Final Project Report

Partitioning of Nanoparticles into Organic Phases and Model Cells

Program Manager: Daniel W. Drell

Principal Investigator: Jonathan D. Posner, Arizona State University
jposner@asu.edu, 480.965.1799

Co-Investigators: Paul Westerhoff, Arizona State University
Trevor Thornton, Arizona State University

Individual Contributors: Wen-Che Hou, Babak Moghadam, Charlie Corredor, Steven Klein, Philip Wheat, Kamil Salloum.

Table of Contents

1. Executive Summary 3
2. Partitioning of engineering nanomaterials 4
   2.1 Octanol-water partitioning 5
   2.2 High throughput microfluidic partitioning 24
   2.3 Lipid bilayer-water distribution 21
3. Engineering nanomaterial disruption of model cell membranes 35
   3.1 Electrophysiology assay 35
   3.2 Dye leakage assay 43
4. Summary 51
5. List of contributions 52
6. References 54
7. Appendices 58

Executive Summary

There is a recognized need to understand and predict the fate, transport and bioavailability of engineered nanoparticles (ENPs) in aquatic and soil ecosystems. Recent research focuses on either collection of empirical data (e.g., removal of a specific NP through water or soil matrices under variable experimental conditions) or precise NP characterization (e.g. size, degree of aggregation, morphology, zeta potential, purity, surface chemistry, and stability). However, it is almost impossible to transition from these precise measurements to models suitable to assess the NP behavior in the environment with complex and heterogeneous matrices. For decades, the USEPA has developed and applies basic partitioning parameters (e.g., octanol-water partition coefficients) and models (e.g., EPI Suite, ECOSAR) to predict the environmental fate, bioavailability, and toxicity of organic pollutants (e.g., pesticides, hydrocarbons, etc.).

In this project we have investigated the hypothesis that NP partition coefficients between water and organic phases (octanol or lipid bilayer) is highly dependent on their physiochemical properties, aggregation, and presence of natural constituents in aquatic environments (salts, natural organic matter), which may impact their partitioning into biological matrices (bioaccumulation) and human exposure (bioavailability) as well as the eventual usage in modeling the fate and bioavailability of ENPs.

In this report, we use the terminology "partitioning" to operationally define the fraction of ENPs distributed among different phases. The mechanisms leading to this partitioning probably involve both chemical force interactions (hydrophobic association, hydrogen bonding, ligand exchange, etc.) and physical forces that bring the ENPs in close contact with the phase interfaces (diffusion, electrostatic interactions, mixing turbulence, etc.). Our work focuses on partitioning, but also provides insight into the relative behavior of ENPs as either "more like dissolved substances" or "more like colloids" as the division between behaviors of macromolecules versus colloids remains ill-defined.

Below we detail our work on two broadly defined objectives: (i) Partitioning of ENP into octanol, lipid bilayer, and water, and (ii) disruption of lipid bilayers by ENPs. We have found that the partitioning of NP reaches pseudo-equilibrium distributions between water and organic phases. The equilibrium partitioning most strongly depends on the particle surface charge, which leads us to the conclusion that electrostatic interactions are critical to understanding the fate of NP in the environment. We also show that the kinetic rate at which particle partition is a function of their size (small particles partition faster by number) as can be predicted from simple DLVO models. We have found that particle number density is the most effective dosimetry to present our results and provide quantitative comparison across experiments and experimental platforms. Cumulatively, our work shows that lipid bilayers are a more effective organic phase than octanol because of the definable surface area and ease of interpretation of the results. Our early comparison of NP partitioning between water and lipids suggest that this measurement can be predictive of bioaccumulation in aquatic organisms.

We have shown that nanoparticle disrupt lipid bilayer membranes and detail how NP-bilayer interaction leads to the malfunction of lipid bilayers in regulating the fluxes of ionic charges and molecules. Our results show that the disruption of the lipid membranes is similar to that of toxin melittin, except single particles can disrupt a bilayer. We show that only a single particle is required to disrupt a 150 nm DOPC liposome. The equilibrium leakage of membranes is a function of the particle number density and particle surface charge, consistent with results from our partitioning experiments. Our disruption experiments with varying surface functionality show that positively charged particles (poly amine) are most disruptive, consistent with in in vitro toxicity panels using cell cultures.

Overall, this project has resulted in 8 published or submitted archival papers and has been presented 12 times. We have trained five students and provided growth opportunities for a postdoc.

2. Partitioning of Engineered Nanoparticles

Engineered nanoparticles (ENP) are now in more than 1,300 commercial products and have found widespread applications as biomedicine, nanosensors, catalysts, cosmetics, antibiotics, microelectronics, opacifiers, and fillers for plastics and rubber.[1] Given that there has been growing evidence that ENPs may exert ecotoxicological effects to a wide range of organisms,[2] it is imperative to develop methods to assess their potential for bioaccumulation and impacts on organisms. Although there is scientific agreement that these ENPs will eventually be discharged into the environment at some point of their life cycle, the ultimate fate of these ENPs in the environment is still widely unknown and difficult to predict. A need exists for experimental and modeling approaches to better understand and predict the bioaccumulation and environmental fate and distribution of ENPs among various environmental compartments (air, water, soil, and biota).

Traditionally, the partitioning of organic compounds between organic solvent phases (typically n-octanol) and water[3-7] is used to evaluate the potential of organic pollutants to bioaccumulate in organisms from the aqueous phase. Additionally, octanol-water partitioning (K_{ow}) correlates with the partitioning of organic pollutants between soil organic matters (SOMs) and water and has been used to predict the mobility of organic pollutants in soil environments. The SOM-water partitioning can help to evaluate where organic pollutants tend to distribute in the soil-water systems (e.g., ground water, farm field). Larger SOM-water partitioning (generally corresponding to higher Kow) could indicate that pollutants (e.g., pesticides) are less mobile with ground water or rain water leaching in top soil layers and the impact will be limited to local ecosystems.

The basic approach of using partition coefficients, instead of detailed measurements (molecular weight, conformation, molar volume, ionic charge, etc.), to predict environmental fate and transport, aquatic toxicity and bioaccumulation is used extensively in current EPA models (e.g., EPI Suite, ECOSAR, etc.). The partitioning types of descriptors that capture the collective physicochemical properties of pollutants (e.g., molecular weight, conformation, charge, etc.) are more robust than individual physicochemical property in predicting the fate, transport, and bioaccumulation potential of pollutants. Similarly, characterization of ENPs often involves numerous physical measurements of size distribution, morphology, surface area, porosity, surface charge density, aqueous zeta potential, surface chemistry, and stability. However, it is extremely challenging to employ these precise ENP measurements as descriptors in models suitable to assess fate and bioaccumulation potential of ENPs. Analogous partitioning type global descriptor methods have not been used extensively for nanomaterials. Therefore, there is a need to develop simplified, empirical approaches for characterizing the distribution of ENPs between environmentally relevant compartments such as water, soils, sediments and biota. The partitioning type of descriptors may be used as inputs to current EPA models or can be used to develop new empirical models by correlating with measured organism-water or soil-water partitioning for ENPs.

In this project, we developed methods to evaluate the octanol-water partitioning of a range of ENPs. Octanol is often used as a surrogate for the biological mediums because octanol is more repeatable and less expensive than using whole organisms or cells. We also developed a novel microfluidic architecture that has the potential to more efficiently measure the octanol-water partitioning for ENPs than conventional shake-flask method. We also developed methods to evaluate the lipid bilayer-water distribution for ENPs. Lipid bilayers are a common constituent to cellular life and constitute continuous barriers between cellular contents (e.g., organelles, cytosols, etc.) and the harsh environment, at which interface the pollutant flux is regulated. Contact with lipid bilayer is the critical first step towards bioaccumulation and any biological effects.

2.1 Develop methods for measuring octanol-water partition coefficients for ENP

In this section, we examine the octanol-water distribution of selected model nanoparticles. Empirical observations of the octanol-water distribution of five ENPs were conducted at a range of pH values and ionic strengths. We propose a novel distribution coefficient that accounts for distribution onto the fluid interface and describe three broad scenarios that bound distribution outcomes. This paper focuses on the development of standardized methods of nanomaterial distribution, empirical observations of unique distribution behavior of ENPs that is distinct from molecular contaminants, the development of a two parameter distribution coefficient, and the broad description of possible distribution outcomes. In this work, we also strive to demonstrate that the outcomes of distribution coefficient experiments are difficult to predict and describe due to their dependence on multiple nanoparticle properties as well as physical mechanisms (e.g., aggregation, dissolution, fluid interface adsorption, etc.) and their relative kinetics.

Experimental Section

Preparation of Nanoparticle Stock Dispersions Working nanoparticle stock dispersions were prepared by suspending nanoparticle powders or prepared nanoparticle dispersions in ultrapure water (Millipore Milli-Q) with conductivity < 1.1 µS/cm. We ensured appropriate particle size and homogeneity of the dispersions by sonicating them for 1 h at 200 W/L using an ultrasonic probe and filtering them with GF/F filters. The particle sizes and zeta potentials at a range of solution pH values were estimated using phase analysis light scattering (ZetaPALS, Brookhaven Instruments, Brookhaven, NY). Freshly made dispersions were used within 48 h. Particle sizes were expressed as the mean value of monomodal number distributions. Table 1 summarizes the nanoparticle types, their estimated isoelectric points (pH_{IEP}) and their average particle sizes.

Table 1. Types and total masses of nanoparticles used in the experiments, their estimated iso-electric points (pH_{IEP}), and the average particle sizes in the stock solutions.

Type	Total mass	Units	pH_{IEP}	Size (nm)
Functionalized silver (Fn-Ag NP)	0.01	mg Ag	NA	~ 3
Silver (Ag-NPs)	0.11	mg Ag	~ 3	~13
Fullerene aggregates (nC_{60})	0.15	mg DOC	~ 2	~ 88
Fullerol aggregates ($nC_{60}(OH)_{24}$)	0.23	mg DOC	~ 3*	~ 48
Hematite (Fe_2O_3)	0.24	mg Fe	~ 9	~ 85

Silver nanoparticles in powdered form were purchased from Sigma-Aldrich (576832-5G), and a stock dispersion with a concentration of 200 mg Ag/L was prepared. A stock dispersion of functionalized silver nanoparticles (Fn-Ag NP) with a carboxyl terminated polymer coating was prepared from a purchased dispersion (Northern Nanotechnologies, Canada) with a concentration of ~430 mg Ag/L. The measured diameter of these functionalized nanoparticles was ~3 nm. Dissolution of these nanoparticles at low pH values prevented estimation of the isoelectric point. The silver concentration was determined by digestion in concentrated HNO_3/H_2O_2 followed by inductively coupled plasma–optical emission spectroscopy (ICP-OES).

Hematite nanoparticles were prepared following a modified version of the method of Penners and Koopal.[8] In brief, 1 L 0.02 M $FeCl_3$ in 4 mM HCl was incubated at 100°C for 24 h to complete sol formation. Nanoparticles were separated by centrifuging at a gravitational force of F > 1700 G for a period of 1 h, discarding the supernatant, and rinsing the sediment with 4 mM

HCl. This was repeated six times. The nanoparticle stock dispersion had a concentration of ~100 mg Fe/L as determined by digestion in concentrated HNO_3/H_2O_2 followed by ICP-OES.

Fullerene C_{60} (nC_{60}) and fullerol ($nC_{60}(OH)_{24}$) nanoparticle aggregate dispersions were prepared by adding ~200 mg of C_{60} dry powder or ~ 70 mg of $C_{60}(OH)_{24}$ to 500 mL or 1000 mL ultrapure water, respectively. The dispersions were sonicated for 6 h and then filtered using GF/F filter to remove large aggregates. The filtrate was collected and used as a stock solution. Preliminary research using FTIR showed that this dispersion preparation protocol does not cause oxidation of these nanoparticle aggregates. The concentration of nC_{60} and $nC_{60}(OH)_{24}$ expressed as dissolved organic carbon (DOC) was analyzed using a total organic carbon (TOC) instrument (Shimadzu TOC-V CSH). The concentrations of the nC_{60} and $nC_{60}(OH)_{24}$ stock dispersions were ~14.5 and ~20 mg DOC/L, respectively.

Octanol-Water Distribution Experiments Distribution experiments were conducted in pre-cleaned and EPA certified 60 mL vials with Teflon-lined septa.[9] The experiments were conducted at pH values ranging from ~2 to ~11 to determine the role of pH in distribution. To eliminate the potential interference of phosphate oxo-ions from phosphate buffers, which can adsorb onto the surface of metal (hydro)oxides and change their surface properties, a freshly prepared solution of 1 mM $NaHCO_3$ in ultrapure water was used as a buffer. The pH was adjusted using HNO_3 and NaOH. Considering that distribution in the range between 6.5 and 8.5 (the pH of natural waters) is the most important for environmental studies, experiments in 1 mM $NaHCO_3$ buffer and no additional pH control were conducted in triplicate. A minimum of three control samples containing only the water matrix and nanoparticles were also prepared. The volumes of octanol and water were 30 mL each. For two types of nanoparticles (nC_{60} and Fn-Ag NP), additional experiments were conducted at two different ionic strengths (10 mM and 100 mM) in addition to those conducted at 1 mM. NaCl was used as the ionic strength modifier because these two ions are usually the dominant ones in salty waters such as sea water which may be the ultimate sink for nanoparticles discharged in aqueous environments. Table 1 presents the initial measured nanoparticle concentrations (expressed as total mass) that were used in the experiments. The selected nanoparticle masses were based on two criteria: (1) the sensitivity of analytical techniques and (2) the concentrations that could be exhibited in the environment if the nanoparticles were trace contaminants. The samples were agitated using a rotary agitator (such as those used during a toxic characteristic leaching procedure) for a period of three days at a constant speed of 30 rpm.

Two sets of experiments were conducted with the hematite nanoparticles. The initial set was in the absence of NOM. The second set was conducted in the presence of Suwannee River Fulvic Acid (C_{NOM} = ~2.1 mg DOC/L; pK_a< 4.5).[10] This amount of NOM was selected (1) because Zhang et al. showed that NOM concentrations in excess of 0.2 mg DOC/mg hematite-Fe do not impact the stability of hematite nanoparticles,[11] (2) because these NOM concentrations are commonly present in surface waters, and (3) to ensure an excess NOM over hematite.

The octanol-water samples containing metal-based nanoparticles were separated into three portions: an octanol phase (27 mL), an aqueous phase (27 mL), and an octanol-water interface (6 mL). Separation of the interface from the octanol and aqueous phases was essential because in some samples a significant fraction of the nanoparticles accumulated at the interface. Extraction of the octanol and aqueous phases did not allow for recovering interface samples smaller than 6 mL without disturbing the interface. The interface represented 10% of the total volume of the octanol and aqueous phases.

Nanoparticle Quantification Different analytical tools were required to quantify the metal and carbon nanoparticle concentrations. We quantified the metal-based nanoparticles by acid digestion followed by ICP-OES. After the separation into three different portions, the octanol and water samples were placed in beakers and slowly evaporated. The nanoparticles remaining in the beakers after the evaporation were digested in concentrated ultrapure HNO_3

and 30% H_2O_2. To improve mass recovery, the interfaces were evaporated in the same capped sample containers in which the experiments were conducted, and then sonicated in ultrapure nitric acid before any additional digestion (if necessary) was conducted. For this reason, interface samples also include the mass partitioned to glass vials and septa. Control samples were handled as their interface sample counterparts. To estimate sample recovery, mass balances were conducted.

To obtain data about the impact of silver nanoparticle dissolution on distribution, silver nanoparticles in the aqueous phase were differentiated from silver cations by measuring the silver ion concentrations using a silver selective electrode (ISE electrode, silver/sulfide, Cole-Parmer, Inc.) before acid digestion commenced. The masses of undissolved silver nanoparticles were estimated as the difference between total silver measured by ICP-OES and silver ions measured by silver electrode.

Carbon-based nanoparticles were quantified using UV-Visible spectroscopy without any additional sample preparation. Absorption wavelengths of 347 nm and 400 nm were selected for the fullerene and fullerol, respectively, after recording their entire UV-visible absorption spectra. Considering that interface absorption measurements could not be conducted, the mass of nanoparticles in the interface was obtained as a difference between the initial mass and the measured masses in both the octanol and aqueous phases.

Results and Discussion

Distribution Trends Impact of pH

Previous theoretical work related to distribution of nC_{60} in organic solvents suggests that nC_{60} should partition into octanol (K_{OW} ~ 6.7).[12] In our experiments, nC_{60} partitioned only slightly in octanol (≤ 10% by mass) at pH > 5.6, while most of the nC_{60} partitioned into the interface (~50%) and aqueous phase (~40%) as Figure 1a illustrates. Distribution of nC_{60} in the interface is not unexpected, as it is well documented that small particles tend to accumulate on interfaces between two immiscible phases following the natural laws of thermodynamics.[13] Placement of a particle at the interface between the two phases stabilizes the interface by decreasing the interfacial energy of the system. nC_{60} interface distribution at higher pH values occurs even though nC_{60} has a large negative surface charge ($\zeta \approx -50$ mV) at neutral and high pH. At these conditions, strong interparticle repulsive electrostatic forces, which result from possible hydroxyl ion adsorption and nC_{60}'s strong electron affinity,[14] keep the nC_{60} aggregates in a stable aqueous dispersion. At pHs near the isoelectric point of nC_{60} (pH_{IEP} = ~2), the mass of nC_{60} in octanol nearly doubles, indicating a reduced stabilizing effect of these electrostatic forces. Likewise, the mass

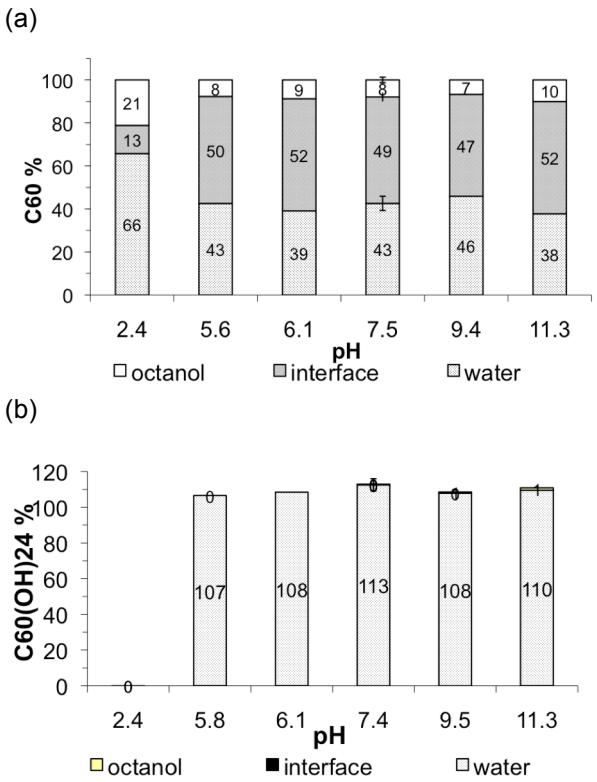

Figure 1. Distribution of (a) nC_{60} and (b) $nC_{60}(OH)_{24}$ in the interface, octanol, and aqueous phases at different pH values in the presence of 1

fraction of nC_{60} in water also increased from ~40% at pH = ~5.6 to ~65% at pH = ~2.4. The increased mass fraction of nC_{60} in the aqueous phase at pH values near the pH_{IEP} is due to its destabilization and resultant aggregation, which leads to settling in the aqueous phase. Control samples confirmed the aggregation and settling.

In contrast to the nC_{60}, $C_{60}(OH)_{24}$ nanoparticles did not partition into the octanol or interface (Figure 1b), which is likely due to their high surface charge at high pH.[15] At pH = ~2.4, however, water-in-oil Pickering emulsions formed instead of clear distribution of the $nC_{60}(OH)_{24}$ into the octanol or interface. When the emulsion droplets were investigated by light microscopy, their vacuole structure (Figure 2a) was observed; this remained stable even when pressed by the microscope slide glass. Discrete nanoparticles or nanoparticle aggregates were not observed because of the limited spatial resolution of the optical microscope. From the experimental perspective, this emulsification prevented the use of UV-Visible spectroscopy to quantify the nanoparticle concentration in octanol at low pH, so data are not reported.

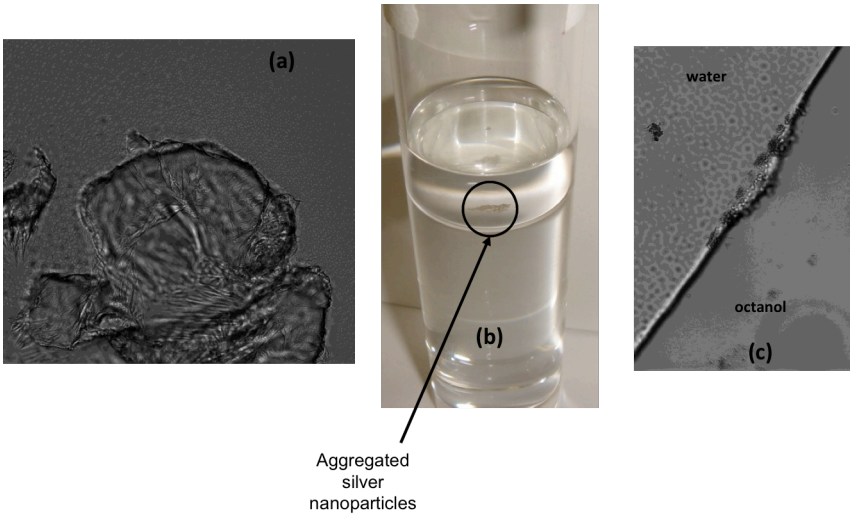

Figure 2. Images of aggregated (a) $nC_{60}(OH)_{24}$ (20 ×) Pickering emulsion of water in octanol; (b) silver nanoparticles; and (c) hematite nanoparticles (20 ×) distribution into the octanol-water interface.

Functionalized silver nanoparticles (Fn-Ag NPs) partitioned primarily into the aqueous phase (> 65%) at high pH (> 8) (Figure S1 in the appendices). At pH = ~7.5, these nanoparticles partitioned equally between the interface and aqueous phase (~46% in each). As the pH became more alkaline, the fraction of nanoparticles distribution into the aqueous phase increased from ~67% at pH = ~8 to >80% at pH = ~11, while the amount of nanoparticles distribution into the interface remained constant (~20-25%). One possible explanation for this trend is that excess Na^+ neutralizes the charge of the deprotonated carboxylic acid groups as well as compresses the electric double layer due to high ionic strength at high pH, making the nanoparticles aggregate and settle to the bottom of the reactor vessel. As the pH decreased from ~7.5 to ~3, the amount of silver in the aqueous phase increased, which we attribute to the dissolution of Fn-Ag NPs to Ag^+. Data from the silver ion-selective electrode analysis show dissolution of Fn-Ag NPs at lower pHs. The fraction of Ag^+ increased from ~20% at pH = 7.6 to almost 80% at pH = 2.7 as the nanosilver dissolved. Only a small fraction (generally < 15%) partitioned into the octanol at neutral or slightly alkaline pH, while traces of Fn-Ag NPs were detected in the octanol at high and low pH. The fraction of Fn-Ag NPs that partitions onto the interface remains relatively constant (~25%) in the alkaline condition. We attribute the increase in interface distribution as pH decreases to the neutralization of the negative charge of the carbonyl groups by the H^+ and Ag^+ resulting from the decrease in pH.

Unfunctionalized silver nanoparticles (Ag NPs) generally partitioned onto the interface, forming a large aggregate that was visible with the naked eye (Figure 2b). At low and high pH

values (pH = ~3 and ~11), the distribution of Ag NPs into the interface increased from ~50-60% to ≥ 70% (Figure S2). We attribute the increase in interface distribution to (a) the ability of the particles to reach the charged fluid interface due the increase in ionic strength at higher and lower pH values that compresses the EDL, and (b) to the neutralization of surface charge by H^+ and Na^+ at low and high pH, respectively. Near the isoelectric point (pH_{IEP} = ~3) at pH = ~2.8, columbic repulsion forces are minimized and the EDLs are thin, so nanoparticles partition onto the interface. Silver ion analysis using the silver-selective electrode suggests high stability of the Ag NPs, with ion fractions of less than <1.4% over the pH range tested.

Hematite nanoparticles partitioned into the interface at pH values of ~8.1 and ~9.7, which are near the estimated hematite isoelectric point (pH_{IEP} = ~9) (Figure 3). At these pH values, 55-65% of the hematite partitioned into the interface, as Figure 3a illustrates. Additionally, ~45 and ~20% of the hematite nanoparticles partitioned in octanol at their pH values of ~8.1 and ~9.7, respectively. Higher magnification images of the hematite nanoparticles obtained by light microscopy show the aggregation and distribution of nanoparticles at the octanol-water interface, as illustrated in Figure 2c for hematite distribution at pH = ~8.1. As the pH decreased from 8.1 to 2.8 or increases above 9.7, the fraction of hematite in water increased to approximately 40%. Interestingly, most (80%) of the hematite partitioned into the water at pH = ~8.7. We attribute this dramatic distribution to nanoparticle aggregation and settling. The rapid change in distribution as a function of pH is indicative of the rich behavior of nanomaterials, the influence of competitive kinetics (e.g., rate of distribution into interface versus rate of aggregation), and the importance of understanding the distribution mechanisms.

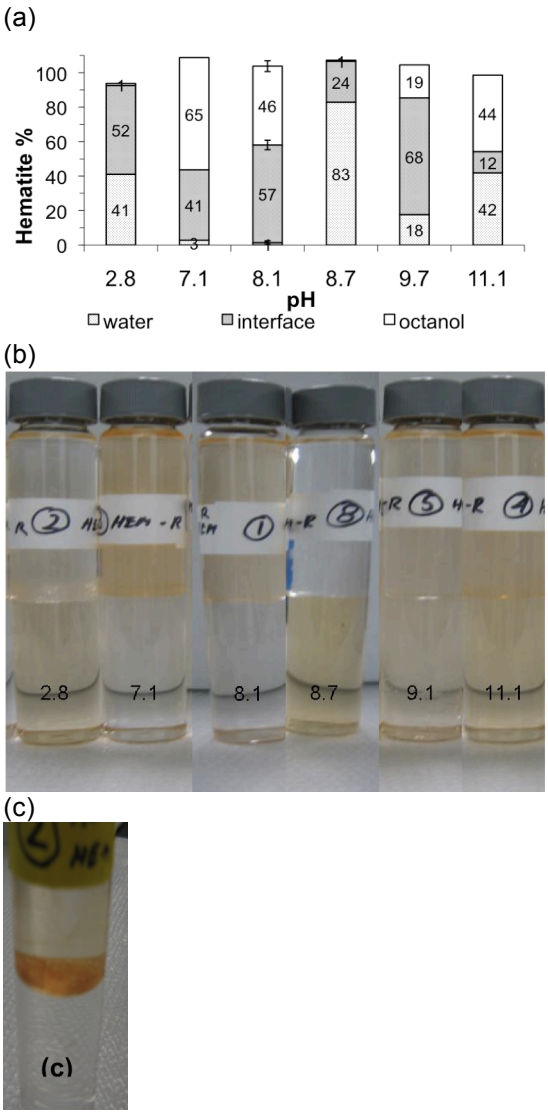

Figure 3. Distribution of hematite nanoparticles into the octanol and aqueous phases and the interface at different pH values in the presence of 1 mM $NaHCO_3$ buffer (a and b); image of aggregated hematite nanoparticles at the interface at pH ~ 8.1 (c).

When NOM was introduced with the hematite nanoparticles, the distribution of hematite exhibited distinct trends (Figure S3). At pH = 2.8, ~13% of the NOM-coated hematite nanoparticles partitioned into the aqueous phase and ~90% partitioned into the interface (in contrast to 40 and ~50% into the aqueous phase and interface, respectively, without NOM). We attribute this increase in interface distribution to the NOM coating, which contains many carboxylic groups (pK_a = ~4.5) that are deprotonated at higher pH and protonated at low pH (e.g., 2.8), making the overall hematite-NOM particle complex less

charged.[16] As the pH increases, the carboxylic groups of the hematite-NOM nanoparticle complex became deprotonated, and the affinity to the aqueous phase increased, causing ~90% of the hematite nanoparticles to partition into the aqueous phase at pH > 7.

Impact of ionic strength and initial nanoparticle concentration Figure S4 illustrates the distribution of nC_{60} at three different ionic strengths at pH = ~7.5. At IS = ~1 mM, the majority of nC_{60} partitioned in the aqueous phase or interface. At this IS, only a small fraction (< 15%) partitioned into the octanol. However, when the IS increased an order of magnitude to 10 mM, nC_{60} was driven to the interface and octanol. An additional increase of IS to 100 mM did not cause any significant change in distribution, suggesting that only aqueous matrices with low ionic strengths impact the distribution of nanoparticles nC_{60}.

Quantifying the Distribution of Nanoparticles Distribution of molecular contaminants in octanol and water can be characterized by a single K_{OW} distribution coefficient. In contrast, distribution of nanoparticles also includes a significant fraction of the mass at the interface between the aqueous and organic phases. To address this interface distribution, we introduce two distribution coefficients, K_D and K_I, which are given as,

$$K_D = \frac{m_O}{m_A} \qquad \text{Equation 1}$$

$$K_I = \frac{m_I}{m_A} \qquad \text{Equation 2}$$

where m_I, m_A, and m_O are the masses of nanoparticles in the interface, aqueous, and octanol phase and the volumes of the octanol and aqueous phases are the same.

The K_D distribution coefficient describes the distribution of nanoparticles between the octanol and aqueous phases. The K_I coefficient describes the distribution of nanoparticles at the interface. The concentrations that are typical of K_{OW} here are replaced by mass quantities in consideration of the facts that the volumes of the octanol and aqueous phases are different than the volume of the interface (theoretically, the interface has no volume), and that mass concentration poorly describes systems containing particles. For the equal water and octanol volumes used here, K_D is effectively identical to K_{OW}.

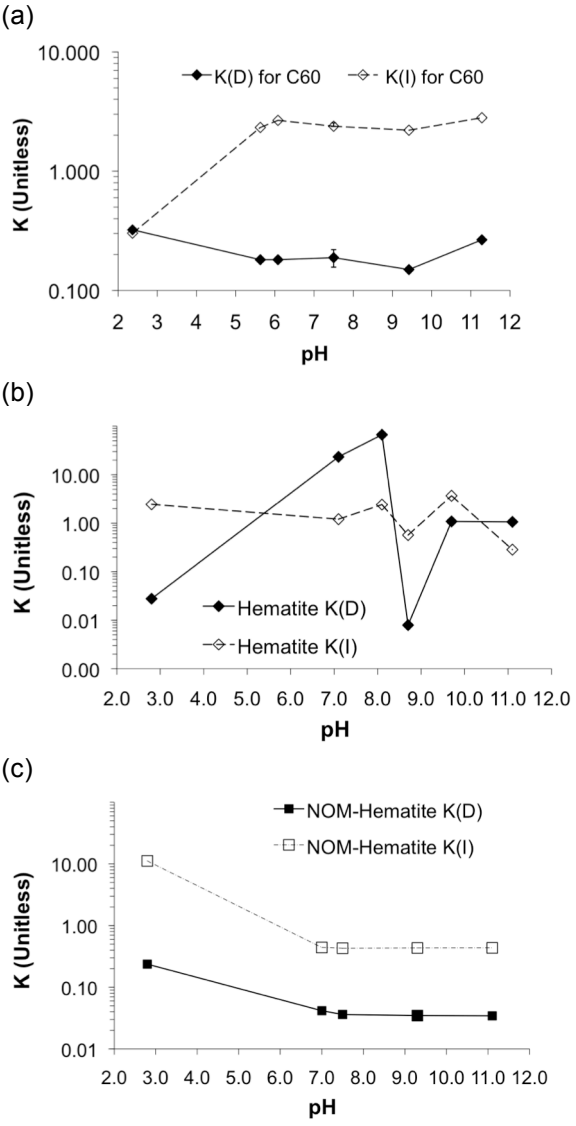

Figure 4. Distribution coefficients K_D and K_I as a function of pH for (a) n-C_{60} nanoparticle aggregates; (b) hematite; and (c) hematite-NOM nanoparticles.

We expect that the mass at the interface depends on the area of the octanol-water interface. This, of course can be tested as part of future work. For systems in which the interface area is small, the nanoparticle assembly already formed at the interface may impede high distribution of nanoparticles into the interface.[17]

The affinity of nanoparticles for each phase or interface can be quantified when K_D and K_I are used together. As summarized in Table S1, nanoparticles prefer the interface with respect to the other phases, but prefer water over octanol when $K_D < 1$ and $K_I > 1$. When $K_D > 1$ and $K_I > 1$, particles still prefer the interface but partition into the octanol over the aqueous phase. When $K_D > 1$ and $K_I < 1$, the nanoparticles tend to prefer octanol, while when both K_I and K_D are less than 1, the nanoparticles prefer the aqueous phase. Values of $K_D \approx 1$ and $K_I \approx 1$ imply that the nanoparticles have equal preference for the interface, octanol and aqueous phase, which is why we define K_D using $2m_I$ instead of m_I in the numerator.

Figure 4 shows the two distribution coefficients plotted versus solution pH for (a) nC_{60}, (b) hematite, and (c) hematite with NOM. These coefficients depend on pH and ionic strength. For example, the estimated coefficients for nC_{60} at pH ≈ 2.4 are $K_D \approx 0.32$ and $K_I \approx 0.30$, which describe a favorable distribution into the aqueous phase with respect to both the interface and octanol, as illustrated in Figures 1 and 4a. In contrast, the coefficients for nC_{60} at pH ≈ 7.5 are $K_D \approx 0.2$ and $K_I \approx 2.4$, suggesting that nanoparticles prefer the interface with respect to the aqueous phase, and prefer aqueous phase with respect to octanol. For hematite without NOM, $K_D \approx 0.03$ and $K_I \approx 1.22$, implying high affinity for the aqueous phase with respect to octanol, and almost equal affinity for the interface with respect to the aqueous phase, as illustrated in Figures 3a and 4b. As the pH increases to 8.1, which is near the pH_{IEP}, columbic forces are minimized, and hematite nanoparticles partition into octanol and the interface. The resulting coefficients are $K_D \approx 57.53$ and $K_I \approx 1.45$. A further increase in pH reverses the process, causing hematite nanoparticles to prefer the aqueous phase again. However, at pH values very close to the iso-electric point (pH = ~8.7; pH_{IEP} = ~9), the hematite nanoparticles aggregate and settle into the aqueous phase, as described by the sharp decrease in both K_D = ~0.01 and K_I = ~0.6. In contrast, the hematite with NOM at pH ≈ 2.8 prefers the interface with respect to the aqueous phase, and is described by the high $K_I \approx 5.6$ and low $K_D \approx 0.24$. As illustrated in Figure 4c, these coefficients decrease as the pH increases. At pH ≈ 7.5, $K_D \approx 0.04$ and $K_I \approx 0.21$ imply high affinity for the aqueous phase, which results from deprotonation of the carboxylic groups present on the surface of the hematite-NOM complex.

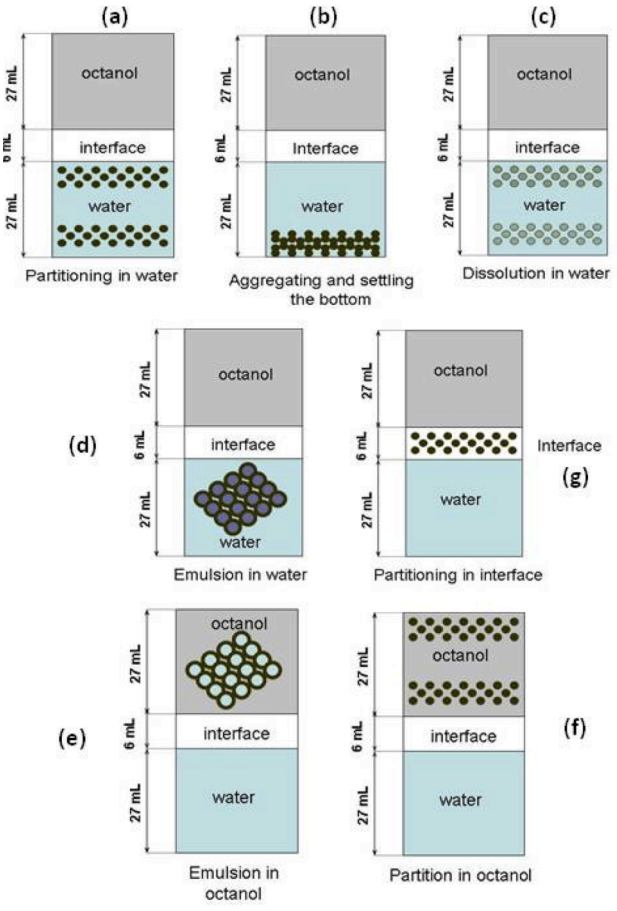

Figure 5. Boundary distribution scenarios of nanoparticles in the octanol and aqueous phases and the interface.

Distribution Scenarios Our experimental distribution data describe the combination of three broadly classified scenarios: (A) distribution in the aqueous phase, (B) distribution in the octanol, and (C) distribution into the interface. Here we briefly describe these three classifications.

Scenario A: Distribution of

nanoparticles in the aqueous phase Nanoparticles can partition in the aqueous phase in four ways to yield $K_D < 1$ and $K_I < 1$, as shown in Figure 5 and discussed below.

(1) *Aqueous nanoparticle dispersion*. High surface charge or other modes of stabilization keep nanoparticles suspended in the aqueous phase without distribution into the organic phase or the interface (Figure 5a). Figure 1 shows that this type of distribution was observed for $nC_{60}(OH)_{24}$ at neutral pH. $C_{60}(OH)_{24}$ molecules have highly negative surface charge and low pH_{IEP} (Table 1), and remain in the aqueous phase at pH > 5.8.

(2) *Aggregation and settling*. Nanoparticles can aggregate and settle to the bottom of the aqueous phase (Figure 5b). According to DLVO theory, particles near their pH_{IEP} and at high ionic strength are destabilized and can aggregate.[18] Regardless of in which phase the particles reside, their aggregates become large and settles due to gravity. This phenomenon may be facilitated by higher nanoparticle concentrations, which increase the rate and extent of aggregation. Figure 3 shows that more than 80% of the hematite nanoparticles partitioned into water at pH = ~8.7, which is near the iso-electric point of hematite (pH_{IEP} = ~9). Figure 4b shows that the hematite distribution into the octanol and interface increases (as characterized by increasing K_D and K_I) as the iso-electric point is approached (from both high and low pH). At the isoelectric point, the particles aggregate and settle to the bottom of the aqueous phase, resulting in a strong decrease in both K_D and K_I. The behavior of hematite demonstrates the complexity of nanoparticle distribution and the importance of the kinetics of the physical mechanisms (e.g., aggregation, dissolution, adsorption, etc.) that govern their equilibrium distribution.

(3) *Dissolution of nanoparticles*. Metal or metal (hydro)oxide nanoparticles may dissolve and form soluble aqueous ionic species (Figure 5c). This was observed for silver nanoparticles, as the mass of silver in the aqueous phase increased as the pH decreased (Figures S3 and S4). The data from the silver ion-selective electrode analysis suggests that the majority of silver remained in the aqueous phase at low pH values because it dissolved to form Ag^+ (Figure S5).

(4) *Pickering emulsions of octanol in water*. Nanoparticles may stabilize the octanol droplets by producing Pickering emulsions of octanol in water (Figure 1d). Although none of the nanoparticles used in these experiments formed Pickering emulsion of octanol in water, poly(N-isopropylacrylamide) particle-stabilized emulsions of octanol in water have been reported.[19] Physically, this scenario can be interpreted as distribution at the interface, while experimentally this condition would be recorded as mass in the aqueous phase.

Scenario B: Distribution of nanoparticles into the octanol Distribution of nanoparticles into octanol or other organic phases can be facilitated by nanoparticle hydrophobicity, reduced surface charge, aggregate size, and/or higher cohesive energy density in the organic phase.[12] When the dispersion pH is approaching the iso-electric point, nanoparticles could form very stable Pickering emulsions in the organic phase (Figure 5e) or could partition into the octanol because of the small electrostatic repulsive forces and higher cohesive energy density in the organic phase (Figure 5f). The aqueous $nC_{60}(OH)_{24}$ exhibited this type of distribution behavior at pH = ~2.5 because the –OH groups on the surface of these nanoparticles were protonated at this low pH (Figure 1). This scenario, in which the vast majority of nanoparticles partition into the octanol, would trend toward large K_D and small K_I values.

Scenario C: Distribution of nanoparticles into the interface Nanoparticles can accumulate at the interface due to a minimization of the Helmholtz energy (Figure 5g). Placement of a particle at the interface between two phases stabilizes the interface by decreasing the interfacial energy from E_0 to E_1 ($E_0 > E_1$). This change in interfacial energy (ΔE) is described by Equation 3:[16]

$$\Delta E = \frac{r^2\pi}{\gamma_{AB}}[\gamma_{AB} - (\gamma_{PA} - \gamma_{PB})]^2 \qquad \text{Equation 3}$$

where γ_{PB} and γ_{PA} are interface tensions between the particle and each of the two phases (N m^{-1}). Interface tensions depend on several factors, including nanoparticle properties (size, surface charge, functional groups, and solubility) and concentration, in conjunction with properties of the immiscible phases.

Unfunctionalized silver nanoparticles clearly partitioned into the interface over a range of pH values, as illustrated in Figure S4 and discussed previously. Functionalized silver nanoparticles also exhibited almost exclusive distribution into the interface at high pH (Figure S3). This type of distribution is characterized by K_I >1 independent of the K_D value.

IMPLICATIONS Distribution coefficients represent a first approach toward integrative surrogate descriptors that account for combined particle properties and that may ultimately provide predictive capabilities for nanoparticle fate in the environment. Our results show that some mixture of the reported scenarios can describe nanoparticle distribution. The two proposed distribution coefficients partly describe the distribution. We expect that particles with K_D >1 and K_I > 1 are most likely to accumulate in the environment and living organisms because of their propensity to partition onto interfaces. Unlike the accumulation of organic pollutants in the environment, which is related to the organic content of the sorbent, distribution of nanoparticles is likely to be dependent on the properties and abundance of the interface surface.

Challenges remain for these distribution descriptors. The current coefficients do not describe or distinguish the state of the particles within each phase, which is likely to impact the nanomaterials' environmental fate and transport. Thus, distribution may be due to a combination of dissociation/dissolution, aggregation and gravity precipitation, or emulsification, for example. Our results suggest that it is difficult to predict or explain distribution using knowledge of particle size and charge plus solvent properties such as pH and ionic strength. This highlights the richness of nanomaterial distribution behavior and its dependence on particle and solvent properties as well as physical mechanisms and kinetics.

A next step to understanding particle fate and transport is investigation of the physical mechanisms, paths, and particle/solvent properties that manifest themselves in various distribution scenarios. Additional descriptors are required that reflect the state of the ENPs (settled, dissolved, dispersed, etc.) within each phase. The ultimate goal is the implementation of a small set of global particle descriptors, perhaps including distribution, into nano-modified fate and transport and qualitative structure activity relationships (QSAR) models that can be used to predict engineered nanomaterials' fate and transport and biological effects in soil and aquatic ecosystems. This work has resulted in a single journal publication:

Hristovski, K.; Westerhoff, P.; Posner, J. D. Octanol-Water Partitioning of Engineered Nanomaterials. *J. Environ. Sci. Heal. A* **2011**, *46*, 636-647.

2.2 Develop, validate, and apply novel microfluidic architectures for NP

Traditional octanol-water and lipid-water partition experiments require long times for equilibrium to be reached and use large samples. Such a method may not be valid for ENPs because particle-particle aggregation may occur. Thus, there is a need to develop a faster partition experimental approach where particle-particle aggregation and adsorption to solid phases may not be as critical.

Miniaturization of octanol-water partition coefficient analysis can offer rapid measurements with minute samples. Flow injection analysis (FIA) and variants of the monosegmented flow analysis (MSFA) have been used with great accuracy to measure K_{ow} of organic compounds.[20] These microvolume methods have reduced the measurement time down to as low as 4 minutes for a single measurement.[20] In these methods, immiscible water and organic phases are loaded into a capillary such that that the octanol and water phases share a large surface area for transport of the sample from one phase to the other. The large surface area and short distances results in rapid equilibrium of the sample. In FIA, the organic phase coats the walls of a PTFE tube whereas in the MSFA the octanol and water form segmented plugs.

Droplet-based (or segmented flow) microfluidic systems have been used to perform various processes such as chemical synthesis and reactions,[21] particle synthesis,[22] extraction and purification,[23] among others. In this paper, we present a segmented flow microfluidic method for measuring octanol-water partitioning coefficients in single picoliter drops. Picoliter water droplets are generated in octanol carrier fluid within a T-shaped segmented flow device fabricated in polydimethylsiloxane (PDMS). The partition coefficient of fluorescein, a fluorescent dye, is measured as a function of pH using epifluorescence microscopy. The microfluidic partitioning measurements reach equilibrium in seconds for a single drop and are conducted in minutes for thousands of individual picoliter droplets. The methods presented here are rapid, provide detailed statistics, and can be run in parallel enabling the simultaneous partitioning of thousands of compounds for various applications such as drug development, environmental testing, and combinatorial chemistry.

Experimental Section

Microchip design. Partitioning microdevices with serpentine channels and a T-shaped segmented flow injector are shown in Figure 6. Segmented flow of octanol and water is generated at the T-intersection at the bottom left of Figure 6. The octanol and water respectively flow from the west and north channels of the T-intersection. The segmented drops of octanol and water flow through the serpentine channels to the waste port at the top right of Figure 1. The injection channels that form the T are 3.4 mm long. Each serpentine channel is 10 mm long. The channels are 100 μm wide and 30 μm tall.

Microfabrication. The devices were fabricated using soft lithography of PDMS. We use an SU8 (2025 MicroChem. Corp., Newton, MA) master template fabricated on a Si (100) wafer (University Wafer Corp., Boston, MA) using photolithography. Sylgard 184 PDMS prepolymer (Dow Corning, Midland, MI) at 30:1 base polymer/curing agent (A:B) is then cast on a silanized master. The PDMS is then cured at 80^{o}C in a convection oven for 30 min. The cured PDMS is peeled off from the master and bonded by baking for 1h at 80^{o}C onto PDMS 3:1 (A:B) that is spin coated onto a glass

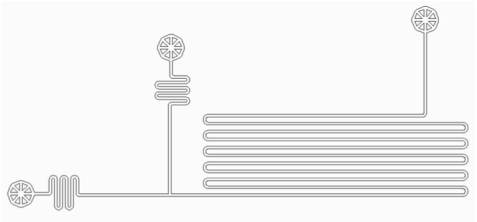

Figure 6. Schematic of the serpentine partitioning microdevice.

microscope slide. The bond strength between the two layers of PDMS was increased by using dissimilar monomer/hardener ratios.

Experimental setup. We used quantitative epifluorescence microscopy on an upright microscope (AZ 100, Nikon, Melville, NY) to image the flows. Images were recorded on a cooled CCD camera (Cascade IIb, Photometrics, Tucson, AZ) with a blue-green filter cube (Excitation 450-490nm, Emission 510-570nm, XF100-2, Omega Optical, Brattleboro, VT). The images are 20 × 20 pixels and are recorded at ~30 frames per second with a 40× objective with a numerical aperture of 0.5. We used two independent (KD Scientific Model 210, Holliston, MA) syringe pumps to provide constant flow rate of the octanol and water. The octanol and water flow rates (Q_{oct} and Q_{water} respectively) were set between 0.3 and 1.0 μL/min for all measurements which results in a Peclet number range of 210-680. The ratio of Q_{water}/Q_{oct} was typically unity, so that the length of the droplets was equal. Glass, 50 μL syringes (Fisher Scientific, Waltham, MA) and 23 gauge needles (0.5 in. long, type 304, i.d. 0.017 in. o.d., 0.025 in.) were used. Fluidic connections were made using Tygon tubing (1/16'' ID, McMaster-Carr, Santa Fe Springs, CA) and stainless steel tubes (NE-1300-01, New England Small Tube Corp., Litchfield NH).

Chemicals. We measure the partitioning of fluorescein disodium salt (Fisher Scientific, Waltham, MA) in HEPES buffered aqueous solutions and 1-octanol (CAS# 111-87-5 Acros Organics, Geel, Belgium). The partition coefficient is measured over a range of pH 6.4-8.3 using 100 mM HEPES buffer (Sigma-Aldrich, St. Louis, MO). The buffer pH is controlled by the concentration of the sodium phosphate monobasic and sodium phosphate dibasic heptahydrate in the solution. These conditions are chosen consistent with previous partitioning measurements of fluorescein of Grimes et al.[24] Although surfactants are typically used in segmented flow devices, here we do not use them to avoid any interference with the partitioning.

THEORY. The partition coefficient is defined as

$$K_{ow} = \frac{C_o}{C_w} \qquad (1)$$

where C is the concentration of fluorescein and the subscripts o and w denote octanol and water respectively. Here we are measuring the partitioning of fluorescein which is an ionizable compound. Partitioning of ionizable compounds are often described by distribution coefficients, apparent partition coefficients, or partitioning ratios. We consider our experiments to be direct measures of the partitioning ratio, following the previous fluorescein partitioning measurements of Grimes et al.[24]

For the range of concentrations used in our experiments, the fluorescence intensity is linearly related to fluorescein concentration. Assuming negligible partitioning into the PDMS and equal and linear fluorescence response in both solvents, one can directly measure the partition coefficient from fluorescence using $K_{ow}=I_o/I_w$, where I is the fluorescence intensity in the (o) octanol and (w) water drops. We found that fluorescein fluorescence in octanol is red shifted 70 nm such that the fluorescence captured using the epifluorescence filters is rather weak. Two-dimensional fluorescence spectra showing the spectral red shift in octanol are shown in the supporting information. Due to the weak fluorescence of fluorescein in octanol, we infer the sample concentration in octanol from the concentration in the water sample. The number of moles in the octanol phase can be written as $n_{oct} = n_{w,initial} - n_{w,final}$. Here the subscripts *final* and *initial* denote the number of moles of fluorescein respectively in a water drop at equilibrium and in the initial state. The molar concentration in the water and octanol are simply $C_w = n_w / V_w$ and $C_{oct} = n_{oct} / V_{oct}$. The concentration of a dilute sample in water can be

measured as $C_w = \beta \cdot I_w$, where β is constant. Therefore, the number of moles in a water drop can be written as $n_w = V_w \cdot I_w \cdot \beta$. Rewriting Equation 1 in terms of intensity of the water drop we get

$$K_{ow} = \left[\frac{I_{w,initial}}{I_{w,final}} - 1 \right] \cdot \frac{V_w}{V_{oct}} \qquad (2)$$

Since the channel depth is uniform throughout the channel, we can approximate the volume ratio of the drops as $V_w / V_{oct} = L_w / L_{oct}$, where *L* is the length of the droplet in the microchannel. In our experiments we infer the length ratio of the drops from the intensity-time plots as shown in Figure 4, and described in the results. Correcting for the background signal, the partition coefficient in terms of measured variables is

$$K_{ow} = \frac{L_w}{L_o} \left[\frac{I_{w,initial} - I_{dark}}{I_{w,final} - I_{dark}} - 1 \right] \qquad (3)$$

where the subscript *dark* denotes the fluorescence measured by the camera in the channel with no fluorescein. The fluorescence intensity of each droplet is determined by area averaging over the droplet area and then ensemble averaging over the multiple frames that constitute a single droplet. Equation 3 assumes that no fluorescence is lost due to photobleaching and that no mass is lost to the channel walls. To avoid photobleaching of the initial intensity images the light source remains blocked for two minutes before taking data. For the final intensities, we capture images of the droplets by taking 50,000 continuous frames at the end of the serpentine channel which takes approximately 15 min. Doing this requires the light source to be illuminating the chip the entire measurement period. We tested for photobleaching under these conditions but found that there was no measureable photobleaching because of the low light intensity used and the limited time each droplet is exposed to the light. Equation 2 also assumes no mass is lost to the channel walls. However, the network polymer structure of PDMS is well known to be permeable to and absorb water and solvents,[25] and small molecules.[26] PDMS has been explored for solid-phase microextraction of organic compounds from aqueous solutions and the equilibrium partitioning of compounds in PDMS-water have been related to octanol-water partitioning coefficients.[27] For these reasons we have run several experiments to determine the effects of partitioning into the PDMS microstructure.

We filled the PDMS channels with fluorescein dyes for 24 h. As we expected, due to fluorescein's relatively polar nature, we found that there was no partitioning of fluorescein into PDMS. However, for an apolar molecule like rhodamine, we and others have observed significant partitioning.[26] Partitioning of the apolar sample molecules into the PDMS microchip may result in a loss of mass depending on the timescale of the experiment and the channel surface to volume ratio. We measured the diffusivity of rhodamine dye in PDMS and found it to be 1×10^{-11} m^2/s, which is one order of magnitude less than in water. See the supporting information for details of the experiment and results. This result suggests that if the experiments can be conducted quickly that the sample molecules may reach equilibrium in the water and octanol phases before significant mass is lost to the microchannel walls. For example, here fluorescein dye reaches equilibrium partitioning in less than two seconds which would translate to a penetration length in PDMS of only 6 μm. The microchannel material, sample molecule polarity, and experiment timescale must all be considered to ensure accurate quantitative measurements. In this case, fluorescein is relatively polar and does not absorb into the PDMS by any measurable amount. Alternatively, to avoid possible partitioning into the microfluidic substrate, the channels can be fabricated in inert materials such as glass, silicon.

Results and Discussion

Figure 7a shows an image of the partitioning device with segmented flow of fluorescein in buffered aqueous water in a carrier fluid of octanol. This image was recorded with a 0.5 × magnification. The segmented flow is generated at the T-intersection (lower left) by flowing 1-Octanol from the west channel well and fluorescein laden HEPES buffer from the north well (of the T-intersection) as shown in Figure 7a. The droplets become darker over time as they travel down the channel and the fluorescein partitions into the octanol. However, the octanol phase remains dark throughout the channel because fluorescein in octanol has relatively weak fluorescence in spectral range of the epifluorescence filters used here. Figure 7a shows that the intensity of the water droplets look nearly equilibrated by the fourth drop, midway through the first channel. Figure 8 shows the normalized water droplet fluorescence as a function of time. The time axis in this plot is a time in the Lagrangian reference frame from the point of creation and can be equated to an Eulerian measure of distance using the average velocity in the channel. The dye diffuses and partitions into the octanol phase resulting in an exponential decay of the fluorescence. The exponential decay time constant is 0.37 and the time to reach equilibrium is approximately 1.2 seconds, which is consistent with Figure 7a. This equilibrium time agrees well with the predictions established by Mary et al. based on the diffusive time scale (L^2/D) and the Peclet number using the droplet length as the characteristic length scale over which mass transport occurs.[23] For our system the time required to reach equilibrium is small relative to the time required to travel through the channel (less than 2 seconds compared to 1 minute).

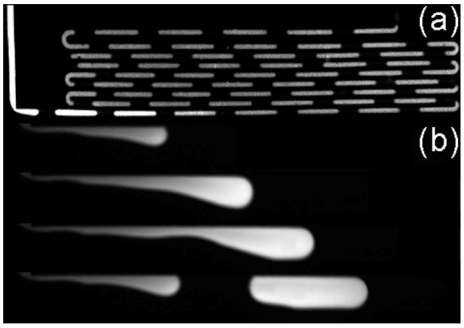

Figure 7. Fluorescence micrograph of microfluidic partitioning device.

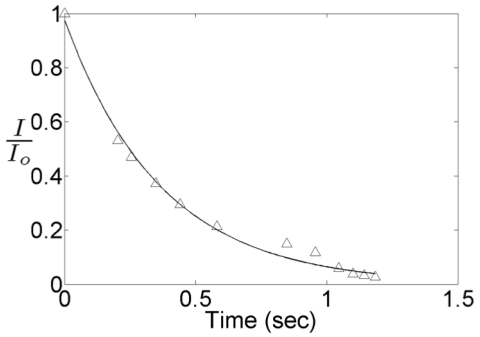

Figure 8. The normalized intensity of fluorescein in a water droplet as a function of time.

Figure 7b shows a magnified view of the T-intersection where the droplets break up. For our system the capillary number $Ca = \mu u/\gamma$ is ~2×10^{-3}, where μ is the fluid viscosity, u is the fluid velocity and γ is the surface tension. This value is less than the critical value of 10^{-2} established by Garstecki et al. therefore the breakup of the droplets is controlled by the Laplace pressure drop across the droplets as they form.[28] The small capillary waves on the surface of the water drops in Figure 7b are evidence of surface tension dominated behavior associated with small capillary number flows. The length of the droplets can be controlled by adjusting the ratio Q_{water}/Q_{oct}.[28] Controlling the length of the droplets is important to partitioning and extraction as it dictates the length scale over which over which mass transport occurs. The lengths of the drops are approximately 300 μm,

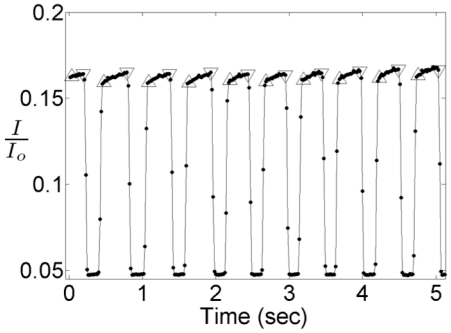

Figure 9. The normalized, area averaged intensity of the droplets versus time measured at the outlet of the microchannel.

resulting in drop volume of ~900 pL.

Figure 9 shows a plot of the normalized intensity of several individual picoliter drops. The regions of the plots with large intensities are the water drops, while the low values correspond to the octanol phase. This data is obtained by monitoring the fluorescence near the outlet of the microchannel (top right in Figure 7a). Each data point in Figure 9 is an area average of the initial, final, and background fluorescence over 20 × 20 pixels. We measure the initial and background intensities at the beginning of each experiment. Each data point in Figure 4 is determined from a single frame of a single droplet.

We use the data shown in Figure 9 to obtain quantitative measurements of the partition coefficient. When calculating K_{ow} for each drop we ensemble average over all of the frames containing a single droplet. The beginning and end of drops are respectively denoted as upward and downward pointing triangles. The drops with intermediate intensities are the interface of the droplets and are not considered when calculating the average intensity. The length of each droplet is also determined using the same criteria, where the intermediate intensities are shared equally between the water and octanol water drops when calculating the length ratio of Equation 3. Figure 10 shows the histogram of the normalized partition coefficient $(K_{ow} - \bar{K}_{ow}) / \sigma_{K_{ow}}$ at pH = 7.93 of nearly a thousand individual drops. The bar denotes an ensemble average over many drops and σ is the standard deviation. Thus each x-axis unit represents one standard deviation and the graph is centered about the mean. The mean partition coefficient of this data set is 0.18, the standard deviation is 0.08 and the coefficient of variance (CV) is 0.44.

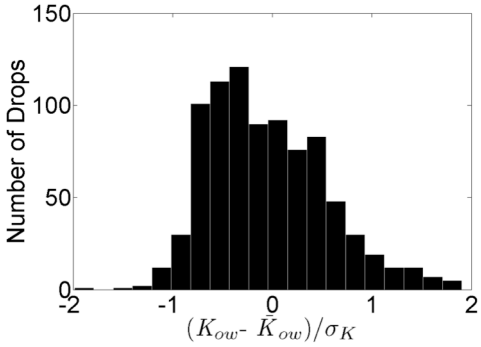

Figure 10. Histogram of the normalized partition coefficient at pH 7.93 of nearly a thousand individual 900 picoliter drops. The x-axis unit represents one standard deviation and the graph is centered about the mean.

In order to validate the microfluidic segmented flow methods used here, we map the partitioning coefficient over a range of pH values pH = 6-8 used by Grimes et al. Figure 11 shows a plot of the measured K_{ow} at pH = 6.43, 6.77, 7.12, 7.66, 7.80, 7.93 and 8.30. The upright triangles show the measurements of Grimes et al., while the squares show the average measurements made with the microfluidic method. Each dot represents the partition coefficient of a single drop and the error bars are two standard deviations. For pH = 7.66, 7.8, 7.93 and 8.26 the error bars are not visible because $2\sigma < 0.3$. The figure shows that the average values obtained with the microfluidic method correspond very well with the trend established by Grimes et al. At pH = 6 the fluorescein partitions highly into the octanol phase while starting at pH = 7.4 the amount of partitioning levels off almost to zero. In our measurements we see that when a molecule partitions highly into the octanol phase that there is a wide variability in the partition coefficient. Despite the large variability, the CV is similar in all of the measurements indiscriminate of pH. The variance is more apparent at high partitioning coefficient (low pH) because both the standard deviation and the mean are larger. In fact, the CV is actually larger in the high pH (0.49) than the low pH (0.36) although the variance appears larger at low pH values.

By examining the individual components in the uncertainty we see that the uncertainty in the intensity is negligible, while the main source of variability arises from the uncertainty in determining the length of the droplets. We expect the variability in the intensity to be small since the fluorescent detection method for fluorescein is very sensitive. The sensitivity of the fluorescence detection method depends on a number of factors including the sensitivity of the camera, the numerical aperture of the imaging system, the octanol-water volume ratios used, the intensity of the light source, the depth of the microchannel and the concentration and fluorescence cross section of the sample being analyzed. Since the variability from the intensity is negligible, the uncertainty is not a function of pH. Rather, the variability is controlled by the length of the droplets in a particular experiment and is largest when the droplets are small. Therefore, we can minimize the variability of our measurements by creating longer droplets or decreasing the uncertainty in determining the droplet length.

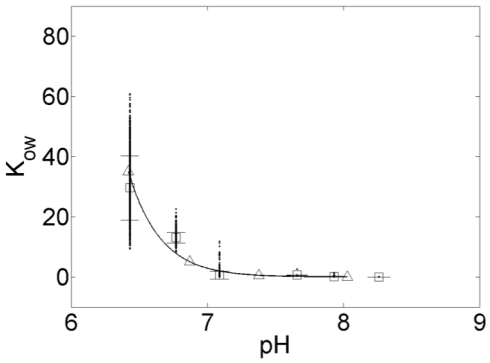

Figure 11. Octanol-water partition coefficient of fluorescein as a function of the buffered aqueous phase pH. The upright triangles, 4, are shake-flask measurements obtained from Grimes et al. The open squares are our average measurements calculated from nearly 1000 drops each.

Conclusion

We have presented a microfluidic method for rapid measurement octanol-water partition coefficient in thousands of picoliter drops. Picoliter water droplets are generated in octanol carrier fluid within a T-shaped segmented flow device fabricated in PDMS. Quantitative measurements of fluorescein partition coefficient are measured as a function of pH which compare well with published values. Here fluorescein concentration is measured using epifluorescence microscopy. This segmented flow partitioning method may also be applicable to a wide range of non-fluorescent compounds using alternative on-chip detection methods such as UV-visible absorption. UV-visible detection has already been applied to segmented flows in capillaries[20] and to on-chip single phase flows.[25] Alternatively, these methods can be adapted into hyphenated platforms with external analytical equipment where the segmented flow output is phase separated to obtain separate water and octanol streams[29] and then analyzed using existing analytical techniques amenable to small samples (e.g. mass spectrometry). The advantage of our microfluidic method is that partitioning within individual picoliter drops reaches equilibrium within seconds while large statistics across thousands of drops can be conducted in minutes. The microfluidic method presented here are rapid, provide detailed statistics, requires small samples, and can be run in parallel enabling the simultaneous partitioning of thousands of compounds for various applications including partitioning or extraction of compounds far from equilibrium where bulk methods may not be appropriate.

We applied these methods to ENP, but found that they do not partition. We attribute the lack of partitioning to the low disturbance level within the microfluidic devices which do not force the ENP across energy barriers required to move from one phase to the other. ENP tend to be electrostatically repelled from octanol-water interfaces and will only go to the interface or move across phases (octanol to water or vice versa) when significant activation energy is put into the system. This is supported by the fact that significant mixing, by sonication, is typically required to generate stable Pickering emulsions. Although the microfluidic methods are not appropriate for ENP, we published a paper on the development of this method for molecular compounds:

Marine, N. A.; Klein, S. A.; Posner. J. D. Partition Coefficient Measurements in Picoliter Drops Using a Segmented Flow Microfluidic Device. *Anal. Chem.* **2009**, *81*, 1471-1476.

2.3 Engineered nanoparticle partitioning in lipid bilayers

Synthetic lipid bilayers, which mimic natural biological membranes, have been used increasingly as replacements for octanol in partitioning studies. Lipid bilayers surround most living cells and organelles and constitute a continuous barrier to the transport of ions and other molecules.[30] The primary function of lipid bilayer membranes is to regulate ion concentration through serving as a passive diffusion barrier as well as incorporating a variety of functional membrane proteins.[30] Molecules or nanoparticles must first interface with lipid bilayers to cause biological effects.[31] The lipid bilayer-water distribution coefficient (K_{lipw}) has been shown to be a more appropriate descriptor than K_{ow} for the biological membrane uptake of some classes of hydrophobic[32-34] and ionizable organic pollutants[35] as well as surfactants.[36] The thermodynamics of fish lipid-water and simulated biological membrane-water partitioning is different from octanol-water partitioning, which is hypothesized to originate from the highly organized structure of biological membranes as opposed to bulk solvent octanol.[34,37]

Lipid bilayers' mass is nearly all at the interface and can be quantified. This eliminates the difficulty encountered in the octanol-water partitioning of surface-active compounds and potentially some types of ENPs that may also accumulate at the octanol-water interface as we show in section 2.1.[13,38,39] The most widely used technique to determine lipid bilayer-water distribution coefficients is the equilibrium dialysis method in which water and a liposome suspension (i.e., lipid bilayer vesicles) are separated by a dialysis membrane that allows the diffusion of chemicals but not the liposomes.[33,35,36,40,41] However, using dialysis membranes to separate the water and liposomes may hinder ENP diffusion and promote mass losses considering that unilamellar liposomes generally have sizes <100 nm, close to those of ENPs.

We have examined the lipid bilayer-water distribution behavior of ENPs using solid-supported lipid membranes (SSLMs)[42,43] with the goal of developing a quantitative method for assessing the interaction at this critical nano-bio interface.[31] We used commercial lipid bilayers noncovalently coated on silica spheres, which offer the advantage that the relatively dense SSLMs can be separated easily from free ENPs by gravitational settling. SSLMs have fluid bilayers and have been used in phase distribution studies of organic acids and pharmaceutical compounds and the results are consistent with those obtained by the equilibrium dialysis method.[41,43] We selected nC_{60} and polyhydroxylated C_{60} (i.e., fullerol) for lipid bilayer-water distribution tests because nC_{60} and fullerol are the focus of recent ecotoxicology, fate, and transport studies,[44] and fullerol-like C_{60} derivatives are potential transformation products of nC_{60} in the aquatic environments.[45-47] We have examined the interaction kinetics of nC_{60} and fullerol with SSLMs and described their distribution behavior between water and lipid bilayers as a function of pH using classical isotherm models to represent their behavior over several orders of magnitude in initial ENM concentrations. The distributions depend strongly on pH, suggesting that electrostatic interactions between lipid bilayers and ENPs are important. The results from the SSLM and fullerene nanoparticle interaction studies are compared with recent bioaccumulation and toxicity studies using aquatic organisms to demonstrate their potential and to identify promising areas for future research.

In the second part of the lipid bilayer-water distribution studies, we examined functionalized gold nanoparticles (Au NP) with various sizes (5-100 nm) and two surface coatings (tannic acid and polyvinylpyrrolidone (PVP)). We have examined the interaction kinetics, reversibility and dose dependent behavior of Au NPs with SSLMs. We rationalized the kinetic trend for Au NPs with different diameters by particle transport and the Derjaguin-Landau-Verwey-Overbeek (DLVO) theory. The data was also used to explore the selection of mass versus number concentration dosimetry for nanoparticles. A single distribution coefficient (K_{lipw}) was used to fit the data across a wide range of spherical functionalized Au NP diameters.

Experimental Section

Materials. C_{60} (99.9%) and fullerol [$C_{60}(ONa)_x(OH)_y$, x + y = 24, 95+%] were purchased from MER Corp. (Tucson, AZ). Gold nanoparticles (Au NP) of various sizes (5-100 nm) and surface coatings (tannic acid or polyvinylpyrrolidone (PVP)) were purchased from nanoComposix (San Diego, CA) and used as received. Chicken egg phosphatidylcholine lipid (egg PC) was purchased from Avanti Polar Lipids (Alabaster, AL). According to the supplier, the major composition of the egg PC is dioleylphosphatidylcholine (DOPC). Other chemicals were of the highest purity available and used as received. All aqueous samples were prepared using water purified with a Milli-Q Advantage A10® system (Millipore Corp., Billerica, MA).

Model Biological Membranes. Solid-supported lipid bilayer membranes (SSLMs) are available as TRANSIL® binding kits and were purchased from Sovicell (Leipzig, Germany). TRANSILs are 10-μm porous silica spheres completely and noncovalently coated with unilamellar egg PC lipid bilayers.[42,43] The surface charge of the silica surface is properly shielded to minimize electrostatic interaction between lipid bilayers and silica, thereby retaining the natural fluidity of lipid bilayers, which mimics actual cell membranes according to the published characterization data for the material.[42,43] TRANSILs were used as per the manufacturer's instructions. TRANSILs were stored at -20°C. Prior to use, SSLMs were thawed at room temperature for 3 h or at 4°C overnight. The TRANSIL electrolyte has a high salt concentration (i.e., 150 mM KCl) and was replaced by 5-20 mM phosphate buffer to prevent nanoparticle aggregation during use.

We also prepared lipid bilayer vesicles (i.e., liposomes) with composition identical to the SSLM in order to measure the effective lipid zeta potential. The liposomes were prepared following a literature method.[48] Briefly, dry lipid powder was dissolved in chloroform prior to placing in test tubes and drying under N_2. The resulting lipid film was hydrated with electrolytes under mild sonication to form multilamellar liposome suspensions. The suspensions were passed through polycarbonate membrane filters with a pore size of 100 nm held within a commercial extruder (LIPEX, Northern Lipids Inc., BC, Canada) 11 times.

Because the egg PC lipid used in this study contains a phosphate moiety, we determined the lipid concentrations by the malachite green dye method after converting the organic phosphate to inorganic phosphate.[49] We also used this method to check that lipid bilayers remained attached to the solid support during storage, processing, and experiments by determining the lipid concentration of SSLM sediments after removing supernatants containing loose lipids. In a test of 2 days of mixing in room temperature (23°C), the results indicate that SSLM was stable, remaining at 102 ± 6% of the as-received lipid concentration of 15.4 mM.

C_{60} and Fullerol Nanoparticles. Aqueous C_{60} clusters (nC_{60}) were prepared by extended stirring of pulverized C_{60} dry powder in water following procedures described previously.[50] The nC_{60} was passed through 0.7-μm glass fiber and 0.45-μm cellulose ester membrane filters sequentially and concentrated using a rotary evaporator as needed prior to use. Aqueous fullerol dispersions were prepared by directly mixing dry fullerol powder and water (2600 mg/L) in a bath-type sonicator for 1 h. A portion of the fullerol suspension was diluted to 200 mg/L and then passed through 0.7-μm glass fiber and 0.45- and 0.22-μm cellulose ester membranes filters sequentially prior to use.

Nanoparticle and SSLM Interactions. The distribution studies were performed by placing various concentrations of SSLM (0.47 to 4.7 mM lipid) and fullerene nanoparticles (1 - 190 mg/L) in glass vials (1.5 mL) sealed with caps with PTFE septa lined with aluminum foil. The solution was buffered between pH 3 and 8.6 using phosphate electrolytes (5-20 mM). Vials were covered with aluminum foil and mixed on a rotary mixer (50 rpm) for prescribed durations at room temperature (23°C). Upon sampling, vials were removed from the mixer and left to sit quiescently for 30 min, allowing the SSLM beads to settle to the bottom so that supernatants containing free nanoparticles could be drawn for analysis of concentrations (i.e., $C_{w,\,eq}$).

Triplicate samples were prepared for each distribution isotherm data point. Corresponding control samples that contained nanoparticles only, used to account for nanoparticle losses to vial walls or due to sedimentation, were prepared in the same manner as experimental samples except that SSLM was not added. Distribution isotherms were constructed by plotting $C_{w,\,eq}$ (mg/L) against $C_{lip,\,eq}$ (mg/kg lipid). $C_{lip,\,eq}$ indicates the mass of fullerene aggregates in the lipid phase normalized by the mass of lipid. The masses of nanoparticles accumulating in the lipid phase were determined either by direct measurement of the ENP concentration in the lipid phase (for nC_{60}, and Au NP) or by the difference between the free nanoparticle concentrations of the control and experimental samples (for fullerol due to the lack of analytical method to extract fullerol from SSLM). We were unable to extract fullerol from bilayers using toluene, electrolytes, or DI water.

We performed careful mass balances on ENP samples and the results indicate that >90% of the added ENP mass was recovered from the supernatants, SSLMs, and vial walls combined. The aqueous phase fullerol concentrations in the control samples were stable, showing no loss due to sorption to vial walls or settling at respective pH. The decrease in the aqueous phase fullerol concentration in the presence of SSLM can therefore be attributed to accumulation to lipid bilayers. Lipid bilayer-water association coefficient, K_{lipw} (L/kg), which varies for each material as a function of the pH and initial nanoparticle loading, was calculated by dividing $C_{lip,\,eq}$ by $C_{w,\,eq}$. The times required for apparent equilibrium were obtained from kinetic studies.

We also performed careful validation experiments for SSLM. We used a reference compound, 2,4,6-trichlorophenol, whose K_{lipw} determined by the dialysis method using liposomes is known[35] to characterize the utility of SSLM. The validation experiment was performed in duplicate samples under the same conditions as in reference[35], so that the results are comparable. In addition, to examine the potential effects of the silica support on the distribution behaviors of nC_{60} and fullerol, we performed control experiments using the bare silica spheres received from the SSLM supplier.

The lipid bilayer-water distribution of Au NPs was constructed by plotting $C_{w,\,eq}$ against $C_{lip,\,eq}$. We express $C_{w,\,eq}$ in two ways: mass or number concentration of Au NPs (i.e., mg/L or #/L). The lipid bilayer-water distribution coefficient, K_{lipw} (L/kg), which varies for each nanoparticle as a function of initial Au NP loading, was calculated by dividing $C_{lip,\,eq}$ by $C_{w,\,eq}$. Accordingly, we express $C_{lip,\,eq}$ as Au NP mass or number per unit mass of lipid (mg/kg or #/kg). We determined the mass of Au NP in aqueous phase or accumulating in the lipid phase by directly measuring it using inductively coupled plasma-optical emission spectroscopy (ICP-OES). We then converted the Au NP mass to particle number as,[51]

$$N = \frac{M}{\frac{2}{3}\pi(\frac{d_p}{a})^3}, \qquad (1)$$

where the edge of a four gold cubic cell a is 4.0786 Å, M is the number of the gold atoms in a sample measured by ICP-OES and the denominator is the number of gold atoms per particle with diameter d_p.

Analysis. nC_{60} concentrations were determined by HPLC on a reverse phase column (LC-18, 5 µm, 4.6 mm × 150 mm, Supelcosil) with UV detection at 336 nm. The mobile phase was a 50/50 mixture (v/v) of toluene and methanol at 1 mL/min. Prior to HPLC, molecular C_{60} was extracted from nC_{60} in the aqueous phase or in SSLMs to toluene with the aid of 0.1 M $Mg(ClO_4)_2$ following a method reported previously.[50] The toluene extracts were mixed with 50% (v/v) methanol before injection into the HPLC. Fullerol concentrations were measured without extraction by UV-visible absorption spectroscopy at 254 nm. Because the extinction coefficient for fullerol is pH dependent, the fullerol concentration at a given pH was quantified using the extinction coefficient determined with the same pH buffer matrix. The concentration of 2,4,6-trichlorophenol was determined by HPLC on the same column as for C_{60} with UV detection at

280 nm. The mobile phase was a 20/80 mixture (v/v) of phosphate buffer solution (pH = 2.5) and methanol at 1 mL/min.

All Au NP experiments included the analysis of gold in both aqueous and SSLM phases. Au NP mass concentrations were determined by ICP-OES. Prior to ICP, particulate gold samples were acidified with aqua regia, adding 3 parts of HCl and 1 part of HNO_3 by volume ratio (both ULTREX II ultrapure reagents, J. T. Baker, Phillpsburg, NJ). We carefully removed the whole supernatants (~0.97 mL of the 1 mL total sample volume) containing free Au NPs for analysis by pipetting. We also measured Au NP mass accumulated in SSLM (i.e., $C_{lip,\ eq}$) after removing supernatants. The Au NP-associated SSLM samples were transferred to clean vials and acidified there with aqua regia prior to ICP. We consistently recovered > 90% of the added Au mass from the supernatants and Au NP-associated SSLM samples combined using the described procedures.

The sizes and zeta potentials of nanoparticles and liposomes were determined on a dynamic light scattering (DLS) particle sizer (NICOMP 380 ZLS, Particle Sizing Systems, Santa Barbara, CA) that uses a laser light at 635 nm. All particle sizes are reported as intensity-weighted sizes. For scanning electron microscopy (SEM) imaging, samples were drop dried on silicon wafers and gold sputtered. Samples were imaged on a Hitachi S4700 field emission SEM operated at 5-15 kV. For TEM imaging, samples were dried on 400 mesh copper grids prepared with continuous carbon support films. Samples were imaged on a TOPCON 002B TEM operated at 8.9-200 kV. FT-IR spectra were recorded on a Thermo Nicolet Nexus 670 FTIR spectrophotometer. Samples were prepared by embedding dried nC_{60} or fullerol in KBr pellets.

Results and Discussion

Part 1: Lipid bilayer-water distribution of fullerene nanoparticles

Material Characterizations TRANSILs are porous silica spheres with a uniform size of 10 μm and well-characterized surface areas that are noncovalently and fully coated with a single (i.e., unilamellar) chicken egg phosphatidylcholine (PC) lipid bilayer that mimics the natural fluid properties of biological membranes.[42] The size and porous structure were confirmed by optical and TEM images that indicate a size range of 8-12 μm. A typical TEM image of TRANSIL is presented in Figure S5 in the appendices. It was difficult to observe the unilamellar lipid bilayer that is only 4 nm thick[52] on the structurally dense 10 μm silica spheres using the TEM technique even at high magnification. We confirmed the presence of lipid bilayers by measuring the lipid concentration instead. The lipid concentration was measured as 14.5 ± 0.7 mM by determining the phosphorus content, which correlates with the manufacturer-reported value of 15.4 ± 0.8 mM.

We validate the utility of the SSLM method using a reference compound (i.e., 2,4,6-trichlorophenol) and report a log K_{lipw} at 3.89 ± 0.03, close to the value of 3.90 found in previous studies using dialysis equilibrium with liposomes of similar lipid compositions.[35,41] This result supports that the fluidity of the supported lipid bilayers is similar to that of liposomes (i.e., free standing lipid bilayers), as it has been reported that the decrease in fluidity can significantly reduce the lipid bilayer-water partitioning.[53] In addition, we also compared the interactions of nC_{60} or fullerol with SSLMs versus bare silica spheres. The results not reported here shows that the interaction of nC_{60} or fullerol with SSLMs is significantly different from that with bare silica spheres that the bilayers are supported on. The data collectively suggests that lipid bilayers dictate the interaction of fullerene aggregates and SSLMs and that any incomplete coverage of silica surfaces, if any, does not influence the observed lipid bilayer-water distribution of fullerene aggregates.

We have characterized nC_{60} and fullerol using FT-IR spectroscopy and TEM. The data are presented in Figure S6. nC_{60} appears to have a denser structure and more facets than fullerol. The size of nC_{60} agrees reasonably with DLS measurements. Fullerol appears to be amorphous with large and loosely associated aggregates. There are occasionally single particles with a size close to DLS measurement (Figure S6b inset). The large and loosely associated fullerol aggregates may be attributed to sample drying required for TEM imaging. Our TEM images of fullerol are similar to those reported in a prior study on fullerol aqueous cluster formation.[54] The FT-IR spectra indicate that nC_{60} retains the absorbance peaks at 528, 577, 1183, and 1429 cm^{-1} characteristic of bulk pristine C_{60} materials,[46] indicating that nC_{60} preparation by extendedly stirring dry C_{60} powder in water has not significantly altered C_{60} chemical signatures. In contrast, the C_{60} characteristic absorbance peaks disappear for fullerol with new and broadened peaks emerging at 1060, 1390, 1630, and 3400 cm^{-1} indicative of oxygen containing functionalities.[46,47,55]

Figure 12 reports the zeta potentials of egg PC liposomes, fullerol, and nC_{60} under solution chemistry similar to that in which the interaction experiments of SSLM and nanoparticles were conducted. Due to the rapid sedimentation of SSLMs, a property undesirable to electrophoretic mobility measurement, stable liposomes with a measured size of 120 nm were used for zeta potential measurement instead. The results indicate that the egg PC liposomes have an isoelectric point at pH ≈ 4 and became more negative, decreasing from 7.35 to – 20 mV, as pH increased from 3 to 8.2, in good agreement with prior reports on PC lipids.[56] The as-prepared nC_{60} and fullerol were similar sizes of 139 ± 49 nm and 149 ± 65 nm, respectively (Figure 12 inset). The zeta potentials of both nC_{60} and fullerol nanoparticles were ~ 30 mV more negative than those of egg PC liposomes throughout the reported pH range and also exhibited pH-dependent electrophoretic behaviors similar to egg PC liposome.

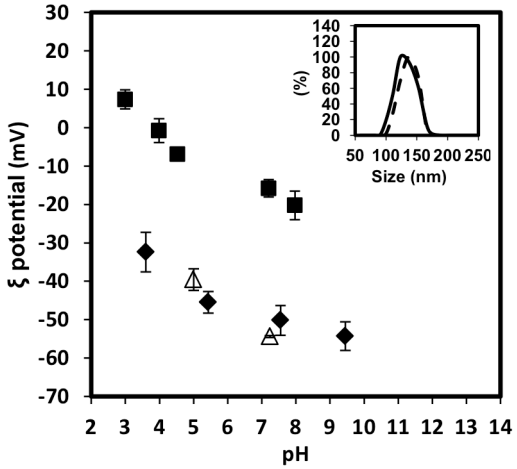

Figure 12. Zeta potentials of egg PC liposomes (0.87 mM) (■), fullerol (650 mg/L) (♦), and nC_{60} (6.5 mg/L) (Δ). Inset: intensity-weighted size distributions of as-prepared nC_{60} (solid line) and fullerol (dashed line) in DI water. Error bars indicate ± one standard deviation.

Interaction Kinetics To determine the duration required to reach pseudo-equilibrium for ENPs between the solution and lipid phases, kinetic studies were conducted. The interaction kinetic studies of nC_{60} or fullerol with SSLM measured by the accumulation of nC_{60} or fullerol mass to SSLM are shown in Figure 13. We directly measured the nC_{60} mass accumulated in SSLM after carefully removing the supernatant containing free nC_{60} by transferring nC_{60}-associated SSLM to clean vials and extracting C_{60} with toluene from there. We then measured molecular C_{60} concentration extracted in toluene using HPLC. nC_{60} associated to SSLM and reached apparent equilibrium after mixing with SSLM (0.47 mM lipid) for 9 h at pH = 7.4, plateauing at ~ 4,000 mg nC_{60}/kg lipid (Figure 13a, triangles). We found that the kinetics is pH dependent. At pH = 5, the nC_{60} reached apparent equilibrium in 30 h, staying at a stable lipid phase concentration of ~ 10,000 mg nC_{60}/kg lipid. The as-prepared nC_{60} size remained constant (i.e., ~ 145 nm) throughout the experiments. The nC_{60} zeta potential changed from - 54 mV to - 31 mV and from - 40 mV to - 14 mV for pH values of 7.4 and 5, respectively, after 20 h of mixing with electrolytes at both pH values. The reduction in zeta potential may be attributed to the presence of counter ions in the electrolyte (i.e., H^+, Na^+ and K^+), that screen the surface charge. Although equilibrium time for nC_{60} is longer at pH 5 than 7.4, the initial kinetics is faster at pH = 5 which is likely due to the decreased electrostatic repulsion between lipid bilayers and particles based on the zeta potential change which may explain the faster interaction rate.

The accumulation of fullerol in SSLMs reached apparent equilibrium more rapidly (~2 h) compared to nC_{60}. Fullerol shows negligible accumulation to SSLM at pH = 7.4 as well as 6,000 and 22,000 mg fullerol/kg lipid of accumulation at pH = 5 and 3, respectively. The size of the fullerol particles remained constant at 150 nm over the duration of the experiments. The zeta potential of fullerol stayed relatively constant, slightly decreasing from -41 to -52 mV at pH = 3, from -46 to -58 mV at pH = 5, and from -59 to -65 mV at pH = 7.4 during the period of equilibration.

Distribution Isotherms We fit our data to classical pseudo-equilibrium isotherm models (Langmuir or Freundlich) to model the behavior of ENPs concentrations over several orders of magnitude with relatively constant lipid bilayer mass. The distribution of nC_{60} and fullerol between SSLM ($C_{lip,\,eq}$) and the aqueous phase ($C_{w,\,eq}$) in the pH range of 3 to 7.4 is presented in Figure 14. We performed experiments that result in $C_{lip,\,eq}$ that spans nearly two orders of magnitude. Although we measured the fullerol distribution up to pH = 8.6, fullerol accumulation to SSLMs was minimal at this high pH and was close to the detection limit of our method. In Figure 3b, we show the data for pH = 7.4 only for qualitative comparison purpose. The accumulation of both nC_{60} and fullerol on SSLMs increases with decreasing pH consistent with reduction in electrostatic repulsion (indicated by zeta potential, see Figure 12). The nonlinearity between $C_{w,\,eq}$ and $C_{lip,\,eq}$ at higher concentrations

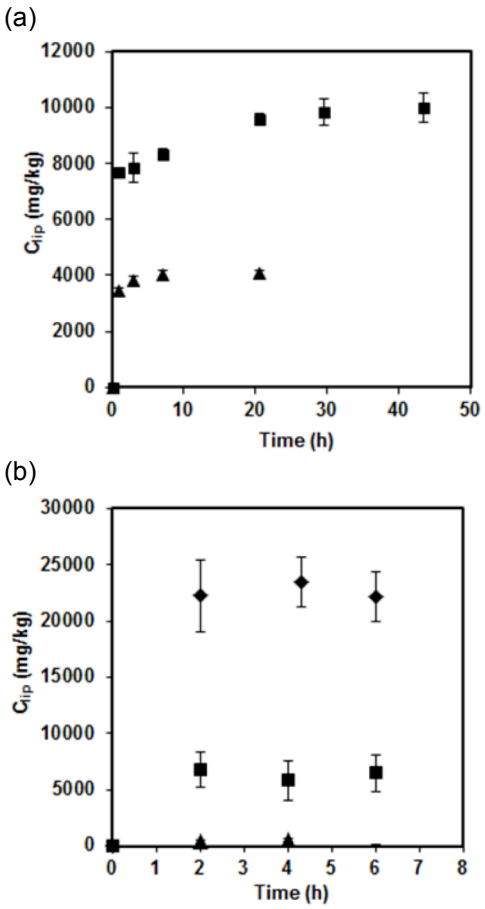

Figure 13. Interaction kinetics of nC_{60} (a) and fullerol (b) to solid-supported lipid bilayer membranes (SSLMs), indicating the accumulation of nC_{60} or fullerol mass to SSLM normalized by lipid mass (i.e., C_{lip}) at pH = 7.4 (▲), 5 (■) or 3 (♦). Error bars indicate ± one standard deviation.

may be attributed to some nanoparticle accumulation on the SSLM that modify the lipid surface charge characteristics leading to repulsion of like-charged nanoparticles.

We use Freundlich and Langmuir isotherm models to fit the data because of the observed nonlinearity in distribution isotherms. Freundlich isotherms are shown in Figure 14. The fitting parameters of both models are summarized in Table 2. The two models are similar in terms of goodness of fits based on r-squared values. Although we tend to use the two isotherm models as empirical fitting tools for the data presented here, there are some interesting trends in the fitted parameters. The Freundlich capacity parameter (K_F) increases with decreasing pH and is consistent with the observed accumulation trends for nC_{60} and fullerol. The fullerol Freundlich exponent (n), which reflects the interaction linearity of fullerol and SSLMs, increases with the decrease in pH and approaches unity (0.94) at pH = 3. A linear relationship implies that the overall driving forces for fullerol association with SSLMs are constant with varying fullerol concentrations.[57] Both fullerol and nC_{60}'s Langmuir maximum accumulation capacity parameters ($K_{lip,\ max}$) increase with decreasing pH in accord with the observed accumulation trend.

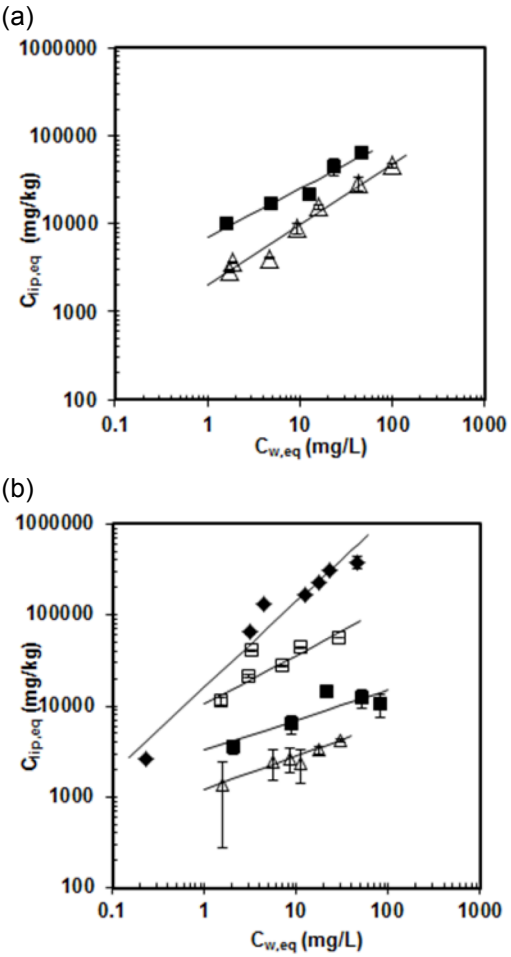

Figure 14. Distribution of nC_{60} (a) and fullerol (b) between water and solid-supported lipid bilayers, indicating the isotherms at pH = 3 (♦), 4 (□), 5 (■), and 7.4 (Δ). The distribution isotherms of nC_{60} were only measured at pH = 5 and 7.4. Lines represent the fit of Freundlich isotherms to the experimental data. Error bars indicate ± one standard deviation.

Lipid Bilayer-Water Association Coefficient The relationship of $C_{lip,\ eq}$ to $C_{w,\ eq}$ is nonlinear (i.e., lipid bilayer-water association coefficient, $K_{lipw} = C_{lip,\ eq}/C_{w,\ eq}$, is not constant with varying $C_{w,\ eq}$) as shown in Figure 14. We use the lipid bilayer-water association coefficient as a general description of fullerene aggregate distribution between lipid bilayers and water, a process that potentially involves interaction mechanisms of adsorption (i.e., interaction on the lipid bilayer surface), absorption or partitioning (i.e., enter into the hydrophobic region of lipid bilayer) or even membrane-mediated endocytosis where fullerene aggregates cross the lipid bilayers.[58-60] Considering that fullerene aggregates are ~150 nm, while the lipid bilayers are ~4 nm thick, it is physically unlikely that all the particles be embedded in the hydrophobic tails of a supported bilayer because the mass of lipids must be conserved. It is, however, possible that particles can partially penetrate the bilayer and interact with the hydrophobic tails of the lipids. A recent simulation paper suggests that C_{60} molecules within small aggregates can translocate into the bilayer in microseconds, dispersing as monomers in the hydrophobic tails.[58] This suggests that small C_{60} aggregates may actually partition into lipid bilayers. It is uncertain if partitioning of fragments of large fullerene aggregates at the size of 150 nm can occur, as the simulation work only ran very short-term simulations (i.e., ~μs), ignored electrostatic interactions, only addressed small aggregates, and was for a free standing

membrane. The membrane-water distribution of fullerene aggregates we observed here may be a combination of adsorption and, to a much less degree, absorption (i.e., partitioning).

Table 2. Parameters of the Freundlich models fitted to nC_{60} and fullerol isotherm data.

ENPs	pH	Freundlich model: $C_{lip,eq} = K_F \cdot C_{w,eq}^{n}$				Langmuir model: $C_{lip,eq} = K_{lip,max} \cdot K_{ads} \cdot C_{w,eq} / (1 + K_{ads} \cdot C_{w,eq})$			
		log K_F ($L^n/mg^{n-1} \cdot kg$ lipid)	n	r^2	log K_{lipw}*	log $K_{lip,\ max}$ (mg/kg lipid)	K_{ads} (L/mg)	r^2	log K_{lipw}*
nC_{60}	5	3.85	0.55	0.95	3.40	4.70	0.2	0.91	3.52
	7.4	3.30	0.69	0.98	2.99	4.40	0.08	0.92	3.05
Fullerol	3	4.21	0.94	0.95	4.15	5.70	0.05	0.90	4.22
	4	4.02	0.54	0.95	3.55	4.70	0.2	0.98	3.52
	5	3.52	0.33	0.73	2.85	4.10	0.2	0.94	2.92
	7.4	3.08	0.37	0.93	2.45	3.52	0.38	0.92	2.42

*modeled log K_{lipw} at $C_{w,\ eq}$ = 10 mg/L.

Table 2 reports the log K_{lipw} values for nC_{60} and fullerol at a given $C_{w,\ eq}$ = 10 mg/L. The log K_{lipw} values in Table 1 were calculated using Freundlich or Langmuir models. To do this, we calculate K_{lipw} by determining $C_{lip,eq}$ for $C_{w,eq}$ = 10 mg/L using either model. The K_{lipw} of nC_{60} is consistently larger than that of fullerol at a given pH (i.e., 5 or 7.4), regardless that the two types of ENMs have similar sizes and initial zeta potentials. Here we report a log K_{lipw} of ~3 for C_{60} aggregates that is ~ 3.5 orders of magnitude lower than the log K_{ow} value of 6.67 reported by Jafvert et al. for molecular C_{60}.[12] Once C_{60} molecules form aqueous aggregates, their property changes drastically. For example, molecular C_{60} is neutral, carrying no charge, while it is widely known and reported here that C_{60} aggregates are negatively charged. While neutral molecular C_{60} is not expected to be responsive to electrostatic interactions, C_{60} aggregates are, as suggested by our membrane-water distribution of nC_{60}, which is dependent on pH due to electrostatic repulsion.

We believe that the distribution of charged ENPs between water and lipid bilayers may be analogous to partitioning of ionizable organic compounds. Ionizable organic compounds are similar to the nanoparticles studied here in that they also exhibit pH-dependent charge behaviors in their interactions with lipid bilayers. It has been shown that chlorinated phenols[35,40] and some acidic pharmaceuticals[43] sorb more to phosphatidylcholine lipid bilayers at acidic pH (i.e., pH < pK_a's) where phenols are neutrally charged. Similar to the nanoparticles tested in this work, the sorption of phenols to lipid bilayers also exhibited mild saturation at higher phenol concentrations, especially at high pH, where sorbed phenoxides may accumulate a negative surface potential, leading to the rejection of anions.[35]

Environmental Implications

Bioconcentration factor (BCF), defined as chemical concentration measured in biota divided by chemical concentration measured in water, traditionally has been used to assess the bioaccumulation potential of chemicals.[61] Figure 15 shows our preliminary comparison of the lipid bilayer-water distribution of nC_{60} at pH = 7.4 from this study with existing bioaccumulation studies using *Daphnia magna* (i.e., water flea) at pH = ~7.[62-64] The data and calculation are also summarized in Table S1 in the appendices. The reported or estimated log BCF ranges are 2.98-4.40 (dry biomass based) and 3.67-4.16 (lipid content based). The daphnia-water distribution trend is qualitatively consistent with our lipid-water distribution data. Tao et al. reported that nC_{60} accumulated in biomass well correlated to the lipid content.[64] The single estimated lipid-based log BCF of 3.67-4.16 from Tao et al. compares well to our log K_{lipw} of 3.62 (estimated by Freundlich model) at similar exposure concentration. There are some quantitative differences between the lipid-water measurements and existing BCF studies that partially originate from variability in the test parameters used in the bioaccumulation studies including, exposure time (4-48 h), age of test organisms, exposure concentrations (0.1-30 mg/L nC_{60}), etc. In addition, the factor relating lipid content to biomass is system-specific (related to organism age)[64] and is not reported in all studies compared, suggesting that lipid content to wet or dry biomass is needed to provide more quantitative comparisons.

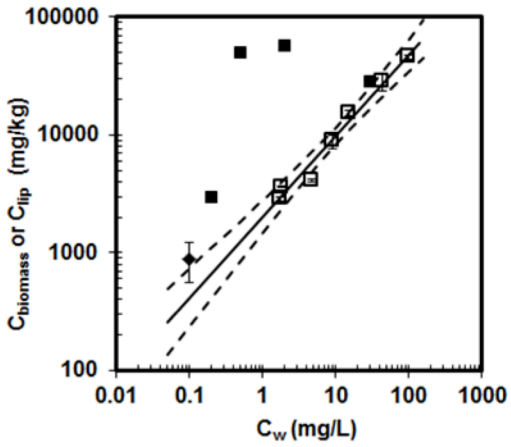

Figure 15. Preliminary comparison of lipid bilayer-water distribution of C_{60} aggregates (nC_{60}) measured at pH = 7.4 from this study with existing bioaccumulation studies of nC_{60} under similar solution chemistry, indicating data (□) from this report with the line representing the fitted Freundlich isotherm as well as organism (water flea, *Daphnia magna*)-water distribution data ($C_{biomass}$ versus C_w). $C_{biomass}$ is the mass of nC_{60} accumulated in daphnia normalized by daphnia biomass (i.e., mg nC_{60}/kg biomass) based on dry weight (■), or lipid content (♦). Bioaccumulation data are from reference[62-64] with all studies using *Daphnia magna* as test organisms. Dashed lines indicate 95% confidence interval.

In our previous work, we quantified the interactions of nC_{60} and fullerol with heterotrophic bacteria wastewater biomass. We showed that nC_{60} was removed by biosorption to the biomass to a greater extent than fullerol, which is qualitatively consistent with the current observations for SSLMs.[65] The biomembrane-water distribution similar to what we report here has been linked to the toxic action of narcosis (i.e., baseline toxicity), which is induced by the nonspecific disturbance of membrane integrity and functioning by chemicals.[66] The study of nanotoxicology is in its nascent stage and more research is needed to elucidate the toxicity mechanisms. The strong nC_{60} interactions with lipid membranes are generally consistent with toxicity studies on human cell lines, bacteria, and fish indicate that nC_{60} was more toxic than fullerol.[67-69]

Part 2: Lipid bilayer-water distribution of functionalized gold nanoparticles

Interaction of Au NPs with Lipid Bilayers We conducted experiments to demonstrate that the lipid bilayer governed the association between Au NPs and the TRANSIL product. Under our typical experimental conditions (pH = 7.4), 10 to 60% of the gold from the aqueous solution distributed onto the SSLM phase. Calculations based upon the surface area of Au NPs and SSLM indicated that < 2% of SSLM surface was occupied by Au NPs under these experimental conditions which we interpret as insignificant to limit steric hindrances or other interactions between Au NPs on the surface and in the aqueous solution. To support these calculations, SEM images of Au NPs on the SSLM indicate that individual Au NPs were present on the bilayer surface and well distributed across the SSLM surface (Figure 16). This is consistent with our separate measurements of the Au NP sizes in the same solution chemistry, which indicate that Au NPs remained non-aggregated throughout the interaction time periods. (Figure S7)

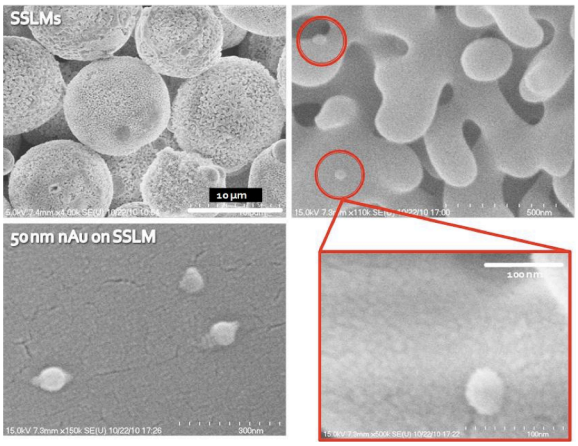

Figure 16. SEM images of 50 nm tannic acid Au NP adsorbed onto the supported lipid bilayers.

The effect of solution pH and reversibility was probed to further understand the association of Au NPs with SSLM. Figure 17 illustrates a higher fraction of Au NPs (10 nm, tannic acid coated) associated with the SSLM at pH = 5.0 compared with pH = 7.4. The zeta potential of Au NPs and SSLM in the pH = 7.4 electrolyte solution were both negative (both -15 mV to -20 mV), and but lower (i.e., less negative at -6 mV to -10 mV) at pH = 5. The greater association of Au NPs and SSLM at pH = 5.0 may be attributable to the reduction in electrostatic repulsion as measured by the smaller zeta potentials (i.e., less negative) of Au NPs and SSLM.

We investigated the potential for Au NPs to disassociate from the SSLM by changing the aqueous solution in the same vials. First, we exposed the SSLM to Au NPs. Then we moved the Au NP-associated SSLM to an identical electrolyte solution without Au NPs. After shaking, less than 5% of the Au NPs dis-associated from the SSLM back into solution. The Au NP-associated SSLM was washed with a higher pH solution (pH = 8.6, 5 mM phosphate) to possibly promote charge repulsion without damaging the lipids. Very little gold mass (< 5%) was measured in the high pH solution suggesting insignificant disassociation of Au NPs from the SSLM. The irreversibility of the association of 10 nm Au NP and lipid bilayers can

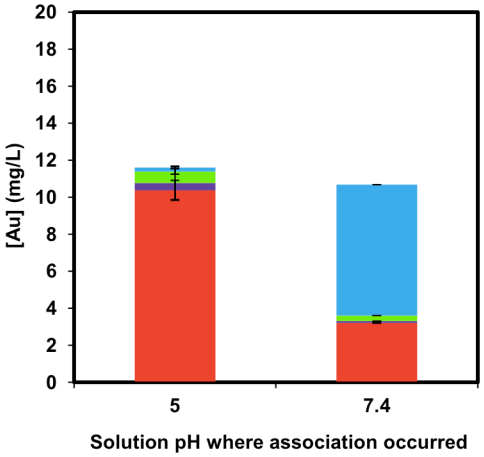

Figure 17. Association and disassociation of tannic acid Au NPs with supported lipid bilayers (SSLM) at two pH conditions. Initial aqueous [Au] = ~10 mg/L. The blue bars indicate the free Au NP concentration at apparent equilibrium after 4 h. The green and purple bars indicate the mass of Au NP extracted from the Au NP-associated SLM following initial sorption by original electrolytes w/o Au NP and pH = 8.6 buffer electrolytes, sequentially. The red bars denote the Au NP concentration remained associated with SSLM after sequential extractions.

be explained by the interaction energy modeled using the DLVO theory, which considers the electrostatic and van der Waals forces. The detailed model calculation is presented in the appendices. Figure 18 shows the interaction energy of various sizes of NPs as a function of their distance from the SSLM surface. The energy barrier between the 10 nm Au NP and lipid bilayers at pH = 7.4 is very small suggesting that the association of Au NP with lipid bilayers likely falls in the primary energy minimum.[18] Prior studies have shown that nanoparticles depositing in the primary energy minimum are less likely to release from the surface due to strong attractive interaction,[70] which correlates with our observations for 10 nm Au NPs associated with lipid bilayers.

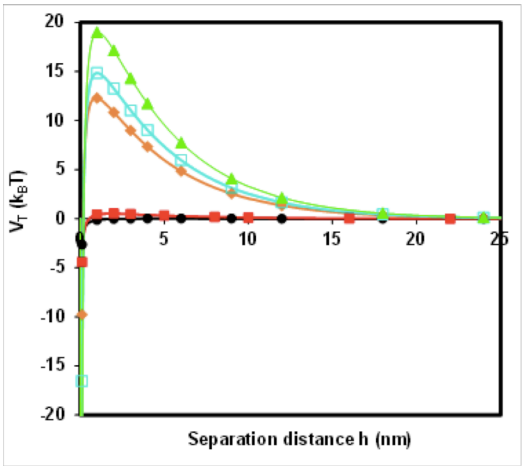

Figure 18. Interaction energy between Au NPs and lipid bilayers at pH = 7.4 modeled by the Derjaguin, Landau, Verwey and Overbeek (DLVO) theory, indicating the interaction energy as a function of separation distance between Au NPs with sizes of 5 (●), 10 (■), 50 (♦), 70 (□), and 100 nm (▲).

Nanoparticle-Lipid Bilayer Distribution Kinetics The distribution kinetics for the five Au NPs at a constant SSLM mass, and similar initial gold concentrations (8 to 10 mg/L), is presented in Figure 19a. The concentration of gold distributed into the SSLM, C_{lip}, increases over time for all sizes of Au NPs and then plateaus at a constant C_{lip}. The increase in C_{lip} is matched with a concurrent decrease in aqueous phase gold concentrations, which was independently measured (not shown). The control samples containing Au NPs alone revealed no decrease in gold concentrations (not shown). Under the conditions tested, constant distributions between Au NPs and the SSLM were achieved in less than 4 h for 5, 10 and 50 nm Au NPs and slightly longer, but less than 24 h, for 70 and 100 nm Au NPs (Figure 19a).

The distribution kinetics can be fit with an empirical model developed to describe the adsorption kinetics of different sized iron oxide nanoparticles to mammalian cells given as

$$\frac{dC_{lip}(t)}{dt} = k_a C\left[C_{lip,0} - C_{lip}(t)\right] - k_d C_{lip}(t) \quad (3)$$

where C_{lip}(t) is the distributed gold mass per unit mass of lipid (mg Au/kg lipid) as a function of time, t is time (h), k_a is the association constant (L/mg/h), k_d is the dis-association constant (1/h), C is the initial Au NP mass concentration applied (mg/L), and $C_{lip,0}$ is the maximum mass of Au NP that can distribute to lipid bilayer (per unit mass of lipid).[71,72] Here, we use $C_{lip,0} = 3.63 \times 10^9$ (mg/kg lipid), which corresponds to 20,000 (mg/m^2) used in previous cell studies.[72] Solving equation 3 yields equation 4.

$$C_{lip}(t) = \frac{k_a C C_{lip,0}}{k_a C + k_d}\left(1 - \exp[-(k_a C + k_d)t]\right) \quad (4)$$

τ (= $1/(k_a C + k_d)$) is the characteristic time (h), indicative of the overall rate of interactions (i.e., association and dis-association) between lipid bilayer and Au NPs.[72,73] A smaller τ value indicates the more rapid interactions. Best fits of the data with equation 4 presented in Figure 19a. The model generally fits the size dependent trend observed in the data. However, the kinetics were too fast to quantify for the smaller sized Au NPs based upon experimental conditions (preparation of vials, dispersion and mechanical mixing) which required at least 20 min before the first sample could be collected. Nevertheless, fitted values for the τ are smallest

for the 5-nm diameter Au NP (0.19 h) compared against the 70 or 100 nm Au NPs (3.38 and 3.76 h, respectively), indicating that smaller Au NPs associate with lipid bilayer more rapidly.

Understanding the size dependent kinetics of Au NP distribution on SSLM may provide insight into appropriate dosimetric selection for nanomaterial studies. Figure 19a shows that larger sized Au NPs accumulate to a greater extent on SSLMs than smaller diameter Au NPs. Conversely, plotting the same data on a number concentration basis (Figure 19b) rather than a mass concentration basis (Figure 19a) shows that the largest number of Au NPs distributed actually have the smallest diameter. Figure 19b clearly shows that rate and extent of Au NPs accumulation increases and reaches higher accumulation as the diameter decreases.

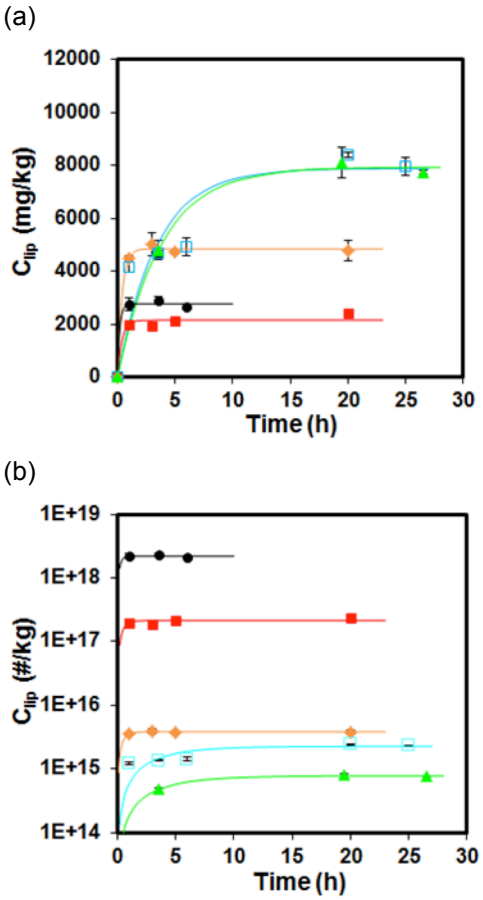

Figure 19. Association kinetics of tannic acid Au NPs of different sizes at 5 nm (●), 10 nm (■), 50 nm (♦), 70 nm (□), and 100 nm (▲) with supported lipid bilayers (SSLM) at pH = 7.4, indicating Au NP accumulation to SSLM based on mass (a) or number (b) of particles. The initial Au NP concentration was 8-10 mg/L. The lines in Figure 4a represent the fit to equation 4 and the lines in Figure 4b are meant to guide the eye.

The association kinetics of SSLM and Au NPs can be considered as a two-step process, consisting of the transport of Au NPs to the proximity of lipid bilayer surface (i.e., collision) followed the surface interaction between Au NPs and lipid bilayers. We modeled the particle transport rates in our system using the classical Smoluchowski equations considering collisions induced by perikinetic and orthokinetic transport as well as differential sedimentation.[74] The detailed model calculation is presented in the appendices. The results suggest that small Au NPs collide with supported lipid bilayers more frequently. Since particle number concentration is the relevant unit of the collision model, it correlates with the experimental data presented in Figure 19b, which shows that smaller Au NPs accumulate to supported lipid bilayer at a higher rate.

The interaction between lipid bilayers and Au NPs impact the association rate after their collision. The classical colloid theory (i.e., DLVO theory) has been increasingly applied to examine the nano-bio interactions.[31,75] We calculated the interaction energy between SSLM and different sized Au NPs based on the DLVO theory and the results are presented in Figure 18. Figure 18 indicates that smaller sized Au NPs have a lower energy barrier to associate with SSLM than larger ones. This is consistent with our observations that smaller Au NP distributed to SSLM at a higher rate (by number concentration) as shown in Figure 4b. Although the interaction energy modeled using DLVO theory accounting for electrostatic and van der Waals interactions qualitatively correlates with our observations, a more rigorous comparison including additional forces such as sterics could be considered.[31] Collectively, these simple analyses of particle transport and interaction energy between Au NP and SSLM qualitatively rationalize the distribution kinetics of different sized Au NP to SSLM. This also suggests that number

concentration, along with Au NP diameter, may be the appropriate dosimetric parameters for mechanistically describing the observed kinetics of Au NP distribution on SSLM.

Effects of Au NP Diameter and Surface Coating Experiments for a variety of Au NP diameters and initial concentrations were run until a constant distribution between SSLM and water phases were achieved based upon the kinetic experiments. The results are presented in Figure 20 for independent measurements of gold in the aqueous phase C_w and lipid phase C_{lip}. A best fit line through the data yields a slope ($K = C_{lip}/C_w$) with the units of L/kg that we define as the distribution coefficient. From Figure 20a, the mass concentration dependent distribution coefficient ($K_{lipw,mass}$) for the Au NPs on SSLM is 454 L/kg (95th percentiles for the slope are 400 and 508 L/kg; R^2 = 0.73; n = 102). This implies that higher aqueous phase concentrations of Au NPs lead to greater, but proportional, association of Au NPs on SSLM. Figure 20b shows the same experimental data but plotted on a number concentration basis, and yields a number concentration dependent distribution coefficient ($K_{lipw,\#}$) of 450 L/kg (95th percentiles for the slope are 437 and 464 L/kg; R^2 = 0.98; n = 102). While statistically there is no difference in the K value obtained between the two dosimetry approaches, the improved statistical fit of the data (based upon R^2 values) using number concentration dosimetry implies that the variation in $K_{lipw,mass}$ can be explained by the Au NP diameter, because all other characteristics of the homologous series of Au NPs are comparable. If you ask how can this be? The units of K_{lipw} (L/Kg) are independent of mass or number concentration of the Au NPs themselves.

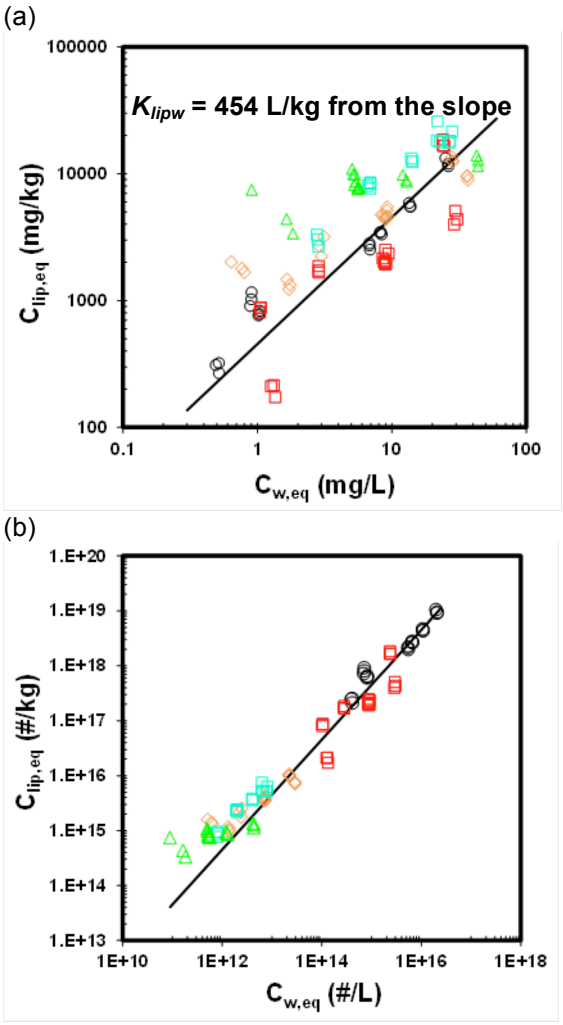

Figure 20. Lipid bilayer-water distribution of tannic acid gold nanoparticles (Au NP) with sizes ranging from 5-100 nm at pH = 7.4, indicating the distribution of 5 nm (○), 10 nm (□), 50 nm (◊), 70 nm (□), and 100 nm (Δ) Au NPs based on mass concentration (a) or number concentration (b).

We also examined the role of surface functionality using 10 nm Au NP. We use tannic acid and PVP functionalized Au NPs which have nearly the same zeta potential in our pH buffer electrolyte (see Figure S9). The hydrodynamic diameter of the PVP Au NP is marginally greater than the tannic acid Au NP. We exposed Au NP to SSLM at several initial gold dosages of 1 to 30 mg/L and found that the mass of gold distributed to the SSLM was less for the PVP Au NP than for the same diameter tannic acid Au NP especially at higher mass concentrations. $K_{lipw,mass}$ for PVP Au NP is approximately half that for tannic acid Au NP. We associate the difference in distribution coefficient with steric interactions between the PVP and SSLM. Similar observations have also been reported for reduced PVP silver nanoparticle uptake by epithelial cells compared with citric acid functionalized silver nanoparticles.[76]

Summary Recently, nanomaterial research started using homologous series of nanoparticles where only one attribute is varied at a time (e.g., size, functionality, aspect ratio).[51,73,75] Data presented in Figure 20b also raise an important observation about experimental design for experiments using homologous series of

nanomaterials. Most of the experiments we report cover one order of magnitude, or slightly more, in mass concentrations, but this results in nearly 8,000 fold differences in initial number concentrations between the 5 and 100 nm Au NPs. While we attempted to design experiments that had comparable number concentrations, this proved exceedingly difficult because the initial concentration of the larger sized Au NPs was above our stock solution gold concentration, and likewise diluting the smaller Au NPs to a low number concentration ran into analytical detection issues by the ICP-OES. Thus, we conclude that designing experiments with equal number concentration dosimetry is exceedingly challenging regardless of the model (e.g., SSLM) being investigated. However, the promising outcome is that the K_{lipw} approach is actually independent of mass or number dosimetry over the conditions tested here. The lipid bilayer-water distribution of ENPs will result in two journal publications:

Hou, W.-C.; Moghadam, B.; Westerhoff, P.; Posner, J. D. Distribution of Fullerene Nanomaterials between Water and Model Biological Membranes. *Langmuir*, accepted in press.

Hou, W.-C.; Moghadam, B.; Corredor, C.; Westerhoff, P.; Posner, J. D. Distribution of Functionalized Gold Nanoparticles between Water and Model Biological Membrane. In preparation.

3. Engineering nanomaterial disruption of model cell membranes

Recent toxicological studies have suggested that ENPs can cause the disruption of live cell membranes, leading to the leakage of intracellular contents (e.g., enzymes) and likely subsequent internalization of ENPs. While the observations are important, the mechanism underpinning the ENP-cell interaction is far from clear. The cell membrane is a complex environment consisting of lipid bilayers, the major component at this dynamic interface, that are embedded with a wide variety of membrane proteins and receptors functioning together with the bilayer to regulate the chemical flux across the cell membrane. To gain a fundamental understanding of the nano-bio interactions, it is essential to probe the interaction at the critical interface one component at a time. Lipid bilayers are common to cellular life. Studying the lipid bilayer-ENP interaction is the first step towards a mechanistic understanding in the nano-bio interface interaction that will shed light on the nanotoxicity. In this project, we also examined the effect of ENPs on the lipid bilayer disruption. Specifically, we developed two assay methods which are described in section 3.1 and 3.2, respectively, to probe how ENP-bilayer interaction leads to the malfunction of lipid bilayers in regulating the fluxes of ionic charges and molecules.

3.1 Electrophysiology assay

The electrophysiological measurement using the patch-clamp technique is capable of probing defects at the membrane level by examining the electrical current passing through the perturbed membranes. Due to its great sensitivity, the technique has been widely used to examine the activity of membrane ion channel proteins and the membrane permeabilizing effect of toxic peptides (e.g., melittin).[77] Only very recently has the patch-clamp technique begun to be employed to probe the interaction of live cells or lipid bilayer with ENPs. Chen et al. indicated that cationic polymeric ENPs can cause nanoscale pore formation on live mammalian cells, leading to the breach of current fluxes.[78] Ramachandran et al. indicated that water soluble CdSe/ZnS quantum dots (QD) evoke current fluctuations across lipid bilayers. They suggested that QDs are embedded into lipid bilayer, forming pore through which current fluxes occur.[79] This is in line with our previous report showing that CdSe QDs induce similar current bursts attributable to QD self-aggregation on suspended lipid bilayers as revealed by fluorescence microscopy.[80]

In this section, we report the first study, to the best of our knowledge, on the interaction of functionalized multi-walled carbon nanotubes (*f*CNTs) with 1,2-dioleyl-sn-3-phosphatidylcholine (DOPC) lipid bilayers using the patch-clamp technique. We used multi-walled carbon nanotubes, because they are promising for a variety of potential applications including biomedicine, nanocomposites, energy conversion, etc. Multi-walled carbon nanotube is also the carbonaceous nanomaterial with the highest annual production volume worldwide. We developed a fractional event interaction (FEI) and average conductance techniques to provide a more quantitative description for the lipid bilayer and nanoparticle interaction. We compared the lipid bilayer disruption behavior of *f*CNTs with QDs and melittin, a well-known pore forming peptide.[81] We also examined lipid bilayer permeability as a function of nanoparticle concentrations.

Experimental Section

Materials. Carboxyl quantum dots (QDs, CdSe/ZnS) were purchased from Invitrogen (Eugene, OR). Functionalized multi-walled carbon nanotubes (*f*CNTs) were the consortium material received from Prof. Somenath Mitra at the Department of Chemistry and Environmental

Science at the New Jersey Institute of Technology. 1,2-dioleyl-sn-3-phosphatidylcholine (DOPC) lipid was purchased from Avanti Polar Lipids (Alabaster, AL). Melittin was obtained as dry powders from Sigma Aldrich (≥ 97%, St. Louis, MO). Other chemicals were of the highest purity available and used as received. All aqueous samples were prepared using water purified with a Milli-Q Advantage A10® system (Millipore Corp., Billerica, MA).

Nanoparticle and Lipid Bilayer Dispersions. To avoid the perturbation on lipid membrane, no surfactants or other nanoparticle dispersion stabilizing chemicals were used in our experiments. The *f*CNTs stock solution was prepared by dispersing dry *f*CNT powder in pure water with mild sonication (2510DTH, Branson Ultrasonic Corp., Danbury, CT) for 1 h. We dissolved melittin in the HEPES buffer (20 mM) at pH = 7.4. The resulting stock solution (5 mg/mL) was then frozen and kept at -20°C. The melittin sample was thawed in 23°C prior to use. To measure the effective zeta potential of DOPC lipid bilayer, we prepared lipid bilayer vesicles (i.e., liposomes) with composition identical to suspended lipid bilayers used in electrophysiological measurements. The liposomes were prepared following a literature method.[48] Briefly, dry DOPC lipid powder was dissolved in chloroform prior to placing in test tubes and drying under N_2. The resulting lipid film was hydrated with the HEPES buffer electrolyte (20 mM with 20 mM KCl) under vortex mixing to form multilamellar liposome suspensions. The suspensions were passed through polycarbonate membrane filters with a pore size of 100 nm held within a commercial extruder (LIPEX, Northern Lipids Inc., BC, Canada) 11 times to obtain unilamellar liposomes.

Electrophysiological Measurements. We have examined the interactions of nanoparticles with suspended lipid bilayer membranes using electrophysiological measurements by continuously monitoring the current across the suspended lipid bilayer membrane employing the patch-clamp type of measurements. A schematic diagram of the measurements setup is shown in Figure 21. As shown in Figure 21, a polystyrene reservoir divided by a wall into two compartments (i.e., cis and trans) with each compartment having a 3 ml working volume (Warner Instruments Inc., Hamden, CT) was used to hold the experimental solutions. An aperture with a size of 150 µm in diameter located in the center of the division wall was used to suspend the lipid bilayer. We measure the bilayer current flux by the Ag/AgCl electrode which was immersed into each well and connected to the low noise Heka extracellular patch clamp amplifiers (EPC8, HEKA Instruments Inc., Bellmore, NY) Also, a positive charge flowing the trans to the cis compartment is plotted as positive current. All experiments presented in this paper were conducted at room temperature (~20°C).

The suspended lipid bilayer was primed and painted across a 150 µm aperture using the conventional Montal-Mueller technique.[82] The DOPC solution used to paint the lipid bilayers was prepared as follows: a 0.4 mL DOPC (10 mg/mL) in chloroform solution was placed in a test tube and dried by a gentle stream of pure N_2 gas and left in a desiccator overnight. The dry lipid film was reconstituted in 1 mL of decane. The DOPC lipid solution was freshly prepared immediately prior to every use

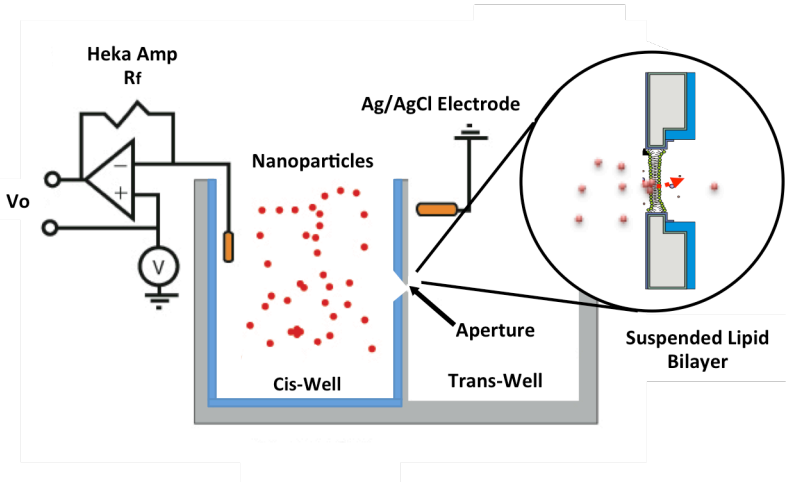

Figure 21. Patch clamp electrophysiological current measurements of DOPC lipid bilayers.

to minimize potential variability in the lipid membrane permeability. Next, a volume of 3 mL buffer electrolyte at pH = 7.4 (20 mM HEPES and 20 mM KCl) was added to each well in a way such that there was not differential hydrostatic pressure across the bilayer. After confirming the bilayer existence, we initiated experiments by adding nanoparticles to the cis reservoir. We examined the existence of a proper suspended lipid membrane by applying a 500 mV current pulse to rupture the bilayer. A true bilayer will exhibit a high capacitance of ~10 GΩ due to its thin (~4 nm) thickness[52] and the ability to be ruptured with a high voltage pulse delivered by the HeKa amplifier.

The current flux data was recorded over time when the nanoparticle-lipid bilayer interaction was occurring with a low-pass, 8-pole Bessel filters at 60 kHz and sampled at 10 kHz by Texas Instruments computerized analog-to-digital converter and processed with an in house Matlab computer program.

Characterizations. The sizes and zeta potentials of nanoparticles, melittin, and liposomes were determined on a dynamic light scattering (DLS) particle sizer (NICOMP 380 ZLS, Particle Sizing Systems, Santa Barbara, CA) that uses a laser light at 635 nm.

Results and Discussion

Nanoparticles and Suspended Lipid bilayers We have thoroughly characterized the nanoparticles and lipid bilayers used in the studies. The *f*CNTs are a well-characterized consortium material whose physicochemical properties have been documented in a previous report.[83] The *f*CNTs have an outer diameter of ~25 nm, an inner diameter of ~8 nm, and a length of 10-30 μm. The purity of the material is greater than 95% by weight as carbon nanotubes with no measurable metal catalyst impurity. The major functionality of *f*CNTs is carboxyl groups. We have measured the effective hydrodynamic sizes and zeta potential for these materials at pH = 7.4 (20 mM HEPES and 20 mM KCl) over the 60 min of time period, during which typical interaction experiments were performed. The electrolyte composition was chosen because it was high enough to allow the measurement of current fluxes, while not causing serious nanoparticle aggregation according to our preliminary tests. We found that the zeta potential remained fairly constant throughout the recorded time period at -16.0 ± 0.7 mV for *f*CNTs, -9.8 ± 1.1 mV for QDs, 13.4 ± 1.1for melittin, and -12.1 ± 1.5 mV for DOPC lipid bilayers. Similarly, *f*CNTs and QDs maintained a constant effective hydrodynamic size of 112.0 and 12.7 nm, respectively, over the 60 min time period. Taken together, the data suggest that the nanoparticles remain stable in all our experimental conditions.

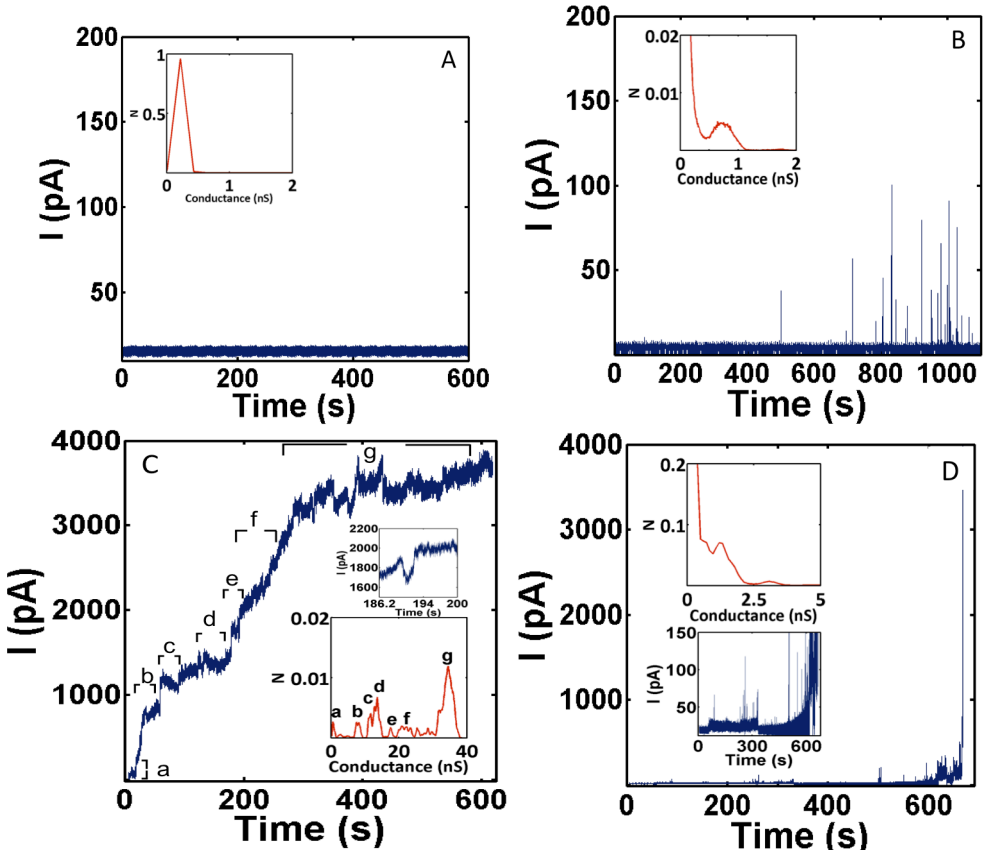

Figure 22. Interactions of nanoparticles (6 ppm) with DOPC lipid bilayers at pH = 7.4 (20 mM HEPES and 20 mM KCl), indicating the current-time traces of the patch-clamp measurements and normalized conductance distribution histograms (insets) in the absence of nanoparticles in the system (A), or in the exposure of carboxyl quantum dots (B),or functionalized carbon nanotubes (C). Melittin (6 ppm), a well-known pore forming peptide on lipid bilayers, was used for comparison under the same solution chemistry. (Figure 1D)

Interactions of Lipid Bilayers and Nanoparticles Figure 22 reports a set of representative nanoparticle and suspended lipid bilayer interactions. The lipid bilayer is a well-known biological barrier against ion conductance.[82] In the absence of nanoparticles (Figure 22A), the current passing through the lipid bilayer was very low at ~8 pA at an applied voltage of 100 mV and remained steady in a period of ~600 s. The lipid membrane created an exceptional ion flux seal with a resistance of ~8 GΩ as measured by utilizing a ramp voltage. The low bilayer current flux is consistent with prior studies.[80] The low current flux also confirms that a suspended lipid bilayer has properly formed on the on the working aperture. Our additional studies indicate that this suspended lipid bilayer can be stable and maintain its low permeability for ~20 h, with no changes in the current flux. The inset figure reports the probability (i.e., N) distribution of all current flux events (with magnitudes represented by conductance on the x-axis) integrated over the current trace plot. Conductance is the ratio of the current flux through the bilayer over the applied voltage (i.e., 100 mV). The inset in Figure 1A displays a single peak spanning from 0 to 0.25 nS, which represents the background interactions consisting of the intrinsic ion permeability of the lipid bilayer and instrument noise under the applied electric field.

Upon the addition of carboxyl QDs (6 ppm), we observe a distinctive change in the current time trace as shown in Figure 1B. Initially the current flux remained steadily low similar to that observed in the control experiment (Figure 22A), indicating that a suspended lipid bilayer

has formed an ion seal and that QDs have not been in contact with the bilayer. The first set of current bursts was observed at 500 s with an event time duration of ~200 ms and maximal current amplitude of 40 pA. The current bursts induced by QDs occurred only sporadically with no clear trend. 210 s after the first interaction, we observed larger and more frequent current fluctuations between 15 to 105 pA with an average about 60 pA. Throughout the experiment (i.e., ~1000 s), the QDs did not cause a complete lipid bilayer breakdown. The inset conductance histogram of Figure 1B presents a single, small, and broadened peak centered at ~0.8 nS in addition to the sharp peak (with N going up to ~1, not shown in the current scale) resulting from the background interactions similar to the one observed in the control experiment (Figure 22A). The peak at 0.8 nS represents the probability distribution of the current burst events induced by QDs. Clearly, the interaction of QDs with the suspended lipid bilayer has led to the enhanced current permeability across lipid membrane in an intermittent manner as revealed by the sporadic current spikes in Figure 22B. It has been suggested that the current fluctuations can be attributed to the oligomeric aggregation of QDs onto the bilayer that may create nanopore defects on the lipid bilayer, through which ion transport occurs.[84] Previously, it has been shown that carboxyl polymeric nanoparticles can create pores on supported lipid bilayers,[85] which correlates our observations on enhanced current fluxes. It is likely that the transient defects induced by carboxylated QDs open and close, leading to the sporadic current bursts.

Figure 22C reports the current flux across the suspended lipid bilayer created by *f*CNTs at 6 ppm. In contrast to QDs, *f*CNTs interact with the suspended lipid bilayer more rapidly and in a stepwise manner. The faster interaction of *f*CNT may not be reflective of its intrinsic transport behavior to the bilayer, as we mixed the *f*CNT suspension in situ with a stirring bar for 5 s before recording the current flux. The mixing procedure was necessary as *f*CNTs readily settled to the bottom. *f*CNTs create an immediate current increase to ~50 pA followed by a short plateau lasting for ~4 s. Subsequently, we observed a drastic escalation of current to 950 pA during an 11-s time lap. After this event, the current remains constant for 20 s and then rapidly increases to 1200 pA. While the increase in current flux followed a stepwise manner, each step possessed different magnitude. For example, the first current increase was at 50 pA followed by 950, 1200, 1400, 1800, 2150, and 3200 pA, labeled as A-F correspondently. Eventually, the current flux reached 3650 pA and a complete disruption of the membrane occurred after ~600 s of exposure. The conductance histogram (Figure 1C inset) shows multiple conductance peaks ranging from 0.26 to 36.5 nS corresponding to the current steps in Figure 22C. The mechanism in causing the intense and stepwise increase in bilayer current flux by *f*CNTs is currently unclear. It is likely that *f*CNTs insert and traverse the lipid bilayer, forming transmembrane channels that transport ions in an applied electric field. Prior studies have shown than CNTs can insert or passively diffuse (i.e., endocytosis independent) across cell membranes.[86,87] Computational studies also suggest that CNTs can diffuse and be embedded perpendicularly across lipid bilayers.[88] Given the known capability of CNTs to conduct electric charge,[89] ionic charges are likely to transport through the inserted *f*CNTs across the suspended lipid bilayer, leading to the observed current flux. Recent simulation studies have indicated that CNTs embedded in lipid bilayers can conduct ions through lipid bilayers.[90,91] Currently, there is no known experimental work on the ion conduction behavior of CNTs embedded in bilayers. The closest experimental work is that by Choi et al.[92,93] where two electrolyte wells were connected by CNTs embedded within resins and the ion flux was monitored by the patch-clamp technique. They showed that current flux occurred with quantized current fluctuation behavior similar to the observations in biological ion channels.[93,94] This is analogous to our observation of the local current flux pattern for the *f*CNTs and lipid bilayer interaction (Figure 22C inset). In contrast to the relatively steady fluctuation within a specific range, our system highlights a more dynamic current flux that increases over time. This may be attributed to the increased association of the suspended lipid bilayers with *f*CNTs from the aqueous phase, thereby creating additional channels for ion

transport over time. The investigation of the mechanism in causing the bilayer current flux is ongoing work in our lab.

Figure 22D reports the current flux across the suspended lipid bilayer created by 6 ppm melittin, a well-known pore-forming peptide for lipid bilayer membranes.[81] After 10 s of melittin exposure, we observed an initial sharp current burst (~60 pA) that lasted for 90 ms. Next, a current step with an average of 80 pA in amplitude occurred at 83.5 s and lasted for ~700 ms. Afterwards, the melittin and lipid bilayer interactions as represented by the current bursts became more intensive and larger in magnitude. At ~600 s, the membrane integrity collapsed due to the intensive current fluctuations with a maximum current at ~580 pA. The conductance histogram (Figure 22D inset) shows two distinctive conductance peaks at 1.2 and 3.1 nS corresponding to the current steps (as shown in the close-up current traces plot in the inset) and multiple current bursts observed in Figure 22D. The results are consistent with previous studies that demonstrate the disruptive capabilities of melittin to suspended lipid bilayers.[81,95] It is suggested that membrane disrupting (i.e., pore formation) and permeabilizing properties (i.e., helical secondary structure) of melittin could be the cause of this particular current bursts behavior.[81]

Taken together, QDs, *f*CNTs, and melittin exhibit very different behaviors in the interaction with suspended lipid bilayers. In contrast to *f*CNTs and melittin, carboxylated QDs appear to interact with DOPC lipid membrane in a milder manner, as the overall current fluctuation magnitude was smaller than 100 pA, and no complete bilayer disruption occurred within the timeframe investigated. In contrast, *f*CNTs and melittin both completely disrupted the lipid bilayer in 600 s. While stronger interaction with melittin, melittin and QDs both induced sporadic bilayer current bursts, suggesting a similar interaction mechanism due to pore formation. The stepwise increase in bilayer current flux in the presence of *f*CNTs may be attributed to the formation of transmembrane *f*CNT ion channels.

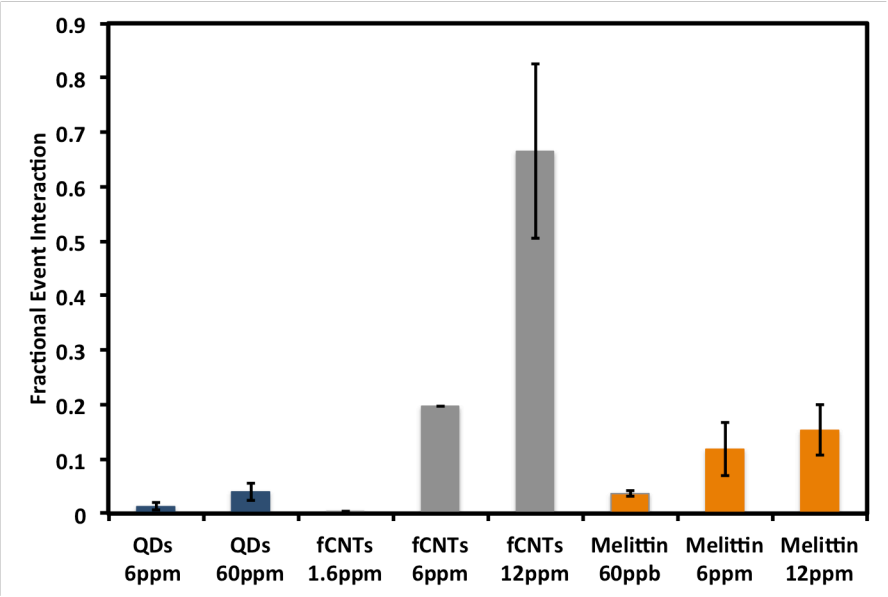

Figure 23. Interactions of nanoparticles with DOPC lipid bilayers at pH = 7.4 (20mM HEPES and 20mM KCl), indicating the fractional event interaction as a function of added nanoparticle concentrations.

Figure 23 compares the fractional event interaction (FEI) of QDs, *f*CNTs and melittin at numerous concentrations. The FEI technique is an approach that provides the quantitative information regarding the fraction of current flux events resulting from the lipid bilayer-nanoparticle interaction to all events (i.e., true and background interactions). The FEI is derived from the conductance distribution histograms as shown in Figure 22 insets. We divide the area under the peaks owing to nanoparticle interactions by the total area under the curve. A larger FEI for a particular particle indicates that the particle creates more interaction events with lipid membrane during an experiment. The FEI reported in Figure 23 are the average of at least triplicate experiments. As shown in Figure 23, the FEIs for QDs, *f*CNT, and melittin increase as

their concentrations increase, indicating that more particles create more interaction events. Comparing FEIs across the three particles indicates that *f*CNTs are most potent in interacting with lipid bilayers especially at higher concentrations, while melittin and QDs exhibit the intermediate and least interactions, respectively. The trend is consistent with the current traces shown in Figure 22. It appears that the aspect ratio plays a role, as tubular *f*CNTs with hollow interior interacts stronger with lipid bilayer than spherical QDs, although the core materials are also different for the materials. Figure 23 also indicates that the FEI for all three materials increases as the mass concentration increases. The concentration dependency can be attributed to a larger number of particles present at a higher mass concentration, which results in a greater probability of particle contact with the lipid membrane. Although melittin has a greater disruption effect for the lipid bilayer at a lower concentration of 60 ppb, *f*CNTs exhibit stronger interactions at 6 and 12 ppm.

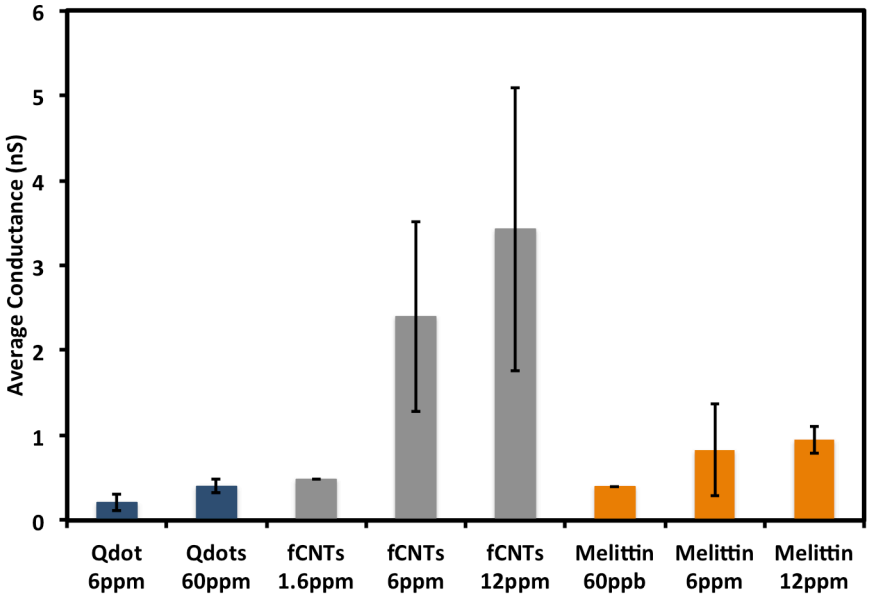

Figure 24. Interactions of nanoparticles with DOPC lipid bilayers at pH = 7.4 (20mM HEPES and 20mM KCl), indicating the average conductance as a function of added nanoparticle concentrations.

In Figure 24, we report the average conductance, which represents the average magnitude of all the lipid bilayer-nanoparticle interaction events integrated over a current trace plot. In Figure 24, the average conductance follows a concentration dependent trend across the three particles similar to FEI reported in figure 2. *f*CNTs interacting with lipid bilayer exhibit the highest average conductance ranging from 0.5 to 3.3 nS, and the average conductance increases as the mass concentrations increases from 1.6 to 12 ppm. QDs have the least membrane disrupting effect on lipid bilayers, as the average conductance is small from 0.20 to 0.45 nS corresponding to QD concentration of 6 to 60 ppm. Melittin has an intermediate interaction with lipid bilayer with an average conductance of 0.45 to 0.95 nS in exposure to melittin concentrations of 60 ppb to 12 ppm.

It should be noted that although the average conductance and FEI combined can allow a more quantitative analysis that captures the average interaction behavior of nanoparticle and lipid bilayers, it does not reflect the specific interaction patterns (i.e., sporadic spikes versus stepwise increase) and the eventual breakdown of lipid bilayer, which varies from particle to particle and can only be observed in the current time traces. Thus, for a comprehensive and unbiased understanding of the lipid bilayer and nanoparticle interaction, an analysis including the three pieces of information may be necessary.

This work will result in two journal publications:

SA Klein, SJ Wilk, TJ Thornton, & JD Posner. Formation of nanopores in suspended lipid bilayers using quantum dots. In: Journal of Physics: Conference Series.Vol 109. Institute of Physics Publishing; 2008:012022.

Corredor, C.; Hou, W.-C.; Klein, S. A.; Moghadam, B.; Goryll, M.; Westerhoff, P.; Posner, J. D. Electrophysiological Measurements to Detect Suspended Lipid Bilayer Disruption Induced by Nanoparticles. In Preparation.

3.2 Dye leakage assay

Another measurement of lipid bilayer disruption is based on detecting the leakage of fluorescent dye encapsulated into lipid bilayer vesicles (liposomes). Liposomes are artificial lipid bilayers that are self-assembled by lipid molecules into hollow spherical structure. They mimic the lamellarity, curvature, and fluidity of biomembrane and can be made of composition close to actual cell membranes. The method relies on detecting the fluorescence resulting from the release of dye pre-loaded into liposomes which are impermeable to dye when lipid bilayers are intact. The encapsulated dye does not fluoresce due to self-quenching of dye molecules at high concentration (generally > 100 mM) within the liposome. The increase in fluorescence intensity signifies that the lipid bilayer integrity has been compromised, leading to dye release into the bulk solution (i.e., dilution of dye concentration) and fluorescence recovery. Due to the relative simplicity of the method that requires no special equipment other than a common lab fluorometer and also allows for the possibility of high throughput assays,[96] it has been used extensively in probing the lipid bilayer response to stimulants such as melittin peptides and other biomolecules with lipid bilayers.[96-99]

In this section, we applied this complimentary measurement to evaluate the disruption of lipid bilayers interacting with nanoparticles. We examined the surface coating and charge effects for gold and TiO_2 nanoparticles with a similar size (~10 nm) on the disruption (as indicated by the dye leakage) of LUVs (~100 nm) consisting of DOPC lipids. We examined the leakage kinetics for liposomes interacting with gold nanoparticles (Au NP) of different surface functionalities and concentrations. We presented an in-depth analysis of the dosimetry of Au NPs interacting with liposomes by comparing the lipid membrane disruption based on nanoparticle mass concentration versus number density or based on nanoparticle to liposome mass or number density ratio. We also derived the nanoparticle dose needed to induce 50% leakage of liposomes for Au NPs and compared the value to that of melittin, a well-known toxic peptide that creates pores of lipid membranes.

Experimental Section

Materials. 1,2-dioleoyl-sn-glycero-3-phosphocholine (DOPC) dissolved in chloroform was purchased from Avanti Polar Lipids (Alabaster, AL). HEPES (≥ 99.5% pure) and melittin (96% pure) were obtained from Sigma Aldrich chemicals (Saint Louis, MO). We dissolved melittin was in the HEPES buffer (20 mM) at pH = 7.4. The resulting stock solution (5 mg/mL) was then frozen and kept at -20^{o}C until used. Triton X-100 was purchased from Fisher Scientific (Hampton, NH) and 5(6)-carboxyfluoresceine (CF) was obtained from Molecular Probes (Eugene, OR) and used without further purification. To facilitate CF crystals dissolution in water, the aqueous stock solution of 100 mM CF was prepared in 20 mM HEPES, adjusting to pH = 7.4 with KOH solution (10 M). Sodium polyacrylate coated titanium dioxide nanoparticles (TiO_2 NP), poly (diallyldimethylammonium chloride) (DADMAC) coated Gold nanoparticles (Au NP) and DADMAC coated TiO_2 NP were synthesized by Vive Nano (Toronto, ON). Tannic acid and polyvinylpyrrolidone (PVP) coated Au NPs (PVP Au NPs) were purchased from NanoComposix (San Diego, CA). All aqueous samples were prepared using water purified with a Milli-Q Advantage A10 ® system (Millipore Corp., Billerica, MA).

Liposome Preparation. We prepared liposomes following a literature method with slight modifications. 25 mg/mL solution of DOPC in chloroform was dried under a gentle stream of pure nitrogen, to create thin layers of dried lipid. The residual solvent was removed overnight in a desiccator. After drying, the lipid films were hydrated in HEPES buffer (pH 7.4, 20 mM) containing 100 mM CF. The lipid mixture was incubated for 1 h with occasional vortexing at a

temperature above the phase transition temperature of the phospholipid composition of liposomes (-19^{o}C). The lipid mixture were then subjected to five freeze-thaw cycles in liquid nitrogen and subsequently extruded 20 times through two polycarbonate membrane filters of 100 nm pore size (Whatman, Clifton, NJ) using the LIPEX extruder (Northern Lipids, Vancouver, BC). Untrapped CF was removed using 3kDa centrifugal ultrafiltration filters (Millipore Corp., Billerica, MA) and substituted with the same HEPES buffer without CF dye. The resulting liposome stock suspension had a final lipid concentration of 2.54 mM, as measured using the malachite green dye method.[49] To ensure the quality of the liposomes, the particle size distribution of the liposomes was checked by dynamic light scattering (DLS). No change in hydrodynamic diameter of liposomes was observed due to the ultrafiltration procedure. The prepared liposome suspensions were stored at 4^{o}C and used in 2 weeks.

Leakage Experiments. We performed dye leakage experiments by simply mixing CF dye encapsulated liposomes and nanoparticles. The liposome dispersion was diluted with 20 mM HEPES buffer in order to obtain a phospholipid concentration of 7.8 μM in the fluorometer cuvettes. The high concentration (100 mM) of the encapsulated CF dye led to self-quenching of its fluorescence, resulting in a low background fluorescence intensity of the vesicle dispersion (denoted as I_{min}). Afterwards, an aliquot of nanoparticle solution was added to dispersion in order to obtain desired NP/Lipid ratio. Release of dye caused by the addition of NPs led to the dilution of the dye into the medium outside the liposomes (and thus recovery of fluorescence) and could therefore be monitored by fluorometry. The measured fluorescent intensity in experimental samples was denoted as I_F. The result of leakage experiments are presented as the percentage of released dye, which is given by Percent Leakage = 100 × (I_F - I_{min})/(I_{max} - I_{min}). I_{max} represents the maximum fluorescent intensity upon the complete leakage of dye, which was induced by adding Triton X-100 (0.2 vol%) to each experimental sample after reaction. Triplicate samples were prepared for a certain NP/lipid ratio to ensure the reproducibility of the experiments.

Analysis The hydrodynamic sizes and zeta potentials of nanoparticles and liposomes were determined on a dynamic light scattering (DLS) particle sizer (NICOMP 380 ZLS, Particle Sizing Systems, Santa Barbara, CA) that uses a laser light at 635 nm. The measurements were done under a scattering angle of 90^{o} at 20^{o}C. All particle sizes are reported as intensity-weighted sizes.

For the leakage experiments we used a Perkin-Elmer, Model LS-5 spectrofluorometer (excitation and emission slit widths were 2.5 nm). CF was excited at 490 nm and emission was read at 517 nm.

Results and Discussion

Material Characterization We thoroughly characterized the nanoparticles and liposomes used in the study. We measured the hydrodynamic diameter and zeta potentials of Au(+) NPs (i.e., DADMAC functionalized), Au(-) NPs (i.e., tannic acid functionalized), PVP functionalized Au NPs, and DOPC liposomes under solution chemistry similar to that in which the interaction experiments of liposomes and nanoparticles were conducted (i.e., in 20 mM HEPES buffer electrolyte at pH = 7.4). The DLS measurements indicate that the hydrodynamic size and zeta potential of DOPC liposomes were 106.2 ± 4.4 nm and -12.1 ± 1.5 mV, respectively. All the three types of Au NPs have the same nominal size of 10 nm as reported by the manufacturers. The hydrodynamic size of Au(+) NPs, Au(-) NPs and PVP Au NPs were measured as 16.2 ± 2.1 nm, 18.2 ± 5.1 nm and 21.9 ± 7.2 nm, respectively, which are slightly larger than size revealed by TEM images (reported by the manufacturer) potentially due to the incorporation of surface coating or slight aggregation in the DLS measurements. Au(+) NPs

have a zeta potential of ~20.0 mV, while those of tannic acid and PVP Au NPs were both -35.0 mV.

Liposome Leakage Kinetics The influence of Au NPs on the permeability of DOPC liposomes was investigated using fluorescence quenching property of CF dye. We comprehensively examined the interaction kinetics of every experiment we report in the paper and Figure 25 shows the representative ones. Figure 1 reports the interaction kinetics of liposomes and Au NPs with different surface functionalities and charges at various mass concentrations. Au(+) NPs induce liposome leakage in a time-dependent manner. For example, Au(+) NPs at gold to lipid mass ratio (NP/L) of 0.02 induced CF leakage at an initial rate (i.e., linear region) of 49% per hour and gradually reached a plateau at 97% leakage after 6 h. The leakage rate of liposome is also concentration-dependent on gold mass, with a slower rate occurring at a lower gold concentration. At NP/L mass ratio ≤ 0.15, the leakage rate decreased from 35% per hour to 3% per hour at NP/L of 0.002. At NP/L of 0.002, the leakage was very close to that in the control experiment, in which Au(+) NP was absent, indicating the liposome-Au(+) NP interaction is insignificant at this ratio. In the control experiment, leakage still occurred, but at a much smaller rate, which can be attributed to the natural decay of liposomes. This also indicates that Au(+) NP is required over a threshold NP/L ratio (i.e., 0.002) to mediate liposome leakage.

In Figure 25, we also compare the leakage kinetics of liposomes in the presence of Au(+) NP versus melittin, a well-known toxic peptide that creates pores on lipid membrane.[100] While Au(+) NP interaction with vesicles reached an apparent equilibrium after 6 h (at NP/L ratio of 0.005), it took much shorter time (i.e., < 30 min) for melittin at an equivalent mass ratio to cause complete leakage. One potential reason for the faster kinetics of melittin may be that it has a smaller size (2.5 ± 1.4 nm in 20 mM HEPES at pH=7.4 according to our DLS measurements), thereby transporting faster to liposomes. Melittin has the diffusivity of 1.92×10^{-10} m^2/s (based on the Stokes-Einstein equation), which is approximately one order of magnitude higher than that of Au(+) NP with a hydrodynamic diameter of 16 nm. Our melittin result is consistent with an earlier study,[101] which shows that melittin induced 100% leakage from CF dye-loaded DOPC vesicles more rapidly in 7 min at a higher NP/L of 0.09. The leakage induced by Au(+) NPs at NP/L = 0.005 was not complete, reaching a steady state leakage at ~40% after 6 h as opposed to ~100% leakage by melittin, indicating that the liposome–Au NP(+) interaction is limited by Au NPs. In a related study, Goodman et al. reported that 2 nm Au(+) NPs at 43 ppb induced a 20% steady state leakage from 1μm negatively charged vesicles (L- α-stearoyl-oleoyl-phosphotidylcholine (SOPC) and L-α-stearoyl-oleoyl-phosphotidylserine mixture (SOPS)) after 5 min,[102] while our

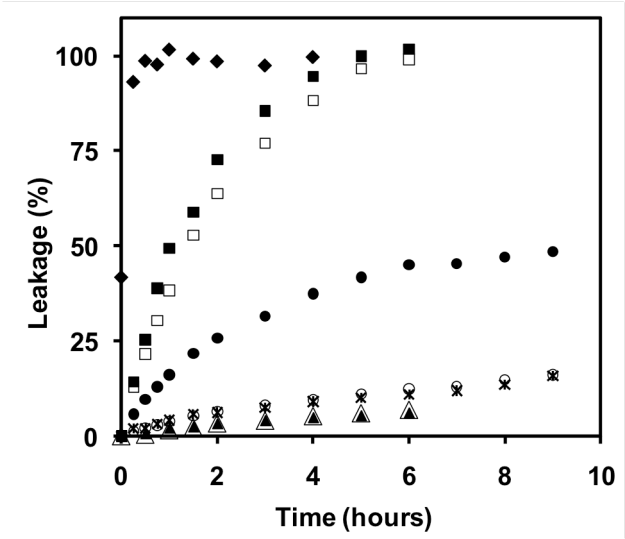

Figure 25. Time dependency study of carboxyfluorescein (CF) dye leakage from large unilamellar liposomes (LUV) ([lipid] = 7.83 μM) induced by 10 nm gold nanoparticles (Au NP) or melittin (MLT) at pH = 7.4 (20 mM HEPES), indicating the leakage in experimental samples containing MLT at MLT to lipid mass ratio (MLT/L) at 0.005 (♦), or positively charged gold nanoparticles (Au(+) NPs) at nanoparticle to lipid mass ratio (NP/L) at 0.02 (■), 0.015 (□), 0.005 (●), or 0.002 (○), or negatively charged gold nanoparticles (Au(-) NPs) at NP/L = 0.02 (▲), or PVP coated Au NPs (PVP Au NPs) at NP/L = 0.02 (Δ) as well as control sample

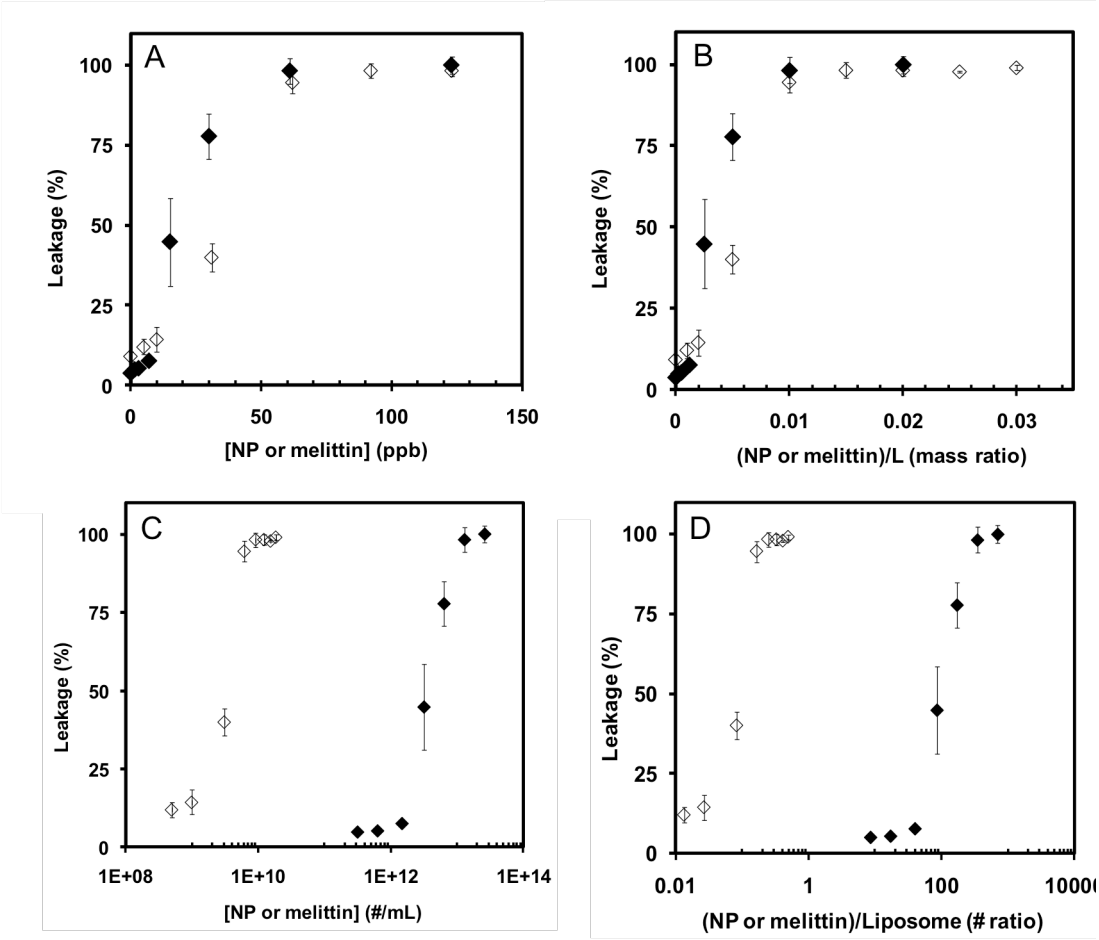

Figure 26. Comparison of liposome leakage induced by 10 nm positively charged Au nanoparticles (Au NP (+)) (◊), versus melittin (♦) as a function of (A) mass concentration, (B) mass ratio, (C) number concentrations, or (D) particle number ratio of Au NP(+) or melittin to liposome after reaching a steady state leakage at pH = 7.4 (20 mM HEPES). The error bars indicate ± one standard deviation.

results show a 40% steady state leakage induced by 10 nm Au(+) NP (30 ppb) after 90 min. The difference in kinetics to reach a steady state leakage can be attributed to the smaller particle size they used (i.e., 2 nm) resulting in higher diffusivity for Au(+) NPs compared to our 16 nm Au(+) NPs.

Concentration Dependency To further elucidate the relationship between liposome leakage versus Au NP concentration, we examined the concentration dependency over a wide range of Au concentration (i.e., 5 to 185 ppb) on membrane permeability, and compared it with the behavior of melittin. The results are reported in Figure 26. The data reported in Figure 26 are values recorded after apparent equilibrium (i.e., maximum leakage) has reached and therefore has no kinetic considerations. Figure 26A shows leakage induced by Au(+) NP and melittin as a function of Au NP or melittin mass concentration. Both Au(+) NP and melittin induce increased leakage as the added melittin or Au mass concentration increases. Since the liposome leakage percentage not only depends on the Au NP (or melittin) concentration, but also should relate to the lipid concentration, we also report the leakage percentage as a function of melittin or Au to lipid mass ratio as shown in Figure 26B. In Figure 26B, the quantity of released dye increased in a monotonic manner with the increased mass ratio of Au(+) NPs to lipid until the ratio reached 0.015. Beyond the point, ~100% of leakage has been achieved and

adding additional Au(+) NPs did not lead to more leakage. By lowering the Au concentration, leakage decreased noticeably, reducing to 40% of leakage at ratio of 0.005. The membrane permeabilizing behavior of Au(+) NPs resembles that of melittin as the leakage mediated by melittin also increased monotonically with increased melittin concentration. Melittin induced complete liposome leakage at a mass ratio ≥ 0.01, which is similar to Au(+) NPs. However, melittin is more effective in inducing leakage at a lower mass ratio, especially in the range of 0.0025 to 0.005. For example, at mass ratio of 0.005, melittin causes ~75% leakage, which is larger than that by Au(+) NPs at 40%. We estimated the mass ratio leading to 50% of liposome leakage (defined as leakage dose 50% (LD50)) for melittin and Au(+) NP at 17.8 and 32.4, respectively. We estimated the LD50 using the trimmed Spearman-Karber model.[103] Our melittin concentration dependency curve reported here correlates with a previous study[97] in which similar PC lipid vesicles were used. Goodman et al. also showed that leakage of negatively charged SOPC/SOPS vesicles increased with increasing mass concentration of 2 nm Au(+) NPs, although they never observed a complete liposome leakage at steady state.[102] In their study, the Au concentration ranged from 0.4 to 172 ppb (overlapping with ours of 5-185 ppb), which corresponds to 12 to 50% of leakage. Potential reasons for this discrepancy can be related to the liposome structure. It is known that liposomes with a size larger than 200 nm have a multilamellar structure, which is more resistant against permeabilization than unilamellar ones[99] This is consistent with the less leakage of 1 μm liposomes reported in the Goodman study compared to ours presented here. Alternatively, the nanoparticle size can play a role, as it has been shown that positively charged polymeric nanoparticles with a larger size tend to create more nanopore defects on lipid bilayers supported on silica surfaces.[85] It is also likely that Au(+) NPs mass concentration in the Goodman study was not enough to induce 100% leakage for a given amount of liposomes, although the lipid concentration was not clearly reported. The uncertainties highlight the need for additional research on the effects of liposome composition and structure and nanoparticle size on liposome leakage.

When we compare the concentration dependent effect on leakage based on number density of Au(+) NP versus melittin, the trend reversed as shown in Figure 26C. We convert Au mass concentration to number density of 10 nm Au NPs per milliliter using the following equations.

$$\#Au\ NP\ per\ mL = \frac{C_{Au} \times N_A / 1000}{\#Au\ atoms\ per\ NP} \quad (1)$$

$$\#Au\ atoms\ per\ NP = 4 \times \frac{Vol\ per\ NP}{4.0786^3} \quad (2)$$

Where C_{Au} is the molar concentration of Au NPs and N_A is the Avogadro number. There are 4 gold atoms per unit cubic cell with a length of 4.0786 Å.[51] We estimated the number of melittin macromolecules per milliliter by multiplying melittin molar concentration by the Avogadro number. In Figure 26C, Au(+) NPs is more effective in inducing liposome leakage than melittin at the same number density. For example, it requires 1×10^{13} melittin macromolecules per milliliter to cause 98% leakage, three orders of magnitude higher than Au(+) NPs by particle number (i.e., 1×10^{10}).

To estimate the least number of melittins or Au(+) NPs per liposome required to induce complete leakage, we divided the number of melittin or Au(+) NPs in the samples reported in Figure 26C by the number of liposomes present in the same samples. We estimated the number of liposomes per milliliter by two methods, using either lipid head group surface area or molecular volume of DOPC lipids. The two methods yield a similar number density of liposomes at 3.7×10^{10} liposomes/mL. In the first approach, we estimated the liposome number density by using the hydrated volume of a single lipid molecule (i.e., 2.0×10^7 Å^3).[104] DOPC lipid bilayer

has a thickness of ~3.2 nm[105] and thus the shell volume of a liposome with a diameter of 106 nm (measured by DLS) will be 1.0×10^{-13} nL. Dividing the shell volume by the volume of a DOPC molecule yields 8.6×10^4 DOPC molecules per liposome. Then, we estimate the number density of liposomes by dividing the total number of lipid molecules per milliliter (from the DOPC concentration = 7.82 μM) by the number of lipid molecules per liposome. The calculation gives the liposome number density of 5.4×10^{10} liposomes/mL. To confirm our calculations, in another approach we used the surface area of DOPC lipid head-group to determine number of liposomes. We multiplied the head group area of a DOPC lipid molecule (i.e., 59.4 $Å^2$)[106] by the concentration of DOPC (i.e., molecules per milliliter), which gave the total head group surface area of lipids. Considering only one fourth of the total lipid head group surface area will constitute the surface area facing the bulk solution in the bilayer arrangement, we then multiplied the derived value by a factor of 0.25 to give the total surface area of liposomes. We estimated the number density of liposomes by dividing the total surface area of liposomes by the surface area of a single liposome. The second method gives 1.9×10^{10} liposomes/mL, which is reasonably close to the result from the first method. We used the average (i.e., 3.7×10^{10}) of the liposome number densities derived from the two methods for our estimation of number density ratio of melittin or Au NP to liposome. In Figure 26D, on average ~350 melittin molecules per vesicle are needed to induce complete leakage. The result is smaller than the value (i.e., 250) reported by Benachir et.al.[97] They estimated the value with a statistical model for their system consisting of melittin and 100 nm POPC vesicles. It has been shown that DOPC liposomes are more resistant against leakage induced by melittin than POPC liposomes,[98] which correlates with higher number density ratio we obtained for DOPC liposomes compared to POPC ones. On the other hand, for Au(+) NPs to induce complete leakage of liposomes, our calculation indicates ~0.5 Au(+) NP per vesicle is required. Since the ratio is derived from our estimation assuming uniform size distributions of Au(+) NPs and liposomes, we do not consider this value significantly different the order of 1.The mechanism for the Au(+) NPs-mediated liposome leakage is currently unclear. It is well known that melittin creates pores on lipid bilayers, thereby releasing the encapsulated dye.[97,98] Recently, it has been shown that positively charged Au NP can create holes on lipid bilayers supported on silica surfaces.[107] For the data presented here, it is likely that Au(+) NPs creates pores on liposomes, leading to the release of encapsulated dye. The discrepancy in the capability of inducing liposome leakage for melittin versus Au(+) NPs in terms of number density may be attributed to the size effect. Considering that Au(+) NP is 16 nm in hydrodynamic diameter larger than that of melittin (~2.5 nm as measured by DLS), it may be that Au NP(+) can create larger defects on vesicles than melittin, thereby resulting in more leakage by number density. Prior studies have indicated that polymeric nanoparticles with a larger size tend to create larger defects on supported lipid bilayer.[85]

Alternatively, Au(+) NP may induce the aggregation of liposomes. This has been shown to occur for liposomes interacting with nanoparticles of opposite charge.[108] Given a larger size and higher zeta potential than melittin (i.e., 20.0 versus 13.0 mV), it is likely that vesicles can hetero-aggregate with gold particles, leading to liposome leakage. To test this hypothesis, we measured the hydrodynamic size change of liposomes before and after adding melittin or Au(+) NPs at the NP/L mass ratio of 0.01, at which ratio 100% leakage occurs as shown in Figure 2B. The result (not shown) indicates that melittin caused the liposome size to increase by 50%, while liposome size in the control sample without melittin remained unchanged. Our observations correlate with the work by Wessman et al.,[101] where the melittin-induced DOPC liposome aggregation was revealed by cryo-TEM micrographs, while liposomes without melittin remained intact. In contrast, we only observed minimal increase in liposome size in the presence of Au(+) NPs after 6 h. In a recent study, Chen et al. examined the interaction of liposomes with iron oxide nanoparticles of opposite charge.[108] They observed that the liposome size almost doubled after adding 16 nm nanoparticles at the nanoparticles to liposome surface

area ratio of 0.23. In our study, the surface ratio was relatively low at 0.003 (corresponding to mass ratio of 0.01), two orders of magnitude lower than what Chen et al. used. Our observation of complete leakage of liposomes suggests that liposome aggregation may not be responsible for liposome leakage at our range of nanoparticle to liposome surface ratio. The mechanistic study is ongoing work in our lab.

Figure 27 compares the effects of surface coating and charge characteristics on liposome leakage by TiO2 NP or Au NPs. In these experiments, we mixed nanoparticle and liposome to the same mass concentrations ratio of 0.01 (i.e., 60 ppb of nanoparticle and 6 ppm of lipid) and the leakage data were all values recorded upon reaching a steady state (i.e., 6 h). The liposome leakage is a strong function of surface charge characteristics. For example, Au(+) NPs induced 94% of leakage while only minimal leakage was detected for Au(-) NPs as well as PVP Au NP (also negatively charged). Considering DOPC liposomes are negatively charged as measured, the strong surface charge effect may be attributable to electrostatic attraction between Au NP and liposomes. To further examine the effect of surface charge, we used a different core composition nanoparticles (i.e., TiO_2) with similar cationic and anionic surface coverage and diameter as Au NPs. DLS measurements indicate the hydrodynamic sizes of TiO_2(+) NP and TiO_2(-) NP were 10.9 ± 0.3 nm and 7.7 ± 0.5 nm, respectively. The zeta potentials for TiO_2(+) NP and TiO_2(-) NP were 31.2 ± 1.3 mV and -45.8 ± 0.6 mV, respectively at pH = 7.4. The result indicates that the charge effect on liposome leakage correlates with that of Au NPs. A prior study showed that carbon nanotubes (CNTs) coated with positively charged proteins caused the leakage of negatively charged liposomes, while uncoated CNTs had a minimal effect.[109] Their results also showed minimal leakage induced by negatively charged NPs in a good agreement with our observations. Taken together, the finding suggests that surface coating, which determines the surface charge sign, plays a key role in the interaction of metallic and metal oxide nanoparticles with DOPC lipid bilayer vesicles, and changing the core composition have an insignificant effect.

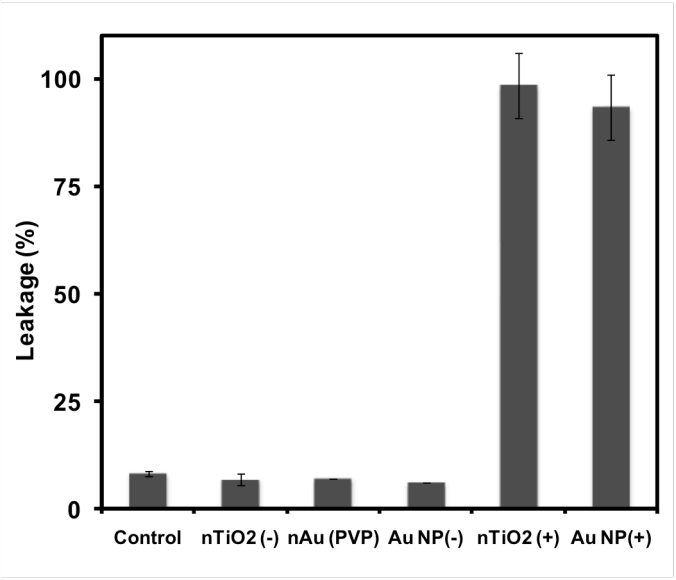

Figure 27. Comparison of liposome leakage induced by 10 nm nanoparticles with different surface coating, charge characteristics, and core compositions, indicating the percent leakage induced by negatively charged TiO_2 nanoparticles (TiO_2(-) NP), positively charged TiO_2 nanoparticles (TiO_2(+) NP), negatively charged Au nanoparticles (Au(-) NP), positively charged Au nanoparticles (Au(+) NP), as well as polyvinylpyrrolidone coated Au nanoparticles (PVP Au NPs) at pH = 7.4 (20 mM HEPES). The error bars indicate ± one standard deviation.

Lastly, we examine the effect of the presence of nanostructure on liposome leakage. To do this, we compare the leakage induced by Au(+) NPs filtrate (potentially containing free DADMAC), the coating material (i.e., DADMAC) solution, or Au(+) NPs. The filtrate was obtained by passing the Au(+) NPs stock solution through a 3kDa ultrafiltration filter. We diluted the filtrate to the concentration level as we used for Au NP(+) in our experiments. Figure 28 compares the leakage induced by Au(+) NPs at 60 ppb, DADMAC solution at 700 ppb (equivalent to that present on Au NP(+) surface, estimated based on the mass ratio (gold to DADMAC) of 1 to 11.5 reported by the supplier), filtrate, and the control solution (i.e., buffer electrolyte). Comparing with the leakage by Au(+) NPs, we observed an insignificant leakage by

DADMAC or the filtrate, which is similar to the control experiment. The finding indicates that the coating material has to associate with nanoparticles (i.e., the nanostructure) to cause lipid bilayer leakage. In other words, the coating materials are not capable of inducing liposome disruption on their own. The result aligns with previous work that indicates that a cationic protein (i.e., lysozyme) will not exert permeabilizing effect on liposome unless it is associated with a tubular nanostructure (i.e., CNTs).[109] This work will result in one journal publication:

Moghadam, B.; Hou, W.-C.; Corredor, C.; Westerhoff, P.; Posner, J. D. Engineered Nanoparticles Induce Model Cell Membrane Leakage: Implications for Nanotoxicity. In preparation.

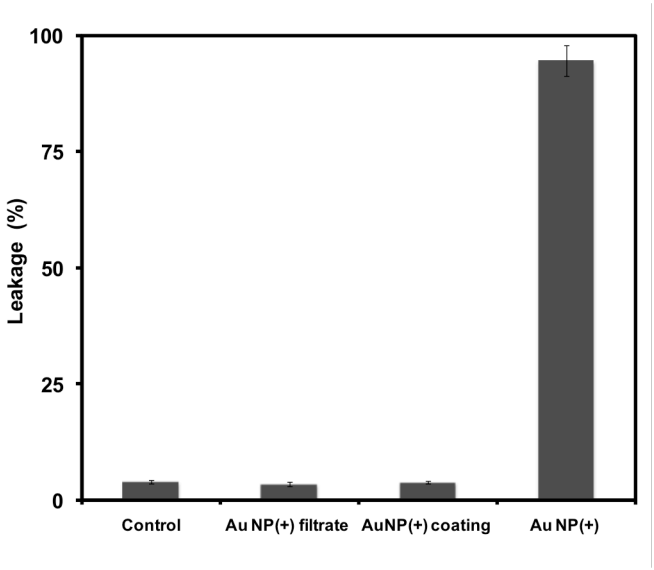

Figure 28. Comparison of dye leakage from liposomes ([lipid] = 7.83 μM) induced by the positively charged Au nanoparticles (Au(+) NPs) (60 μg/L), poly (diallyldimethylammonium chloride) (DADMAC), the cationic material used to coat Au(+) NPs surface (700 μg/L), or the filtrate of Au(+) NPs after 6 h of incubation at pH = 7.4 (20 mM HEPES). The control sample contained liposomes only. The error bars indicate ± one standard deviation.

Summary

In this project, we have investigated two major hypotheses: (1) ENP partitioning between water and organic phases (octanol or lipid bilayer) is highly dependent on their physiochemical properties, aggregation, and the water chemistry parameters in aquatic environments (salts, natural organic matter, pH), which may impact their partitioning into biological matrices (bioaccumulation) and human exposure (bioavailability). (2) The interaction with ENPs will cause the disruption of lipid bilayer, which is dependent on the physicochemical properties of ENPs.

In the first hypothesis, we examine the partitioning of ENPs into octanol, lipid bilayer, and water. We have found that the partitioning of ENP reaches pseudo-equilibrium distributions between water and organic phases. The equilibrium partitioning most strongly depends on the particle surface charge, which leads us to the conclusion that electrostatic interactions are critical to understanding the fate of ENP in the environment. We also show that the kinetic rate at which particle partition is a function of their size (small particles partition faster by number) as can be predicted from simple DLVO models. We have found that particle number density is the mechanistic dosimetry to present our results and provide quantitative comparison across experiments and experimental platforms. Cumulatively, our work shows that lipid bilayers are a more effective organic phase than octanol because of the definable surface area and ease of interpretation of the results. Our early comparison of ENP partitioning between water and lipid bilayer suggests that this measurement can be predictive of bioaccumulation in aquatic organisms.

In our second hypothesis, we examine the disruption of lipid bilayers by ENPs. We show that nanoparticles disrupt lipid bilayer membranes and detail how NP-bilayer interaction leads to the malfunction of lipid bilayers in regulating the fluxes of ionic charges and molecules. Our results show that the disruption of the lipid membranes is similar to that of toxin melittin, except single particles can disrupt a bilayer. We show that approximately a single particle is required to disrupt a 100 nm DOPC liposome. The equilibrium leakage of membranes is a function of the particle number density and particle surface charge, consistent with results from our partitioning experiments. Our disruption experiments with varying surface functionality of ENPs show that positively charged particles (poly amine) are most disruptive, in large contrast to ENPs with negatively charged functionality which exhibit minimal disruption. Lipid bilayer disruption is independent of nanoparticle core composition, consistent with in in vitro toxicity panels using cell cultures. We attribute the disruption capability of nanoparticles to the strong electrostatic attraction between the nanoparticles with cationic surface functionality and net negatively charged lipid bilayer surface. We show that nanoparticles with different shapes (tubular versus spherical) exhibit distinct membrane disrupting behaviors. The disruption by spherical ENPs is similar to that by melittin, which creates nanoscale pores on lipid membranes. Tubular carbon nanotubes create incremental current steps across lipid membrane over time, which simulate the ionic charge transport behavior of carbon nanotube. This suggests that carbon nanotube ion channels likely form across the lipid bilayers, through which ionic charges transport under an applied voltage.

List of Contributions

General:

Posner, J. D. Engineered nanomaterials: Where they go, nobody knows. *Nano Today* **2009**, *4*, 114-115.

Partitioning of engineering nanomaterials:

Marine, N. A.; Klein, S. A.; Posner. J. D. Partition Coefficient Measurements in Picoliter Drops Using a Segmented Flow Microfluidic Device. *Anal. Chem.* **2009**, *81*, 1471-1476.

Hristovski, K.; Westerhoff, P.; Posner, J. D. Octanol-Water Partitioning of Engineered Nanomaterials. *J. Environ. Sci. Heal. A* **2011**, *46*, 636-647.

Hou, W.-C.; Moghadam, B.; Westerhoff, P.; Posner, J. D. Distribution of Fullerene Nanomaterials between Water and Model Biological Membranes. *Langmuir*, accepted in press.

Hou, W.-C.; Moghadam, B.; Corredor, C.; Westerhoff, P.; Posner, J. D. Distribution of Functionalized Gold Nanoparticles between Water and Model Biological Membrane. In preparation.

Engineering nanomaterial disruption of model cell membranes:

Klein, S. A.; Wilk, S. J.; Thornton, T. J.; Posner J. D. Formation of nanopores in suspended lipid bilayers using quantum dots. In: Journal of Physics: Conference Series. Vol 109. Institute of Physics Publishing; 2008:012022.

Corredor, C.; Hou, W.-C.; Klein, S. A.; Moghadam, B.; Goryll, M.; Westerhoff, P.; Posner, J. D. Electrophysiological Measurements to Detect Suspended Lipid Bilayer Disruption Induced by Nanoparticles. In preparation.

Moghadam, B.; Hou, W.-C.; Corredor, C.; Westerhoff, P.; Posner, J. D. Engineered Nanoparticles Induce Model Cell Membrane Leakage: Implications for Nanotoxicity. In preparation.

Presentations

Hristovski, K.; Westerhoff, P.; Posner. J. D. Partitioning of nanoparticles in octanol and water. American Chemical Society Spring Meeting. March 22–26, 2009.

Posner, J. D.; Westerhoff, P.; Hristovski, K.; Klein, S. K. Partitioning of Nanoparticles into Organic Phases and Model Cells. Interagency Nanotechnology Implications Grantees Workshop — EPA, NSF, NIH/NIEHS, NIOSH and DOE. Nov. 9–10, 2009.

Hristovski, K.; Mousset, E.; Luque, H.; Westerhoff, P.; Posner. J. D. Sorption of Engineered Nanomaterials to Soils. American Chemical Society Fall Meeting, Fall National Meeting & Exposition, Boston, MA, August 22-26, 2010.

Hou, W.-C.; Hristovski, K.; Westerhoff, P.; Posner, J. D. Affinity of Engineered Nanoparticles to Artificial Cell Membranes. Oral presentation at the AICHE Annual Meeting, Salt Lake City UT, Nov. 7-12, 2010.

Posner, J. D.; Hou, W. C.; Westerhoff, P. Interactions of Nanomaterials with Model Cell Membranes, U.S. EPA Nanotechnology Grantees Meeting, Portland, OR. Nov. 9, 2010.

Corredor, C.; Hou, W.-C.; Moghadam, B.; Klein, S.; Goryll, M,; Westerhoff, P.; Posner, J. D. Prediction of Nanoparticle Toxicity using Electrophysiological Measurement of Artificial Cell Membrane Disruption, Poster presentation at the SRC-Sematech ERC Review Meeting Tucson, AZ, 2011.

Hou, W.-C.; Moghadam, B.; Corredor, C.; Westerhoff, P.; Posner, J. D. Distribution of engineered nanomaterials between model biological membranes and water. Poster presentation at the SRC-Sematech ERC Review Meeting Tucson, AZ, 2011.

Moghadam, B. Hou, W.-C.; Westerhoff, P.; Posner, J. D. Interactions of Engineered Nanomaterials and Model Biomembranes. Poster presentation at the SRC-Sematech ERC Review Meeting Tucson, AZ, 2011.

Hou, W.-C.; Moghadam, B.; Westerhoff, P.; Posner, J. D. Distribution of engineered nanomaterials between model biological membranes and water. Oral presentation at the 241st American Chemical Society National Meeting, Anaheim, CA, March 27-31, 2011.

Hou, W.-C.; Moghadam, B.; Corredor, C.; Westerhoff, P.; Posner, J. D. Distribution of Engineered Nanomaterials between Model Biological Membranes and Water. Poster presentation at the first Gordon Research Conference on Environmental Nanotechnology, Waterville, NH, May 29-June 3, 2011.

Moghadam, B. Hou, W.-C.; Westerhoff, P.; Posner, J. D. Interactions of Engineered Nanomaterials and Model Biomembranes. Poster presentation at the first Gordon Research Conference on Environmental Nanotechnology, Waterville, NH, May 29-June 3, 2011.

Corredor, C.; Klein, S A.; Moghadam, B.; Hou, W.-C.; Westerhoff, P.; Posner, J. D. Disruption of Suspended Lipid Bilayer Induced by Engineered Nanomaterials. Gordon Research Conference on Environmental Nanotechnology, Waterville, NH, May 29-June 3, 2011.

Reference

(1) An inventory of nanotechnology-based consumer products currently on the market of the Project of Emerging Nanotechnology.
(2) Klaine, S. J. Alvarez, P. J. J. Batley, G. E. Fernandes, T. F. Handy, R. D. Lyon, D. Y. Mahendra, S. McLaughlin, M. J.; Lead, J. R. *Environ. Toxicol. Chem.* **2008**, *27*, 1825-1851.
(3) Davies, R. P.; Dobbs, A. J. *Water Research* **1984**, *18*, 1253–1262.
(4) Jafvert, C. T. Westall, J. C. Grieder, E.; Schwarzenbach, R. P. *Environ. Sci. Technol.* **1990**, *24*, 1795–1803.
(5) Neely, W. B. Branson, D. R.; Blau, G. E. *Environ. Sci. Technol.* **1974**, *8*, 1113-1115.
(6) Chiou, C. T. Schmedding, D. W.; Manes, M. *Environ. Sci. Technol.* **1982**, *16*, 4-10.
(7) Chiou, C. T. Freed, V. H. Schmedding, D. W.; Kohnert, R. L. *Environ. Sci. Technol.* **1977**, *11*, 475-478.
(8) Penners, N. H. G.; Koopal, L. K. *Colloid Surf.* **1986**, *19*, 337-349.
(9) US EPA Product properties test guideline. OPPTS 830.7550 Partition coefficient (n-octanol/H2O), shake flask method. EPA 712-C-95-038. Washington DC USA **1995**.
(10) Leenheer, J. A. Wershaw, R. L.; Reddy, M. M. *Environ. Sci. Technol.* **1995**, *29*, 393-398.
(11) Zhang, Y. Chen, Y. Westerhoff, P. Hristovski, K.; Crittenden, J. C. *Water Res.* **2008**, *42*, 2204–2212.
(12) Jafvert, C. T.; Kulkarni, P. P. *Environ. Sci. Technol.* **2008**, *42*, 5945-5950.
(13) Binks, B. P.; Rodrigues, J. A. *Angew. Chem. Int. Ed.* **2005**, *44*, 441-444.
(14) Fortner, J. D. Lyon, D. Y. Sayes, C. M. Boyd, A. M. Falkner, J. C. Hotze, E. M. Alemany, L. B. Tao, Y. J. Guo, W. Ausman, K. D. Colvin, V. L.; Hughes, J. B. *Environ. Sci. Technol.* **2005**, *39*, 4307-4316.
(15) Brant, J. A. Labille, J. Robichaud, C. O.; Wiesner, M. *J. Colloid Interface Sci.* **2007**, *314*, 281–288.
(16) Navarro, D. A. G. Watson, D. F. Aga, D. S.; Banerjee, S. *Environ. Sci. Technol.* **2009**, *43*, 677-682.
(17) Böker, A. He, J. Emrick, T.; Russell, T. P. *Soft Matter* **2007**, *3*, 1231.
(18) Petosa, A. R. Jaisi, D. P. Quevedo, I. R. Elimelech, M.; Tufenkji, N. *Environ. Sci. Technol.* **2010**, *44*, 6532-6549.
(19) Ngai, T. Auweter, H.; Behrens, S. H. *Macromolecules* **2006**, *39*, 8171-8177.
(20) Carlsson, K.; Karlberg, B. *Anal. Chim. Acta* **2000**, *423*, 137-144.
(21) Sarrazin, F. Prat, L. Di Miceli, N. Cristobal, G. Link, D. R.; Weitz, D. A. *Chem. Eng. Sci.* **2007**, *62*, 1042-1048.
(22) Millman, J. R. Bhatt, K. H. Prevo, B. G.; Velev, O. D. *Nat. Mater.* **2005**, *4*, 98-102.
(23) Mary, P. Studer, V.; Tabeling, P. *Anal. Chem.* **2008**, *80*, 2680-2687.
(24) Barbier, V. Willaime, H. Tabeling, P.; Jousse, F. *Phys. Rev. E* **2006**, *74*, 046306.
(25) Lee, J. N. Park, C.; Whitesides, G. M. *Anal. Chem.* **2003**, *75*, 6544-6554.
(26) Toepke, M. W.; Beebe, D. J. *Lab Chip* **2006**, *6*, 1484.
(27) Beltran, J. Lopez, F. J. Cepria, O.; Hernandez, F. *J. Chromatogr. A* **1998**, *808*, 257-263.
(28) Garstecki, P. Fuerstman, M. J. Stone, H. A.; Whitesides, G. M. *Lab Chip* **2006**, *6*, 437.
(29) Günther, A. Jhunjhunwala, M. Thalmann, M. Schmidt, M. A.; Jensen, K. F. *Langmuir* **2005**, *21*, 1547-1555.
(30) Alberts, B. Johnson, A. Lewis, J. Raff, M. Roberts, K.; Walter, P. *Molecular Biology of the Cell, Fourth Edition*; 4th ed. Garland Science, 2002.

(31) Nel, A. E. Mädler, L. Velegol, D. Xia, T. Hoek, E. M. V. Somasundaran, P. Klaessig, F. Castranova, V.; Thompson, M. *Nat. Mater.* **2009**, *8*, 543-557.
(32) Dulfer, W. J.; Govers, H. A. J. *Environ. Sci. Technol.* **1995**, *29*, 2548-2554.
(33) Kwon, J. -H; Liljestrand, H. M.; Katz, L. E. *Environ. Toxicol. Chem.* **2006**, *25*, 1984-1992.
(34) Opperhuizen, A. Serne, P.; Van der Steen, J. M. D. *Environ. Sci. Technol.* **1988**, *22*, 286-292.
(35) Escher, B. I.; Schwarzenbach, R. P. *Environ. Sci. Technol.* **1996**, *30*, 260-270.
(36) Muuller, M. T. Zehnder, A. J. B.; Escher, B. I. *Environ. Toxicol. Chem.* **1999**, *18*, 2191-2198.
(37) Kwon, J.-H. Liljestrand, H. M.; Katz, L. E. *Environ. Sci. Technol.* **2007**, *41*, 4011-4018.
(38) Giri, J. Diallo, M. S. Goddard III, W. A. Dalleska, N. F. Fang, X.; Tang, Y. *Environ. Sci. Technol.* **2009**, *43*, 5123-5129.
(39) Hristovski, K. D. Westerhoff, P. K.; Posner, J. D. *J. Environ. Sci. Heal. A* **2011**, *46*, 636-647.
(40) Escher, B. I. Schwarzenbach, R. P.; Westall, J. C. *Environ. Sci. Technol.* **2000**, *34*, 3954-3961.
(41) Escher, B. I. Schwarzenbach, R. P.; Westall, J. C. *Environ. Sci. Technol.* **2000**, *34*, 3962-3968.
(42) Loidl-Stahlhofen, A. Schmitt, J. Nöller, J. Hartmann, T. Brodowsky, H. Schmitt, W.; Keldenich, J. *Adv. Mater.* **2001**, *13*, 1829-1834.
(43) Loidl-Stahlhofen, A. Hartmann, T. Schöttner, M. Röhring, C. Brodowsky, H. Schmitt, J.; Keldenich, J. *Pharm. Res.* **2001**, *18*, 1782–1788.
(44) Klaine, S. J. Alvarez, P. J. J. Batley, G. E. Fernandes, T. F. Handy, R. D. Lyon, D. Y. Mahendra, S. McLaughlin, M. J.; Lead, J. R. *Environ. Toxicol. Chem* **2008**, *27*, 1825-1851.
(45) Lee, J. Cho, M. Fortner, J. D. Hughes, J. B.; Kim, J.-H. *Environ. Sci. Technol.* **2009**, *43*, 4878-4883.
(46) Hou, W.-C. Kong, L. Wepasnick, K. A. Zepp, R. G. Fairbrother, D. H.; Jafvert, C. T. *Environ. Sci. Technol.* **2010**, *44*, 8121-8127.
(47) Fortner, J. D. Kim, D.-I. Boyd, A. M. Falkner, J. C. Moran, S. Colvin, V. L. Hughes, J. B.; Kim, J.-H. *Environ. Sci. Technol.* **2007**, *41*, 7497-7502.
(48) Hope, M. J. Bally, M. B. Webb, G.; Cullis, P. R. *Biochim. Biophys. Acta-Biomembr.* **1985**, *812*, 55–65.
(49) Petitou, M. Tuy, F.; Rosenfeld, C. *Anal. Biochem.* **1978**, *91*, 350–353.
(50) Hou, W.-C.; Jafvert, C. T. *Environ. Sci. Technol.* **2009**, *43*, 5257-5262.
(51) Chithrani, B. D. Ghazani, A. A.; Chan, W. C. W. *Nano Lett.* **2006**, *6*, 662-668.
(52) Kučerka, N. Kiselev, M. A.; Balgavý, P. *Eur Biophys J* **2003**, *33*, 328-334.
(53) Liu, X.-Y. Yang, Q. Kamo, N.; Miyake, J. *J. Chromatogr. A* **2001**, *913*, 123-131.
(54) Brant, J. A. Labille, J. Robichaud, C. O.; Wiesner, M. *J. Colloid Interf. Sci.* **2007**, *314*, 281-288.
(55) Chao, T.-C. Song, G. Hansmeier, N. Westerhoff, P. Herckes, P.; Halden, R. U. *Anal. Chem.* **2011**, *83*, 1777-1783.
(56) Zhou, Y.; Raphael, R. M. *Biophys. J.* **2007**, *92*, 2451-2462.
(57) Weber, W. J.; DiGiano, F. A. *Process Dynamics in Environmental Systems*; Wiley-Interscience, 1996.
(58) Wong-Ekkabut, J. Baoukina, S. Triampo, W. Tang, I.-M. Tieleman, D. P.; Monticelli, L. *Nat. Nanotechnol.* **2008**, *3*, 363-368.
(59) Qiao, R. Roberts, A. P. Mount, A. S. Klaine, S. J.; Ke, P. C. *Nano Lett.* **2007**, *7*, 614-619.
(60) Bedrov, D. Smith, G. D. Davande, H.; Li, L. *J. Phys. Chem. B* **2008**, *112*, 2078-2084.
(61) Schwarzenbach, R. P. Gschwend, P. M.; Imboden, D. M. *Environmental Organic Chemistry*; 2nd ed. Wiley-Interscience, 2002.
(62) Oberdörster, E. Zhu, S. Blickley, T. M. McClellan-Green, P.; Haasch, M. L. *Carbon* **2006**, *44*, 1112-1120.

(63) Tervonen, K. Waissi, G. Petersen, E. J. Akkanen, J.; Kukkonen, J. V. K. *Environ. Toxicol. Chem.* **2010**, 1072-1078.
(64) Tao, X. Fortner, J. D. Zhang, B. He, Y. Chen, Y.; Hughes, J. B. *Chemosphere* **2009**, *77*, 1482-1487.
(65) Kiser, M. A. Ryu, H. Jang, H. Hristovski, K.; Westerhoff, P. *Water Res.* **2010**, *44*, 4105-4114.
(66) van Wezel, A. P.; Opperhuizen, A. *Crit. Rev. Toxicol.* **1995**, *25*, 255-279.
(67) Sayes, C. M. Fortner, J. D. Guo, W. Lyon, D. Boyd, A. M. Ausman, K. D. Tao, Y. J. Sitharaman, B. Wilson, L. J. Hughes, J. B. West, J. L.; Colvin, V. L. *Nano Lett.* **2004**, *4*, 1881-1887.
(68) Usenko, C. Y. Harper, S. L.; Tanguay, R. L. *Carbon* **2007**, *45*, 1891–1898.
(69) Zhu, X. Zhu, L. Li, Y. Duan, Z. Chen, W.; Alvarez, P. J. J. *Environ. Toxicol. Chem.* **2007**, *26*, 976-979.
(70) Chen, K. L.; Elimelech, M. *Langmuir* **2006**, *22*, 10994-11001.
(71) Wilhelm, C. Gazeau, F. Roger, J. Pons, J. N.; Bacri, J.-C. *Langmuir* **2002**, *18*, 8148-8155.
(72) Zhang, W. Kalive, M. Capco, D. G.; Chen, Y. *Nanotechnology* **2010**, *21*, 355103.
(73) Cho, E. C. Xie, J. Wurm, P. A.; Xia, Y. *Nano Lett.* **2009**, *9*, 1080-1084.
(74) Elimelech, M. Jia, X. Gregory, J.; Williams, R. *Particle Deposition & Aggregation: Measurement, Modelling and Simulation*; 1st ed. Butterworth-Heinemann, 1998.
(75) Zhang, W. Rittmann, B.; Chen, Y. *Environ. Sci. Technol.* **2011**, *45*, 2172-2178.
(76) Farkas, J. Christian, P. Gallego-Urrea, J. A. Roos, N. Hassellöv, M. Tollefsen, K. E.; Thomas, K. V. *Aquat. Toxicol.* **2011**, *101*, 117-125.
(77) Demarche, S. Sugihara, K. Zambelli, T. Tiefenauer, L.; Vörös, J. *Analyst* **2011**, *136*, 1077-1089.
(78) Chen, J. Hessler, J. A. Putchakayala, K. Panama, B. K. Khan, D. P. Hong, S. Mullen, D. G. DiMaggio, S. C. Som, A. Tew, G. N. Lopatin, A. N. Baker, J. R. Holl, M. M. B.; Orr, B. G. *J. Phys. Chem. B* **2009**, *113*, 11179-11185.
(79) Pornpattananangkul, D. Olson, S. Aryal, S. Sartor, M. Huang, C. M. Vecchio, K.; Zhang, L. *ACS nano* **2010**, *4*, 1935–1942.
(80) Klein, S. A. Wilk, S. J. Thornton, T. J.; Posner, J. D. In *J. Phys.: Conf. Ser.* 2008; Vol. 109, p. 012022.
(81) Tosteson, M. T.; Tosteson, D. C. *Biophysical Journal* **1981**, *36*, 109-116.
(82) Montal, M.; Mueller, P. *Proc. Natl. Acad. Sci. U. S. A.* **1972**, *69*, 3561 -3566.
(83) Wang, X. Xia, T. Ntim, S. A. Ji, Z. George, S. Meng, H. Zhang, H. Castranova, V. Mitra, S.; Nel, A. E. *ACS Nano* **2010**, *4*, 7241-7252.
(84) Ramachandran, S. Kumar, G. L. Blick, R. H.; van der Weide, D. W. *Appl. Phys. Lett.* **2005**, *86*, 083901.
(85) Mecke, A. Majoros, I. J. Patri, A. K. Baker, J. R. Holl, M. M. B.; Orr, B. G. *Langmuir* **2005**, *21*, 10348-10354.
(86) Kostarelos, K. Lacerda, L. Pastorin, G. Wu, W. WieckowskiSebastien, S. Luangsivilay, J. Godefroy, S. Pantarotto, D. Briand, J.-P. Muller, S. Prato, M.; Bianco, A. *Nat. Nanotechnol.* **2007**, *2*, 108-113.
(87) Porter, A. E. Gass, M. Muller, K. Skepper, J. N. Midgley, P. A.; Welland, M. *Nat. Nanotechnol.* **2007**, *2*, 713-717.
(88) Lopez, C. F. Nielsen, S. O. Moore, P. B.; Klein, M. L. *Proc. Natl. Acad. Sci. U. S. A.* **2004**, *101*, 4431 -4434.
(89) Frank, S. Poncharal, P. Wang, Z. L.; Heer, W. A. de *Science* **1998**, *280*, 1744 -1746.
(90) Hilder, T. A. Gordon, D.; Chung, S.-H. *Biophys. J.* **2010**, *99*, 1734-1742.
(91) Joseph, S. Mashl, R. J. Jakobsson, E.; Aluru, N. R. *Nano Letters* **2003**, *3*, 1399-1403.

(92) Choi, W. Lee, C. Y. Ham, M.-H. Shimizu, S.; Strano, M. S. *J. Am. Chem. Soc.* **2011**, *133*, 203-205.
(93) Lee, C. Y. Choi, W. Han, J.-H.; Strano, M. S. *Science* **2010**, *329*, 1320 -1324.
(94) Hamill, O. P. Marty, A. Neher, E. Sakmann, B.; Sigworth, F. J. *Pflugers Arch. Eur. J. Physiol.* **1981**, *391*, 85-100.
(95) Pawlak, M. Stankowski, S.; Schwarz, G. *Biochim.Biophys. Acta-Biomembr.* **1991**, *1062*, 94-102.
(96) Gervais, C. Dô, F. Cantin, A. Kukolj, G. White, P. W. Gauthier, A.; Vaillancourt, F. H. *J. Biomol. Screen* **2011**, *16*, 363 -369.
(97) Benachir, T.; Lafleur, M. *Biochim. Biophys. Acta-Biomembr.* **1995**, *1235*, 452-460.
(98) Rex, S. *Biophys. Chem.* **1996**, *58*, 75-85.
(99) Sila, M. Au, S.; Weiner, N. *Biochim. Biophys. Acta-Biomembr.* **1986**, *859*, 165-170.
(100) Matsuzaki, K. Yoneyama, S.; Miyajima, K. *Biophys. J.* **1997**, *73*, 831-838.
(101) Wessman, P. Strömstedt, A. A. Malmsten, M.; Edwards, K. *Biophys. J.* **2008**, *95*, 4324-4336.
(102) Goodman, C. M. McCusker, C. D. Yilmaz, T.; Rotello, V. M. *Bioconjugate Chem.* **2004**, *15*, 897-900.
(103) Hamilton, M. A. Russo, R. C.; Thurston, R. V. *Environ. Sci. Technol.* **1977**, *11*, 714-719.
(104) Greenwood, A. I. Tristram-Nagle, S.; Nagle, J. F. *Chem. Phys. Lipids* **2006**, *143*, 1-10.
(105) Wiener, M. C.; White, S. H. *Biophys. J.* **1992**, *61*, 428-433.
(106) Fattal, D. R.; Ben-Shaul, A. *Biophys. J.* **1994**, *67*, 983-995.
(107) Leroueil, P. R. Berry, S. A. Duthie, K. Han, G. Rotello, V. M. McNerny, D. Q. Baker,, J. R. Orr, B. G.; Holl, M. M. B. *Nano Lett.* **2008**, *8*, 420-424.
(108) Chen, Y.; Bothun, G. D. *Langmuir* **2011**, *27*, 8645-8652.
(109) Hirano, A. Uda, K. Maeda, Y. Akasaka, T.; Shiraki, K. *Langmuir* **2010**, *26*, 17256-17259.
(110) Lin, S.; Wiesner, M. R. *Langmuir* **2010**, *26*, 16638-16641.
(111) Lyklema, J. *Fundamentals of Interface and Colloid Science*; Academic Press, 1991.
(112) Israelachvili, J. N. *Langmuir* **1994**, *10*, 3369-3370.
(113) Israelachvili, J. N. *Intermolecular and Surface Forces, Second Edition: With Applications to Colloidal and Biological Systems*; 2nd ed. Academic Press, 1992.

Appendices

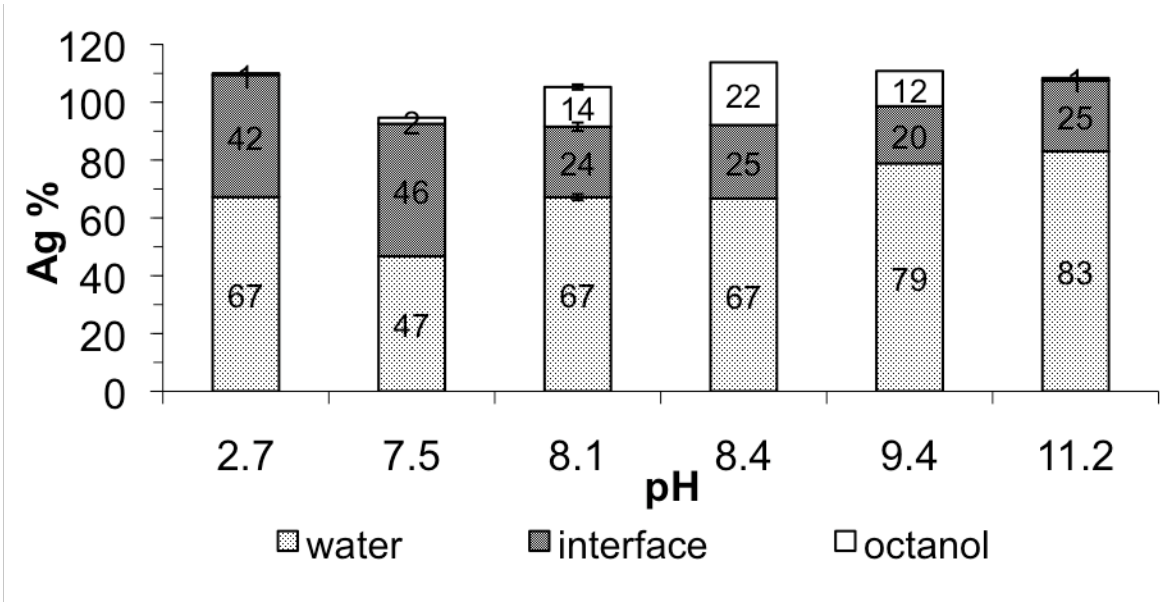

Figure S1. Distribution of functionalized silver nanoparticles at different pH values.

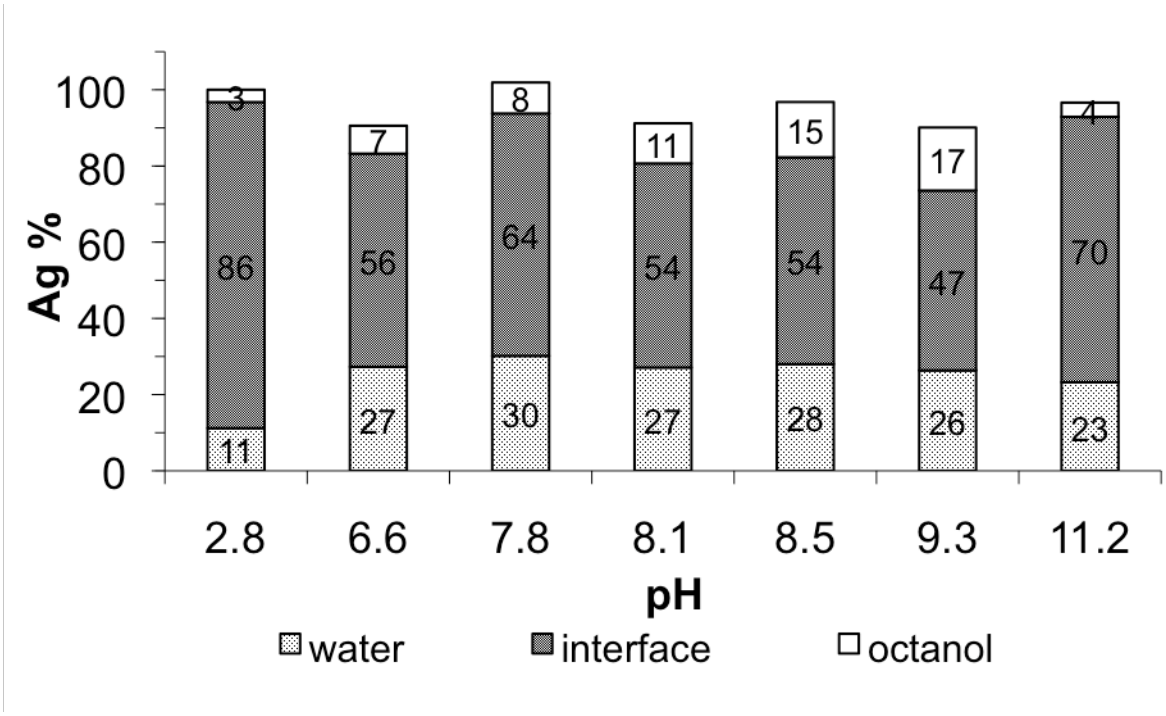

Fig. S2. Distribution of unfunctionalized silver nanoparticles at different pH values.

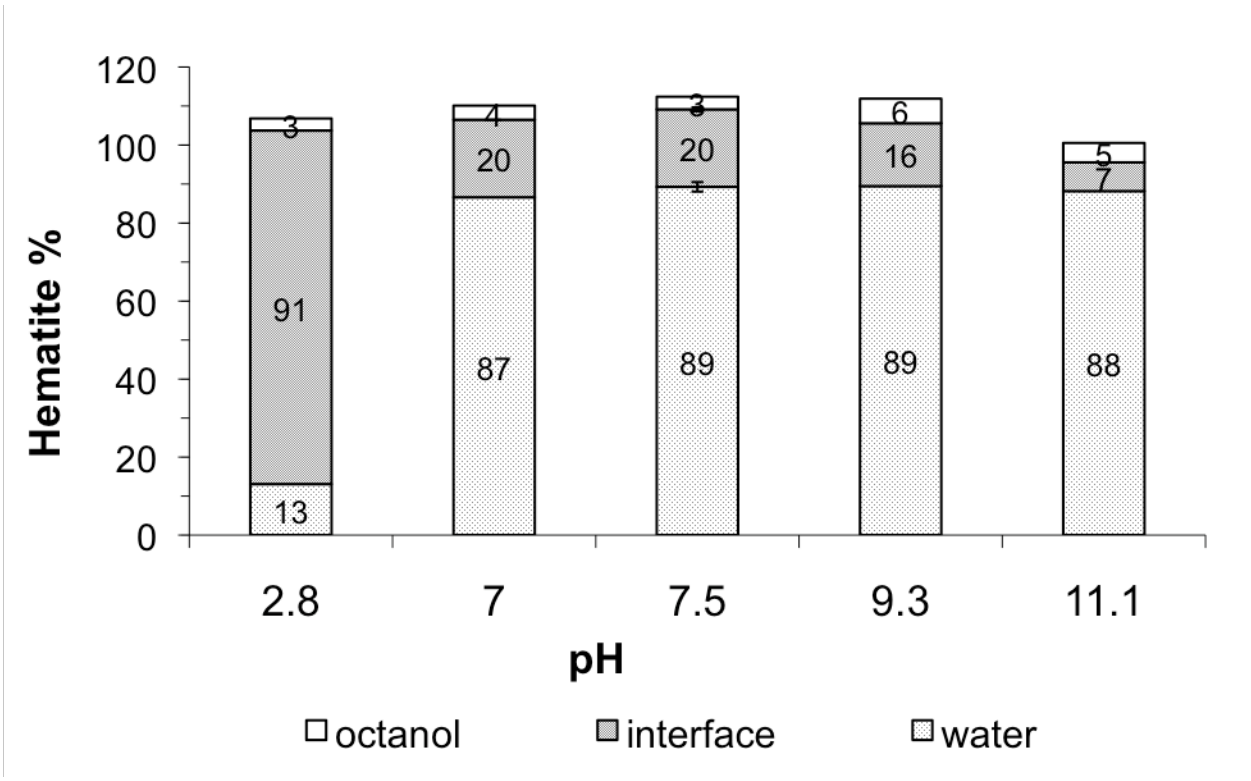

Figure S3. Distribution of hematite nanoparticles in the presence of natural organic matter (NOM) at varying pH values.

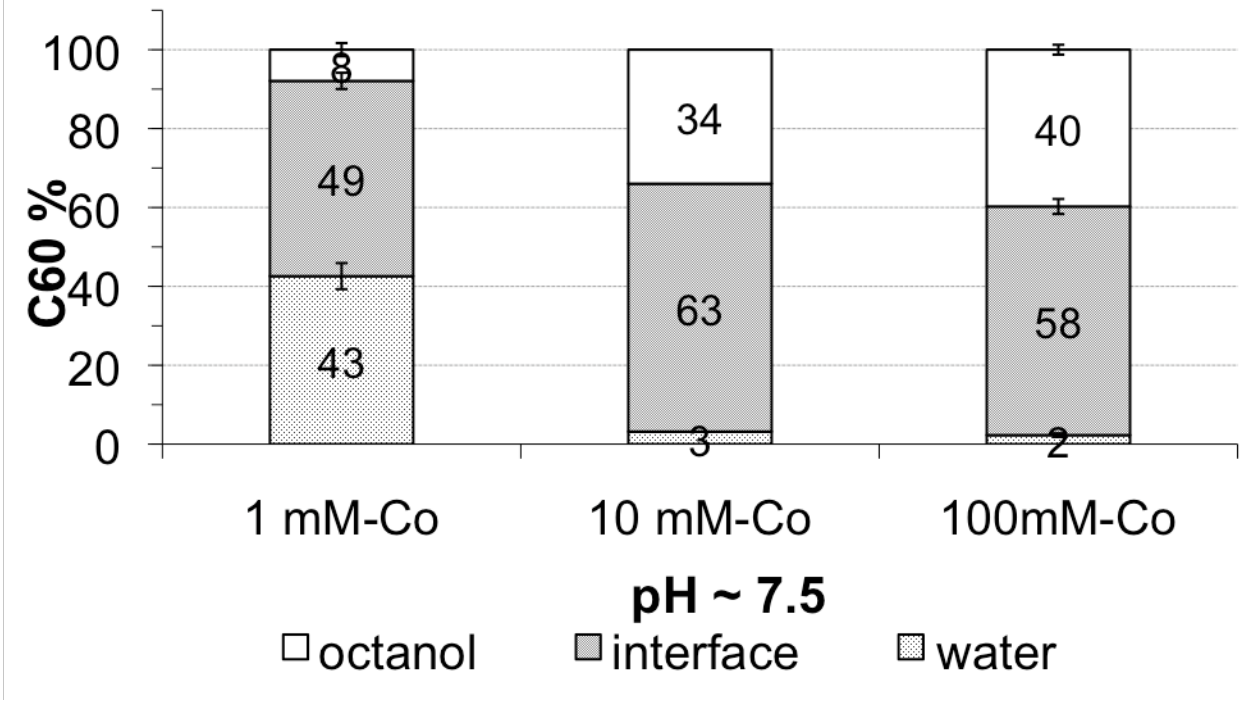

Figure S4. Distribution of nC_{60} nanoparticles of varying ionic strengths and concentrations. Measurements conducted at pH ~7.5. Error bars represent standard deviations.

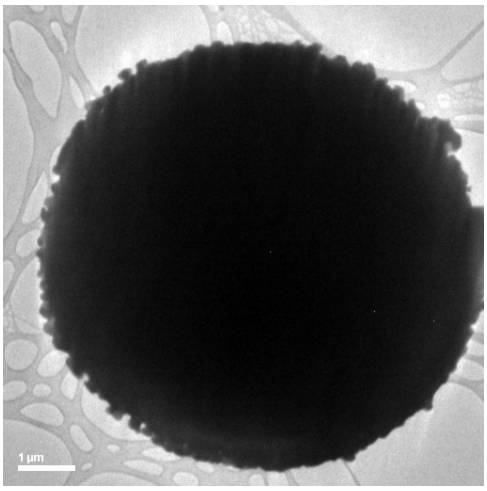

Figure S5. TEM image of TRANSIL SSLM. The scale bar on the bottom left corner indicates 1 µm.

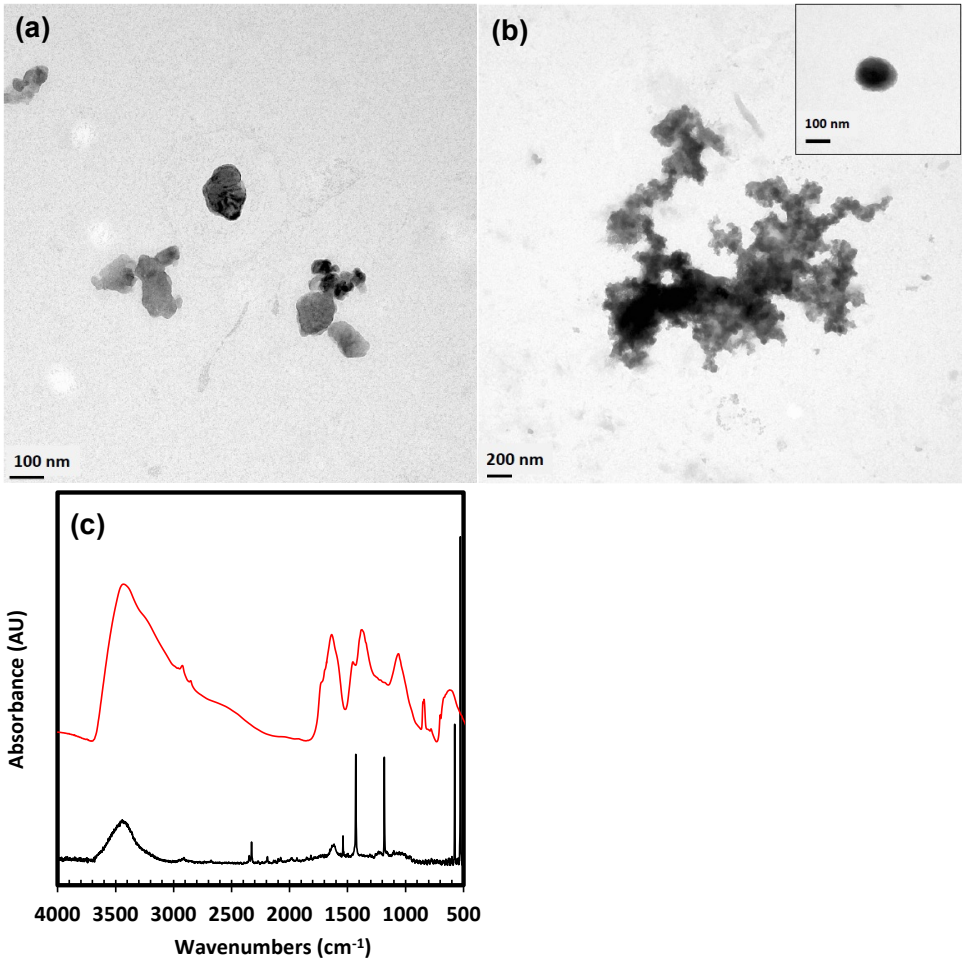

Figure S6. TEM images and FT-IR spectra of nC_{60} and fullerol, indicating the morphology of nC_{60} (a) and fullerol (b), as well as the infrared absorbance of nC_{60} and fullerol (c).

Table S1. Summary of daphnia-water distribution and bioconcentration factors of nC_{60}.

Exposed [nC_{60}] (mg/L)	$C_{biomass, wet}$ † (mg/kg)	$C_{biomass, dry}$ ‡ (mg/kg)	Lipid content % wet biomass	$C_{biomass, lipid}$ # (mg/kg)	log BCF	Ref.
0.5	4,000	-	-	-	3.85[a]	63
0.5	-	50,000	-	-	4.94[b]	63
2	4,600	-	-	-	3.30[a]	63
2	-	57,500	-	-	4.40[b]	63
0.2	240	-	-	-	3.08[a]	64
0.2	-	3,000	-	-	4.18[b]	64
0.1	40	-	8.6	465	3.67[c]	64
0.1	60	-	8.5	706	3.85[c]	64
0.1	70	-	8.8	795	3.90[c]	64
0.1	90	-	9.3	968	3.99[c]	64
0.1	90	-	9.8	918	3.96[c]	64
0.1	170	-	11.7	1453	4.16[c]	64
30	2,300	-	-	-	1.88[a]	62
30	-	28,800	-	-	2.98[b]	62

†$C_{biomass, wet}$ represents nC_{60} concentration accumulated in daphnia on wet biomass basis. ‡$C_{biomass, dry}$ (nC_{60} concentration accumulated in daphnia on dry biomass basis) = $C_{biomass, wet}$/0.08, 0.08 is the dry to wet biomass ratio measured by ref.[63] #$C_{biomass, lipid}$ (nC_{60} concentration accumulated in daphnia based on lipid content) = $C_{biomass, wet}$/lipid content. [a]Wet biomass based log BCF = log ($C_{biomass, wet}$/[nC_{60}]). [b]Dry biomass based log BCF = log ($C_{biomass, dry}$/[nC_{60}]). [c]Lipid based BCF = log ($C_{biomass, lipid}$/[nC_{60}]).

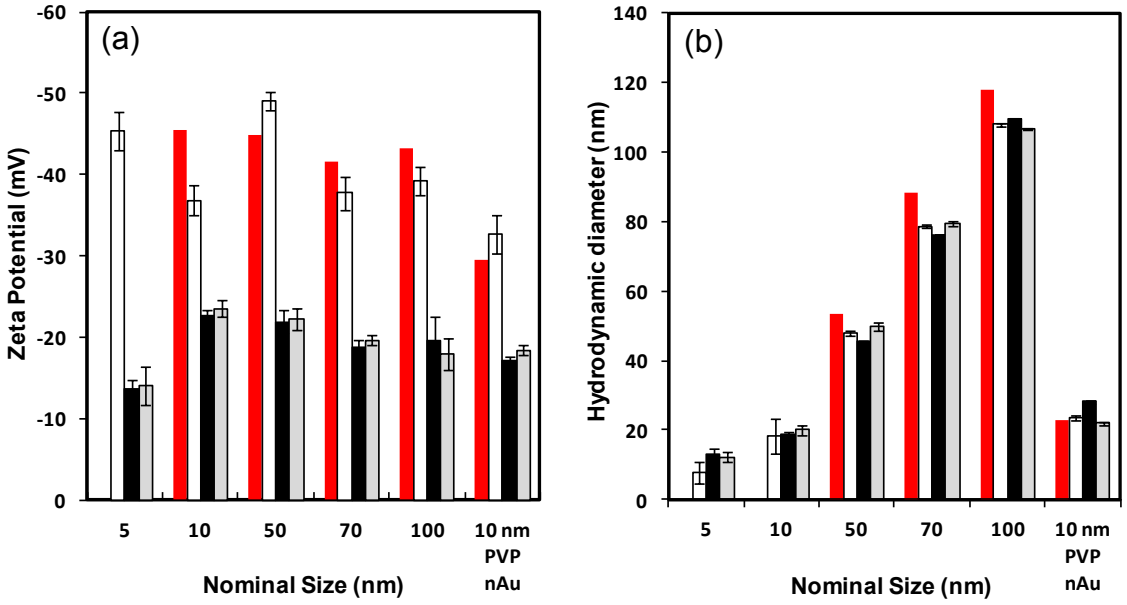

Figure S7. Zeta potentials (a) and hydrodynamic sizes (intensity-weighted) (b) of gold nanoparticles (Au NP) with various sizes and surface functionalities, indicating the values reported by the manufacturer (red bars), measured in DI water (white bars), in pH = 7.4 phosphate electrolyte (5 mM) upon mixing with Au NP (i.e., time zero, black bars), and after 4 h (for size < 70 nm) or 24 h (for size ≥ 70 nm) of mixing (grey bars). All Au NP samples were originally dispersed in DI water when received from the manufacturer and were tannic acid coated unless otherwise noted on the figure. The pH of the solutions was adjusted to pH = 7.4 by the same phosphate buffer electrolyte (5 mM) used for the interaction experiments of SSLM

and Au NP. The zeta potentials for 5 and 20 nm Au NP as well as the hydrodynamic diameters for 5 and 10 nm Au NP are not shown, because the manufacturer did not report them.

Calculation of Gold Nanoparticle and Supported Lipid Bilayer Interaction Energy

The interaction energy is calculated using the Derjaguin-Landau-Verwey-Overbeek (DLVO) theory that considers electrostatic (i.e., electric double layer (EDL)) and van der Waals interactions. Recently, the classical colloid theory (i.e., DLVO theory) has been increasingly used to account for the nano-bio interactions.[31] The interaction energy between Au NPs and supported lipid bilayer is given by equation S1.

$V_T(h) = V_{EDL}(h) + V_{VDW}(h)$ (S1)

Where V_T is the total interaction energy as a function of separation distance h (nm), which is the sum of EDL interaction energy ($V_{EDL}(h)$) and van der Waals interaction energy ($V_{VDW}(h)$). As supported lipid bilayer is fairly larger (10 μm) compared with Au NPs (5-100 nm), it is assumed that the interaction energy can be modeled as plate (i.e., supported lipid bilayer)-sphere (Au NPs) interactions.[18] The following equations are used to assess the interaction energy. The parameters used are summarized in Table S1.

$V_{EDL} = 64\pi\varepsilon_0\varepsilon_r a_p (\frac{k_B T}{ze})^2 \Gamma_{lip}\Gamma_{AuNP} \exp(-\kappa h)$ (S2)[18]

As equation S2 is applicable for large particles and low ionic strength (i.e., $\kappa a_p >> 1$) according to the Derjaguin approximation,[74] an alternative equation (S3) is used when κa_p is close to or smaller than 1 (i.e., for 5 and 10 nm Au NPs).[110]

$V_{EDL} = \left(\frac{64\pi\varepsilon_0\varepsilon_r}{\kappa}\right)\left(\frac{k_B T}{ze}\right)^2 \Gamma_{lip}\Gamma_{AuNP}[(\kappa a_p - 1)\exp(-\kappa h) + (\kappa a_p + 1)\exp(-\kappa(h + 2a_p))]$ (S3)[110]

$V_{VDW} = -\frac{A_{GWL} a_p}{6h(1+\frac{14h}{\lambda})}$ (S4)[18]

Table S2. Summary of parameters

Parameter	Number
Dielectric permittivity in vacuum ε_0	8.85×10^{-12} (F/m)
Relative dielectric permittivity of solution ε	78.5
Particle radius a_p	2.5×10^{-9} - 50×10^{-9} (m)
Boltzmann constant k_B	1.3805×10^{-23} (J/K)
Temperature T	296 (K)
Counterion valence z	1
Electron charge e	1.602×10^{-19} C
Inverse Debye length $\kappa = (\frac{\varepsilon_0\varepsilon_r k_B T}{2N_A I e^2})^{-0.5}$, where NA is the Avogadro's number (6.02×10^{23}); I is the ionic strength.	2.13×10^{8} (1/m)
Dimensionless surface potential for lipid bilayer Γ_{lip} = tanh ($ze\psi_{lip}/4k_BT$), Ψ_{lip} is the zeta potential of lipid bilayer	−0.15
Dimensionless surface potential for Au NP Γ_{AuNP} = tanh ($ze\psi_{AuNP}/4k_BT$), Ψ_{AuNP} is the zeta potential of Au NPs	−0.23 - −0.14
Hamaker constant for lipid bilayer to Au NP in water A_{GWL}	2.77×10^{-21} (J)*
Characteristic wavelength λ	100 (nm)[74]

*The Hamaker constant for supported lipid bilayer and Au NP interacting through water is currently unknown in the literature. Here we estimate it using the method detailed in the next page.

Calculation of the Hamaker constant for supported lipid bilayer and gold nanoparticle interacting through water (A_{GWL}).

The following equation (S5) is used to estimate the Hamaker constant A_{GWL}.[18]

$A_{GWL} = (A_{LL}^{0.5} - A_{WW}^{0.5})(A_{GG}^{0.5} - A_{WW}^{0.5})$ (S5)

A_{LL} is the Hamaker constant for egg PC lipid bilayer interacting across vacuum; A_{GG} is the Hamaker constant for gold interacting across vacuum; A_{WW} is the Hamaker constant for water interacting across vacuum. As the A_{LL} is currently unknown, it is estimated using equation S6.[18]

$A_{121} = (A_{22}^{0.5} - A_{11}^{0.5})^2$ (S6)

Where 1 denotes Au NPs or lipid bilayer and 2 denotes the medium (i.e., water). The A_{LL} and A_{GG} can be estimated by equation S6 using known A_{LWL} and A_{GWG} in the literature as summarized in Table S3. The derived ALL and AGG were then inserted to equation S5 to yield A_{GWL} = 2.77 × 10^{-21} (J). This value compares close to the Hamaker constant for iron oxide nanoparticles and bacteria interacting through water (i.e., 2.40 × 10^{-21} (J)).[75]

Table S3. Summary of Hamaker constants	
A_{WW}	5.74 × 10^{-20} (J)[111]
A_{LWL}	7.50 × 10^{-21} (J)*[112]
A_{GWG}	2.0 × 10^{-19} (J)[113]

*For supported phospholipid bilayers on mica.

Collision rate calculation by using the Smoluchowski equation.[74]

We consider the following equations for perikinetic (Brownian motion of particles) and orthokinetic (fluid motion) transports as well as differential sedimentation.

Perikinetic collision: $k_{ij} = \frac{2k_BT}{3\mu}\frac{(a_i+a_j)^2}{a_ia_j}$

Orthokinetic collision: $k_{ij} = \frac{4}{3}G(a_i + a_j)^3$

Differential sedimentation: $k_{ij} = \frac{2\pi g}{9\mu}(\rho_s - \rho)(a_i + a_j)^3(a_i - a_j)$

The parameters are summarized in Table S4.

Table S4. Summary of parameters of Smoluchowski equations.	
Parameter	Number
Boltzmann constant k_B	1.3805 × 10^{-23} (J/K)
Temperature T	296 (K)
Water viscosity μ	1.14 × 10^{-3} (kg/m/s)
Radius of particle diameter i, a_i	2.5 × 10^{-9} - 50 × 10^{-9} (m) for Au NPs 1.0 × 10^{-5} (m) for TRANSIL SSLM
Mixing intensity, G	1 (1/s) for very low mixing regime 15 (1/s) for mild mixing regime 70 (1/s) for strong mixing regime
Gravity g	9.807 (m^2/s)
Particle density ρ_s	2.65 (g/cm^3) for TRANSIL SSLM
Fluid density ρ	1 (g/cm^3) for water

The results are presented in Figure S8.

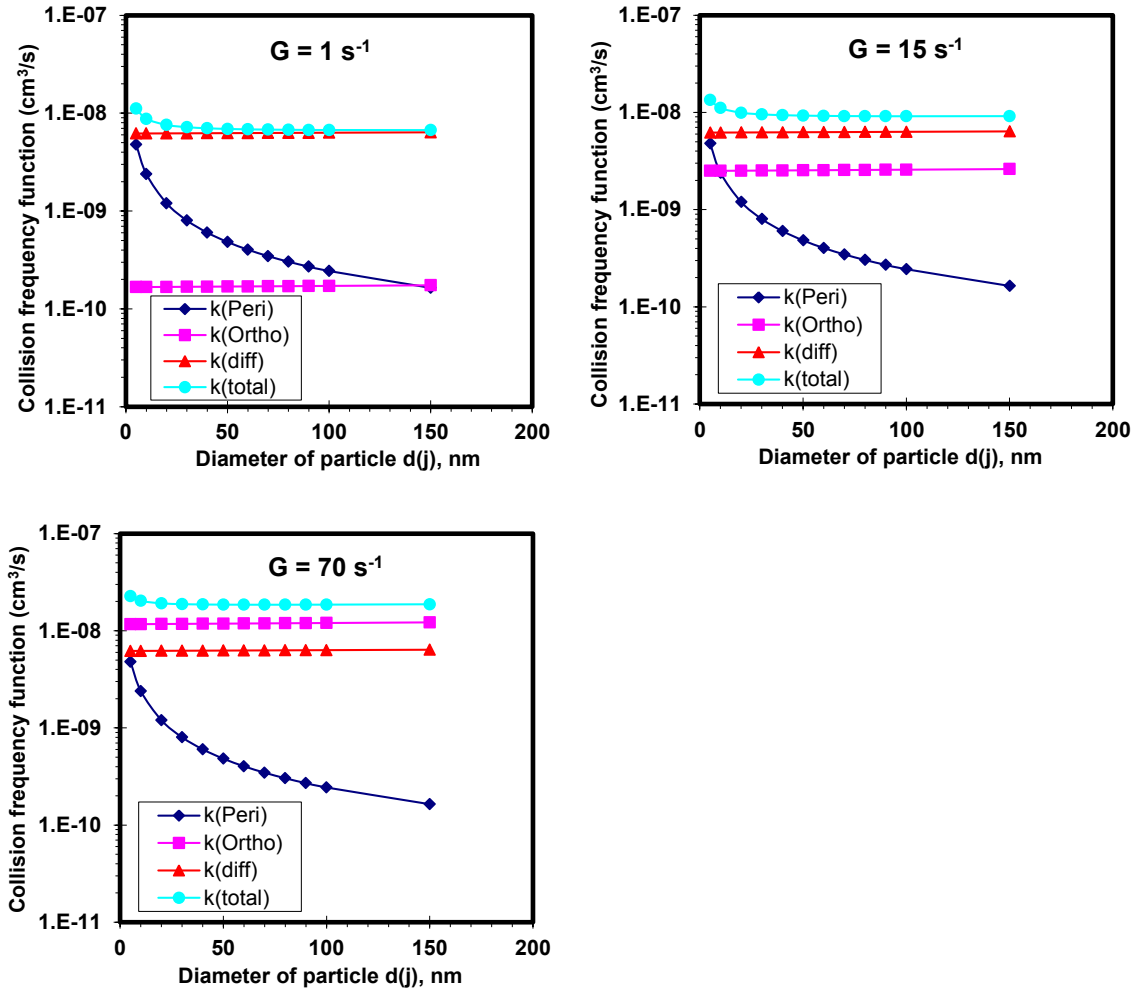

Figure S8. Collision rate calculation under two mixing regimes with G = 1-70 s^{-1}, indicating the collision due to perikinetic (♦) and orthokinetic (■) transports, as well as differential sedimentation (▲), and the total of the three mechanisms (●).

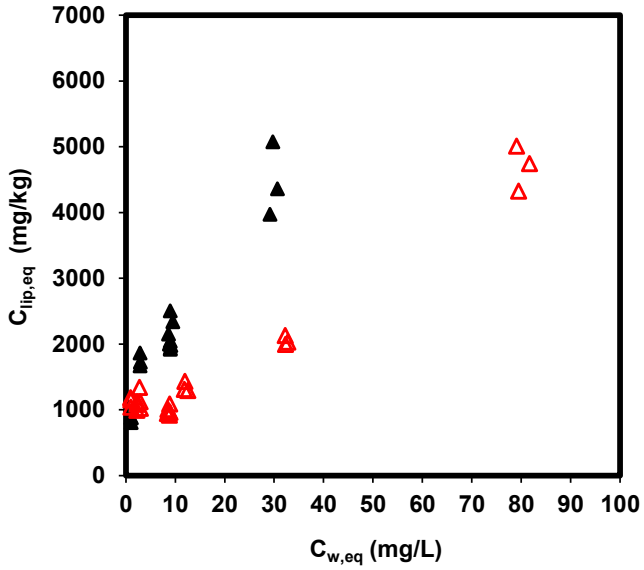

Figure S9. The lipid bilayer-water distribution of tannic acid Au NP versus polyvinylpyrrolidone (PVP) Au NP at pH = 7.4, indicating the distribution of tannic acid Au NP (▲) and PVP Au NP (△).